Doklady Physics, Vol. 48, No. 1, 2003, pp. 1–4. Translated from Doklady Akademii Nauk, Vol. 388, No. 1, 2003, pp. 37–40.

PHYSICS

Features of the Electrode Erosion for Discharge-Current Amplitudes above 10^5 A

A. A. Bogomaz, A. V. Budin, V. A. Kolikov, M. É. Pinchuk, A. A. Pozubenkov, and Academician Ph. G. Rutberg

Received August 5, 2002

In this paper, results of studies of electrode erosion in a dense medium at discharge-current amplitudes exceeding 10^5 A are presented. These results indicate a nonuniform (with respect to time) ingress of the electrode material into the discharge channel. The simultaneous ejection of the cathode material from the entire surface of the electrode end was observed for the first time. The ejection is associated with a violation of the balance between the pressure above the electrode surface, which equilibrates the magnetic force, and the pressure in the depth of the melted surface layer. The mechanism of the electrode-material ejection proposed in the paper allows us to hope for a possibility of regulating the ingress of electrode-material impurities into the discharge channel.

INTRODUCTION

The main goal of the studies being performed by us presently is to generate an electric discharge in a superdense hydrogen medium at temperatures of 10^5–10^6 K and concentrations of charged particles of 10^{19}–10^{21} cm^{-3}. At these discharge parameters, hydrogen is contained in a volume on the order of 1 cm^3 and, in light of its existence time of 10^{-5}–10^{-4} s, can be a source of plasma for thermonuclear studies, as well as for solving a number of other problems. In order to reach the indicated temperatures and concentrations, the required amplitude of the discharge current must attain the level of 1–10 MA. At these currents and short durations of the discharge, the erosion of electrodes exceeds 10^{-2} g C^{-1} [1]. This fact results in the appearance of a considerable amount of electrode-material impurities in the discharge channel. The temperature in the discharge channel decreases due to the increase in the number of heavy particles and radiation loss, which is rather undesirable. In order to reduce the electrode erosion in discharges with the electric-current amplitudes of 0.1–10 MA, further studies of the erosion mechanism are necessary, which is the object of the present paper.

In addition to the well-known phenomenon of erosion in the form of vapor and drops [2], the discovered ejection of the surface layer from the entire surface of the cathode end is an erosion mechanism previously unknown in the conditions under consideration.

EXPERIMENTAL RESULTS AND THEIR DISCUSSION

We studied heavy-current arcs in hydrogen at initial pressures of 1.0–4.0 MPa and discharge-current amplitudes of $(0.5–5.0) \times 10^5$ A with its rate of rise attaining $(0.5–1.0) \times 10^{10}$ A s^{-1}. The distance between axisymmetric tungsten electrodes 6 mm in diameter varied from 5 to 40 mm. The discharge was initiated by exploding a copper or steel wire 0.15 mm in diameter. The walls of the discharge chamber served as a back conducting lead. A sketch of the discharge chamber is presented in Fig. 1. The method of optical measurements is described in [3].

Oscillograms for the electric current and the voltage in the discharge gap are presented in Fig. 2.

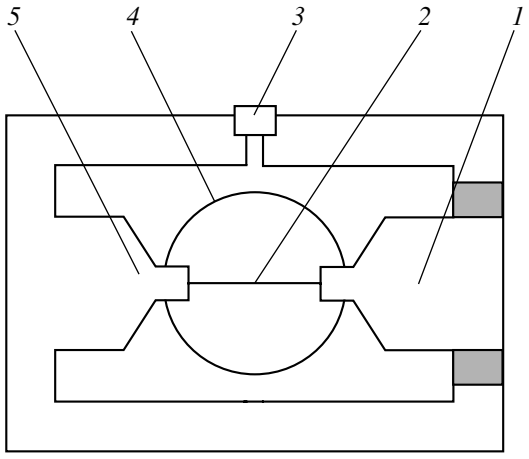

Fig. 1. Diagnostic discharge chamber: (*1*) cathode; (*2*) initiating wire; (*3*) pressure sensor; (*4*) diagnostic windows; and (*5*) anode.

Institute of Problems of Electrophysics, Russian Academy of Sciences, Dvortsovaya naberezhnaya 18, St. Petersburg, 191186 Russia

1028-3358/03/4801-0001$24.00 © 2003 MAIK “Nauka/Interperiodica”

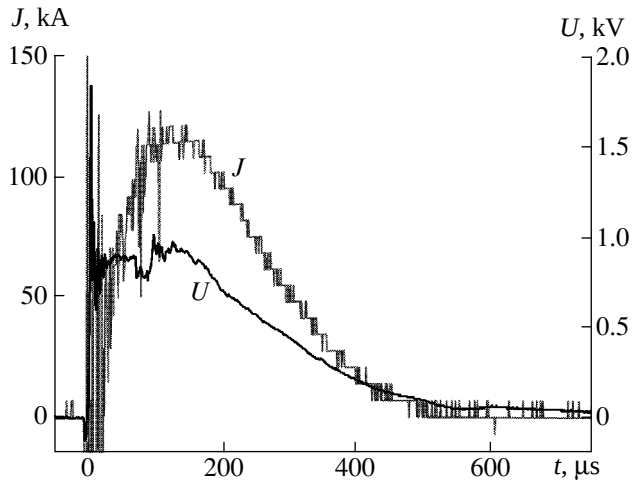

Fig. 2. Oscillograms of the electric-current *J* and voltage *U* at the discharge gap. The initial hydrogen pressure and the diameter of tungsten electrodes are 1 MPa and 6 mm, respectively.

Shadow photographs of the material ejection from the cathode end in the discharge characterized by the initial hydrogen pressure of 1 MPa and the current of 120 kA, which corresponds to the moment of the onset of material ejection, are shown in Fig. 3.

The ejection (Fig. 3, frame 1) begins at the fall of the discharge current after the intense cathode jet with the base diameter equal to the cathode diameter has formed. According to Fig. 3, the velocity of the metal movement and the average ejection-jet width attain ~90 m s^{-1} and ~5×10^{-2} cm, respectively.

In our opinion, the ejection observed is associated with the violation of the equality (corresponding to the maximum of the discharge current) between the magnetic force $\mathbf{j} \times \mathbf{B}$ and the gas-kinetic pressure gradient at the cathode base. The existence of this equality at the base of the anode spot at currents of 10–20 kA was indicated in [4, 5]. The fact of the magnetic confinement at the base of the cathode jet was also observed in [3] at the discharge-current amplitude of 315 kA. In this case, the gas-kinetic pressure at the jet base, which had been determined according to the position of the pressure shock, was 126 MPa, whereas the average pressure determined by formula (1) given below attained 177 MPa. At later times, the magnetic confinement was observed at the anode-jet base.

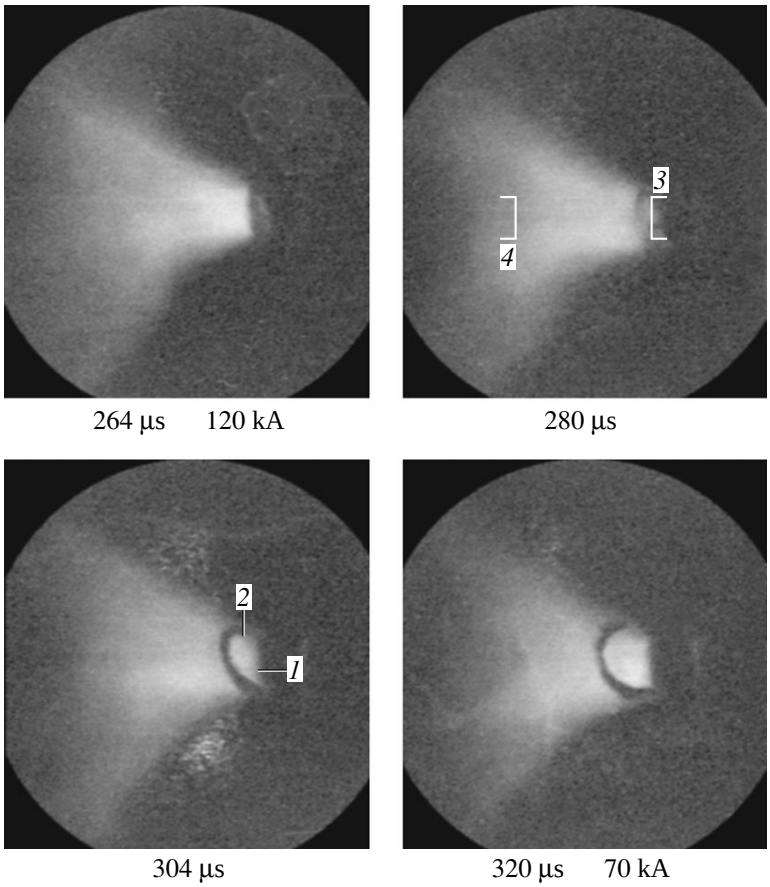

Fig. 3. Shadow photographs of the liquid-tungsten ejection from the cathode surface in a discharge with the initial hydrogen pressure of 1 MPa and the electric-current intensity of 120 kA at the moment of the ejection onset. (*1*) Cathode end; (*2*) zone of the liquid-metal ejection; (*3*) cathode contour; and (*4*) anode contour.

As was shown in [6], for the constant axial current density **j**, in the case when the radial gradient of the gas-kinetic pressure is counterbalanced by the magnetic force $\mathbf{j} \times \mathbf{B}$, which acts inward along the radius r, the profile of the gas-kinetic pressure has the form

$$P(r) = P_{\max}\left(1 - \frac{r^2}{r_0^2}\right) = \frac{\mu J^2}{4\pi^2 r_0^2}\left(1 - \frac{r^2}{r_0^2}\right).$$

Here, r_0 is the radius of the discharge channel, which is equal to that of the electrode. In this case, the pressure averaged over the channel cross section is

$$\frac{P_{\max}}{2} = \frac{\mu J^2}{8\pi^2 r_0^2}. \quad (1)$$

In the conditions of our experiment for the electric-current intensity $J = 120$ kA and $r_0 = 3 \times 10^{-3}$ m, we have $P_{\max} = 51$ MPa.

Apparently, owing to the high-density energy fluxes to the anode, which attain in our experiments 10^8 W cm^{-2}, a common melt wave is formed in several microseconds with its diameter close to that of an electrode. The data of [7] also testify to the high-density energy fluxes. In that study, for approximately the same electric-current amplitudes and geometric sizes, zones with diameters close to those of electrodes and widths of about 1 mm that emitted continuous X-ray radiation were observed near the electrodes.

In the case of the formation of a common melt bath, the melt is not concentrated at the surface of the electrode edges under the action of a high gas-kinetic pressure, so that the central hollow is not formed. Therefore, there exist certain forces in the interior of the liquid melt that equalize the pressure above its surface. The presence of a similar effect for a separate cathode spot was indicated in [8].

It seems that these forces are associated with nonuniform heating of the electrode metal and are rather inertial. Therefore, with a decrease of the discharge current, the magnetic force and the gas-kinetic pressure balancing this force at the electrode surface decay more rapidly than the pressure in the interior of the liquid melt. As a result, the melt is ejected from the cathode surface.

Considering the ejected-shell radius to be equal to the cathode radius $r_0 = 0.3$ cm and the tungsten density and the shell thickness to be $\rho = 19.4$ g cm^{-3} and 5×10^{-2} cm, respectively, we arrive at the shell mass of 0.27 g. This result corresponds to the specific erosion of 8×10^{-3} g C^{-1}. This is close to the value of the specific erosion of the cathode, which was found in the discharge chamber of the electric-discharge accelerator for electric currents of about 10^6 A [1].

According to the above, the observed ejection of the electrode material is associated with heating of the electrode due to the formation of the common melt bath under the effect of magnetic forces. Therefore, owing to the enhanced energy release in the discharge near-electrode zones discovered by us previously [3], a similar mechanism of material ejection must be observed at both the cathode and the anode. In experiments with a larger electrode diameter (10 mm), a bright flame with a diameter of 1–2 mm was observed at the anode center at later times (20–50 μs after the discharge onset). This testifies to an increase in the electric-current density at the center of an electrode. The larger current density corresponds to a pressure even higher than was estimated by formula (1). In this case, after the decay of the electric current, metal ejection in the form of a narrow, dark jet with a diameter of 1–2 mm is seen at the center of the electrode (Fig. 4).

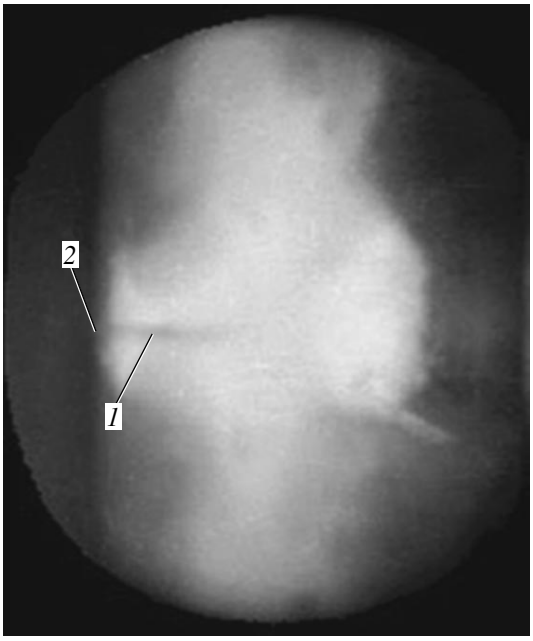

Fig. 4. Ejection of a narrow metal jet from the anode: (*1*) metal jet and (*2*) anode end.

CONCLUSIONS

The observed ejection of the material from the entire electrode surface substantially contributes to electrode erosion at electric currents of 10^5–10^6 A.

We have proposed a mechanism of electrode-material ejection. This mechanism is associated with the violation of the balance between the pressure above the electrode surface and in the electrode interior. The indicated mechanism can act for both electrodes by virtue of symmetry of the energy release in the near-electrode discharge zones and close values of magnetic pressures. The proposed ejection mechanism makes it possible to decrease the ingress of erosion impurities into the discharge channel. This can be attained by the squeezing of the liquid melt at the electrode surface with gas-

kinetic pressure, which is balanced by the magnetic force formed by the discharge current.

ACKNOWLEDGMENTS

The work was supported in part by the Russian Foundation for Basic Research, project nos. 02-02-16770 and 00-15-96604.

REFERENCES

1. A. V. Budin, V. A. Kolikov, B. P. Levchenko, *et al.*, Teplofiz. Vys. Temp. **32**, 628 (1994).
2. G. A. Mesyats, *Ectons in Vacuum Discharge: Breakdown, Spark, and Arc* (Nauka, Moscow, 2000).
3. A. A. Bogomaz, A. V. Budin, V. A. Kolikov, *et al.*, Zh. Tekh. Fiz. **72**, 28 (2002) [Tech. Phys. **47**, 26 (2002)].
4. V. A. Nemchinskiĭ, Zh. Tekh. Fiz. **52**, 35 (1982) [Sov. Phys. Tech. Phys. **27**, 20 (1982)].
5. V. A. Nemchinskiĭ, Zh. Tekh. Fiz. **53**, 235 (1983) [Sov. Phys. Tech. Phys. **28**, 146 (1983)].
6. J. A. Shercliff, *Textbook of Magnetohydrodynamics* (Pergamon, Oxford, 1965; Mir, Moscow, 1967).
7. H. Chuagui, M. Favre, R. Savedra, *et al.*, IEEE Trans. Plasma Sci. **26**, 1162 (1998).
8. A. V. Zharinov and Yu. V. Sanochkin, Pis'ma Zh. Tekh. Fiz. **9** (23), 1465 (1983) [Sov. Tech. Phys. Lett. **9**, 629 (1983)].
9. D. F. Alferov, V. A. Nevrovskiĭ, and V. A. Sidorov, Teplofiz. Vys. Temp. **40**, 19 (2002).

Translated by G. Merzon

Doklady Physics, Vol. 48, No. 1, 2003, pp. 13–17. Translated from Doklady Akademii Nauk, Vol. 388, No. 2, 2003, pp. 181–185.

PHYSICS

The Critical Point of an Exothermic Reactor

A. Yu. Dovzhenko*, M. Dovzhenko, L. B. Mashkinov***, and É. N. Rumanov***,[1]**

Presented by Academician A.G. Merzhanov July 10, 2002

Received July 16, 2002

Conditions for quenching and igniting an exothermic reactor differ from one another, since a hysteresis takes place. In the parameter plane, the bistability region is represented as a peninsula terminating in a cusp. At the cusp point, the difference between high-temperature and low-temperature regimes disappears. In this respect, the cusp is similar [1] to the critical point of a phase transition (e.g., the liquid–vapor transition) in which the distinction between phases disappears. As is well known, density fluctuations are strong at the critical point. Similarly, we can expect an increase in the chaotic pulsations of temperature and concentration in the neighborhood of the cusp. In contrast to equilibrium thermal fluctuations in the case of phase transitions, these pulsations are caused by small random variations in the composition and other parameters of the incoming mixture. Usually, such variations do not lead to marked changes in the reactor state. However, near the critical point in which the reactor susceptibility is especially high, the pulsation intensity increases infinitely when approaching this point. In this study, we investigated the chaotic behavior of the reactor in the critical region of parameters. The similarity with the critical point of phase transition relates to reactor steady-state regimes. Under certain conditions, the region of periodic regimes [2–4] can include a cusp. Below, we also consider the effect of this factor.

1. We can write equations for small deviations from the steady-state regime in the form

$$\frac{d\eta}{dt} = A_{11}\eta + A_{12}\theta, \tag{1}$$

$$\frac{d\theta}{dt} = A_{21}\eta + A_{22}\theta + y(t), \tag{2}$$

$$\langle y(t)y(t')\rangle = \langle y^2\rangle\delta(t-t'), \quad \langle y^2\rangle \ll 1. \tag{3}$$

Here, η and θ are, respectively, the deviations in the concentration of reaction products and in the dimensionless temperature from their steady-state values and t is the dimensionless time. Without noise, denoted as $y(t)$, the steady-state regime is stable if both eigenvalues of the matrix A_{ik} have a negative real part. In other words, it is necessary that $p < 0$ and $q > 0$, where p is the trace and q is the determinant of this matrix. First, we consider reactor parameters such that $p < 0$. At the critical point, the matrix A_{ik} degenerates and $q = 0$. Indeed, when the parameters correspond to the bistability region, the reactor equations have three time-independent solutions. Two of them are stable ($q > 0$), while the third solution is unstable ($q < 0$). At the cusp, all the three solutions merge, which is evidently possible only for $q = 0$. In the neighborhood of the cusp, $|q|$ is a small quantity.

Weak random actions ($y \neq 0$) lead to deviations in concentration and temperature from steady-state values. According to Eqs. (1)–(3), the Fourier components of the correlators $\langle\theta(0)\theta(t)\rangle$ and $\langle\eta(0)\eta(t)\rangle$ have the form

$$(\theta^2)_\omega = \langle y^2\rangle\left[\left(\frac{A_{11}A_{12}A_{21}}{A_{11}^2+\omega^2} - A_{22}\right)^2 + \left(1 + \frac{A_{12}A_{21}}{A_{11}^2+\omega^2}\right)^2\omega^2\right]^{-1}, \tag{4}$$

$$(\eta^2)_\omega = (\theta^2)_\omega A_{12}^2(A_{11}^2+\omega^2)^{-1}. \tag{5}$$

At high frequencies, $(\theta^2)_\omega$ decreases as ω^{-2}. For $\omega \longrightarrow 0$, the expression in the square brackets of formula (4) is approximately equal to $q^2A_{11}^{-2} + B^2\omega^2$, where $B \approx pA_{11}^{-1}$. Thus, the pulsation spectra have a maximum at zero frequency with the peak width $\backsim q$, so that the peak narrows when approaching the critical point. Correspondingly, the mean pulsations squared and correla-

* *Landau Institute for Theoretical Physics, Russian Academy of Sciences, ul. Kosygina 2, Moscow, 117940 Russia*

** *Experimental School no. 82, Russian Academy of Education, Chernogolovka, Moscow oblast, Russia*

*** *Institute of Structural Macrokinetics, Russian Academy of Sciences, Chernogolovka, Moscow oblast, 142432 Russia*

[1] *e-mail: ed@ism.ac.ru*

tion times diverge as $\frac{1}{q}$. It should be noted that, in contrast to the flicker-noise (see [5]), the low-frequency peak disappears with distance from the cusp.

Let the value of p at the negative critical point approach zero. For $p^2 < 4q$, the (attenuating) oscillatory modes appear. Their frequency increases from 0 to $\sqrt{q}$ as p varies from $-2\sqrt{q}$ to 0. For $p^2 \ll q$ and frequencies close to $\sqrt{q}$, the square bracket in formula (4) takes the form of the resonance denominator:

$$(\theta^2)_\omega \approx \langle y^2 \rangle A_{11}^{-2}[(\omega^2 - q)^2 + p^2 q]^{-1}. \qquad (6)$$

As is seen, the periodic regimes do not affect the behavior of the reactor near the critical point until the boundary of the oscillatory instability lies in the neighborhood of this point. Intense low-frequency fluctuations recall the critical behavior in the case of continuous phase transitions (e.g., critical opalescence, etc.). However, the fluctuations accompanying the phase transitions are of thermal nature. Therefore, introducing a random force $y(t)$ for calculating correlators, we choose the quantity $\langle y^2 \rangle$ in such a manner that the variance for the fluctuations turns out to be equilibrium. In our case, $\langle y^2 \rangle$ should be considered as a given quantity evidently independent of q, and the behavior of pulsations is completely determined by formulas (4)–(6). These formulas obtained in the linear approximation are valid until the pulsations are small. To avoid this restriction, the pulsations were studied experimentally with the help of an electric circuit modeling the operation of the reactor.

2. The circuit is based on a nonlinear element (dynistor) with an *S*-shaped current–voltage characteristic and a constant (independent of current and voltage) resistor R connected in series with the dynistor. The direct-current regimes are determined by the intersection of the characteristic curve $I(V)$ and the load straight line $I = \frac{V_0 - V}{R}$. Here, I, V_0, and V are the electric current flowing across the circuit, the applied voltage, and the voltage across the dynistor, respectively. Depending on R and V_0, one or three intersection points are possible. The middle of three intersection points is unstable. At the (R, V_0) plane, the bistability region has the shape of a peninsula terminating in a cusp. The similarity with the reactor steady-state regimes is evident. We used a KN102A dynistor. The voltage drop V across the dynistor was applied to the analog-to-digital converter in the form of an L-154 (*L*-CARD) computer board. To this end, we used an amplifier made on the basis of a K544UD2A chip with an input resistance of 6.8 MΩ, a frequency range of 500 kHz, and a gain of 1. For the given values of R and V_0, the function $V(t)$ was recorded in the intervals of 10^{-3} s. Furthermore, another pair of values of R and V_0 was used, and a new function was recorded, etc. Deviations of the function $V(t)$ from a constant value are caused by oscillations of the line voltage and other random factors (when recording, the constant value of V_0 was maintained within an accuracy of 0.01 V). Until R and V_0 are far from the critical point, such deviations are negligible ($\delta V \sim \delta V_0$). In the vicinity of this point, we observed deviations on the same order as the mean value of V. The total number of experiments was 256. From each of the $V(t)$ records, we determined the mean value $\langle V \rangle$ and the mean deviation squared $\langle v^2 \rangle$, where $v = V - \langle V \rangle$. We also calculated the spectral density $(v^2)_\omega$ of the pulsations.

Studies of the chaotic behavior of circuits with a nonlinear element were begun in [6]. However, the situation that was analyzed in [6] was such that, in the system space of states, the trajectories converged to a strange attractor. In our case, the attractor is a point, which corresponds to the steady-state regime. But the attraction to this point is weak due to the closeness of unstable elements in the space of states (saddle points, unstable cycles, etc.), which restricts the basin of attraction. From here, the mechanism of chaotization described in the introduction to this paper follows. The critical point in the (R, V_0) plane was obtained [7, 8] for a circuit with a semiconductor. The activation shape of the temperature dependence for its conductivity leads to a thermal instability as in the case of the exothermic reactor. The disadvantage of such a circuit is its high transit time for thermal processes compared to electric ones.

In Fig. 1, we show the variance $(\langle v^2 \rangle)^{1/2}$ as a function of R and V_0. As is seen, this quantity increases when approaching the cusp. The highest values are concentrated near the straight line in the (R, V_0) plane. The boundaries of the bistability region, which have a common tangent, converge to the cusp. This tangent is an analog of the phase-equilibrium line (in the vicinity of the critical point). In this regard, the pulsations can be considered as slow transitions between the regimes of strong and weak currents. In the case of a reactor, these transitions correspond to waves of ignition and quenching. At the same time, for the liquid–vapor system, this is a chaotic motion of interphase boundaries, which is responsible for the critical opalescence. The measured values of V lie within the interval of 2–6 V, so that the variance near the cusp is comparable with a mean value of a fluctuating quantity as is the case for the developed turbulence. The most marked feature of the chaos under consideration is the slow rate of its evolution.

This slowness is illustrated by pulsation spectra. An example of such a spectrum is shown in Fig. 2a. For comparison, in Fig. 2b, we show the spectrum calculated on the basis of a record obtained at a certain distance from the cusp. This spectrum represents the usual

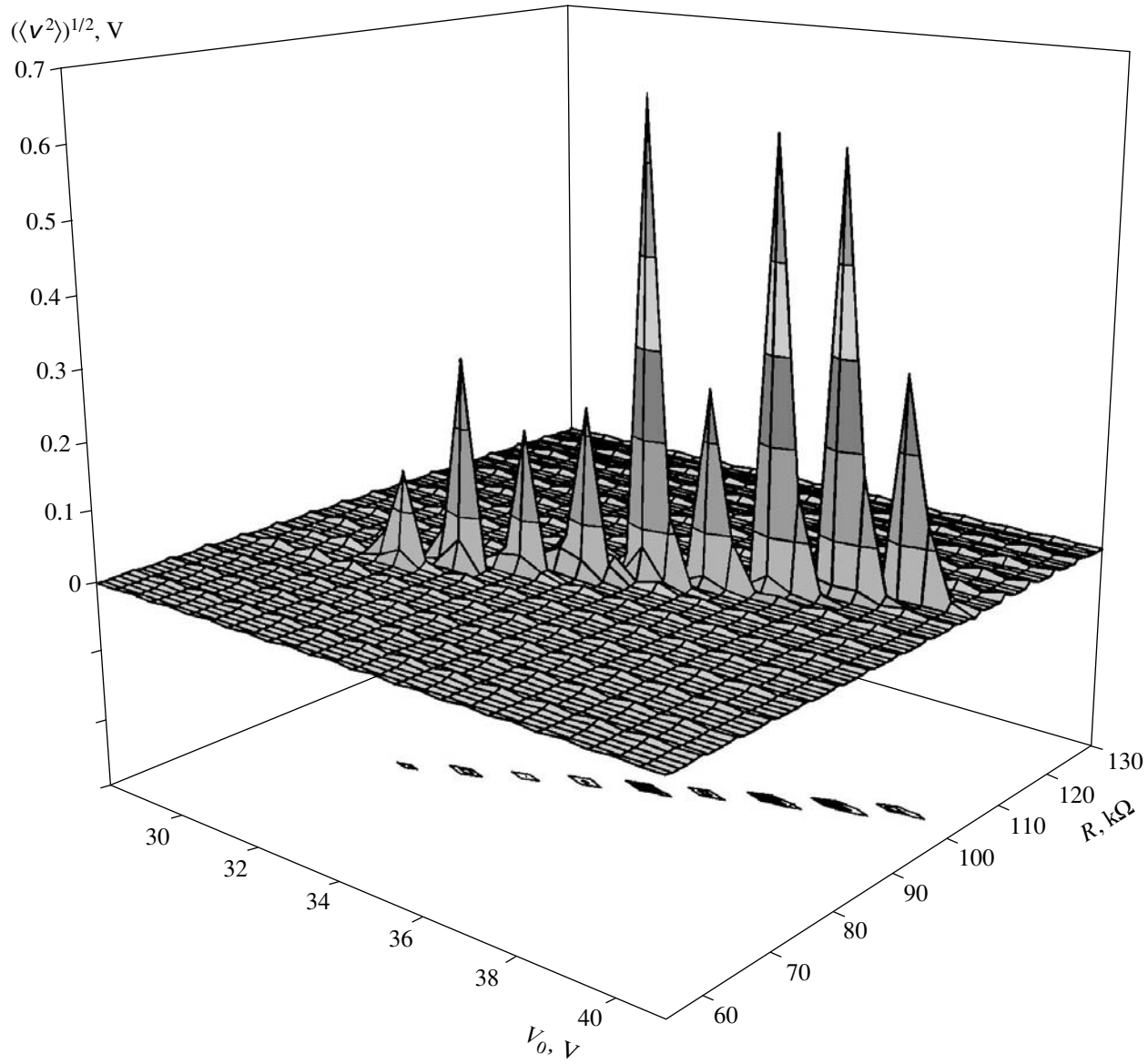

Fig. 1. Variance of pulsations. Below, the horizontals in the (R, V_0)-plane are shown.

white noise, whereas the spectrum in Fig. 2a has a sharp maximum at zero frequency. It is seen that approaching the cusp leads to amplification at all frequencies, but low frequencies are amplified to a larger degree. For the major fraction of the experiments, the recording time for $V(t)$ attained t_0 = 100 s (records with the 200-s and 500-s durations were also made). Therefore, an interval with a width of $\geq 10^{-2}$ Hz can be resolved in the spectrum. The width of the spectral maximum near the cusp is likely much smaller than $\sim 10^{-4}$ Hz as in [8]. For the 100-s records, these low frequencies manifest themselves as a drift towards an increase or a decrease of V. Near the cusp, we performed averaging over several records made for the same values of R and V_0 in various day periods. In order to approach the cusp, it is necessary either to gather statistics of long-term records or to pass to another modeling circuit. Both these variants are considered. We should also note that an additional resonance was observed at a frequency of about 9 Hz for R = 85 kΩ and V_0 = 31 V. The intensity of this resonance was lower than for the main peak by a factor of approximately 15, and its width was ~1 Hz.

Thus, in this study, we observed an effect of enhancing pulsations near the cusp and indicated the nature of this effect. As far as its scale is concerned, the pulsations are highly competitive with the developed turbulence and must be considered as a new type of chaos. The chaos is caused by the high susceptibility of the system near the bifurcation point (in our case, near the cusp). The low external noise inherent in both the

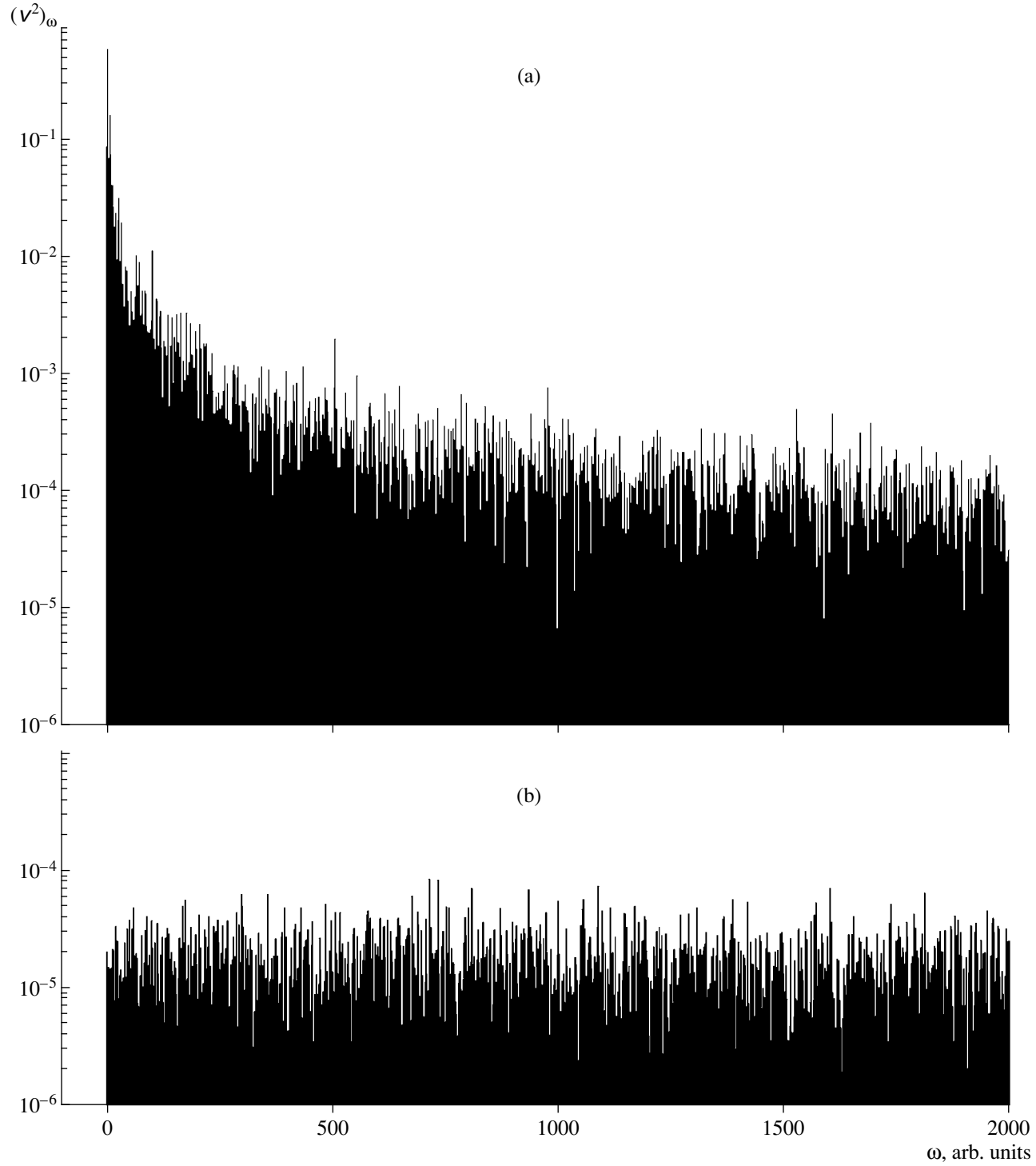

Fig. 2. Frequency spectra of pulsations. (a) R = 75 kΩ, V_0 = 30 V; (b) R = 60 kΩ, V_0 = 32 V. The frequency ω is given in units of $\frac{2\pi}{t_0}$, and the time of the experiment is t_0 = 100 s.

incoming mixture and the mains turns out to be a source of pulsations for the reactor and for the modeling circuit, respectively. However, the properties of pulsations (to within an accuracy of a constant factor in the expression for their intensity) are independent of the noise. Indeed, the correlation time increases infinitely for pulsations when approaching the cusp, whereas this time remains evidently finite for an external noise. Therefore, any arbitrary external noise near the bifurcation point can be considered as δ-correlated (white) noise.

ACKNOWLEDGMENTS

The authors are grateful to A.G. Merzhanov and K.G. Shkadinskiĭ for discussing the results obtained.

This work was supported by the Russian Foundation for Basic Research, project no. 01-03-32772.

REFERENCES

1. A. G. Merzhanov and É. N. Rumanov, Usp. Fiz. Nauk **151**, 553 (1987) [Sov. Phys. Usp. **30**, 293 (1987)].
2. D. A. Frank-Kamenetskiĭ and I. E. Sal'nikov, Zh. Fiz. Khim. **17**, 79 (1943).
3. R. Aris and N. R. Amundson, Chem. Eng. Sci. **7**, 121 (1958).
4. D. A. Vaganov, N. G. Samoilenko, and V. G. Abramov, Chem. Eng. Sci. **33**, 1133 (1978).
5. M. B. Weissman, Rev. Mod. Phys. **60**, 537 (1988).
6. A. S. Pikovskiĭ and M. I. Rabinovich, Dokl. Akad. Nauk SSSR **239**, 301 (1978) [Sov. Phys. Dokl. **23**, 183 (1978)].
7. É. N. Rumanov, Dokl. Akad. Nauk **336**, 328 (1994) [Phys. Dokl. **39**, 339 (1994)].
8. V. G. Abramov, É. N. Rumanov, D. V. Strunin, and S. A. Shevchenko, Dokl. Akad. Nauk **353**, 177 (1997) [Phys. Dokl. **42**, 111 (1997)].

Translated by V. Bukhanov

Doklady Physics, Vol. 48, No. 1, 2003, pp. 18–20. Translated from Doklady Akademii Nauk, Vol. 388, No. 2, 2003, pp. 186–188.

PHYSICS

Self-Similar Rotation of a Toroidal Plasma Configuration

N. D. Naumov

Presented by Academician A.F. Andreev October 9, 2002

Received October 15, 2002

Unsteady solutions to magnetohydrodynamic equations were obtained for time-dependent one-dimensional motions of plasma [1, 2]. These motions relate to the class of self-similar motions of a continuum for which velocities are proportional to the distance to the symmetry center. In the present paper, the exact solution to the two-dimensional motion of the class indicated above is constructed. This solution describes the time dependence of the size of a toroidal configuration for rotating plasma.

We initially present the results obtained for immobile plasma. As is well known, one of the solutions to the Shafranov equations corresponds to a toroidal configuration with the following azimuth distribution of the electric-current density:

$$\psi = \frac{1}{2}\psi_0\left[r^2z^2 + \frac{\alpha-1}{4}(r^2-R^2)^2\right], \qquad (1)$$

where R is the radius of a magnetic axis and ψ_0 and α are certain constant values. Expression (1) describes the unsteady state of plasma with pressure in it related to the magnetic flux by the formula

$$16\pi^3\frac{dP}{d\psi} = -\mathrm{div}\frac{\nabla\psi}{r^2} = -\alpha\psi_0. \qquad (2)$$

We can find from relationship (1) for the magnetic field

$$B_r = -\frac{1}{2\pi r}\frac{\partial\psi}{\partial z} = -\frac{\psi_0}{2\pi}rz, \qquad (3)$$

$$B_z = \frac{1}{2\pi r}\frac{\partial\psi}{\partial r} = \frac{\psi_0}{2\pi}\left[z^2 + \frac{\alpha-1}{2}(r^2-R^2)\right]. \qquad (4)$$

We consider that $\psi_0 = \dfrac{8\pi^2 j_0}{cR\alpha}$. Then, the density of the electric current flowing through the plasma is $j_\varphi = -\dfrac{j_0 r}{R}$.

In the case of the steady-state rotation of an axisymmetric plasma configuration, the condition of freezing-in of magnetic-field lines for $\mathbf{V} = V_\varphi\mathbf{e}_\varphi$ has the form

$$\frac{\partial V_\varphi B_r}{\partial r} + \frac{\partial V_\varphi B_z}{\partial z} = 0. \qquad (5)$$

As is easy to understand, this condition holds for $V_\varphi = \Omega r$, where Ω is a constant quantity, since, in this case, expression (5) is equivalent to the equation $\mathrm{div}\,\mathbf{B} = 0$.

The equilibrium condition for the rotating plasma possessing an azimuth distribution of the electric-current density includes the centrifugal term

$$\frac{1}{c}j_\varphi B_z = \frac{\partial p}{\partial r} - \rho\frac{V_\varphi^2}{r}.$$

If the solution to the equation of equilibrium for an immobile plasmoid is known, we can easily generalize this solution to the case of a configuration rotating as a single whole. In order to do this, we should choose the plasma-density distribution in the form

$$\rho = -\frac{\beta j_\varphi}{cr\Omega^2},$$

where β is a certain constant quantity.

In this case, to confine the rotating plasma, it is necessary to impose the external homogeneous magnetic field $\mathbf{B}_{\mathrm{ext}} = \beta\mathbf{e}_z$. The interaction of this field with the azimuth electric current compensates for the effect of the centrifugal term. In particular, for toroidal configuration (1) of the rotating plasma, we obtain the homogeneous plasma-density distribution:

$$\rho = \rho_0 = \frac{\beta j_0}{cR\Omega^2},$$

and the expression for the axial magnetic-field component (4) should be complemented by the quantity β.

We now will analyze the time-dependent problem. We denote as $a = a(t)$ and $b = b(t)$ the axial and radial dimensions of the moving plasmoid. We consider, for definiteness, that $a(0) = R$ and $b(0) = L$, where L is the longitudinal size of the toroidal configuration in the steady state. For the class of motions under consider-

1028-3358/03/4801-0018$24.00

ation, the plasma density and velocity of plasma components have the form

$$\rho = \rho_0 \frac{LR^2}{ba^2}, \quad V_r = \dot{a}\xi,$$
$$V_\varphi = \Omega\xi\frac{R^2}{a}, \quad V_z = \dot{b}\eta. \tag{6}$$

Here, $\xi = \frac{r}{a}$ and $\eta = \frac{z}{b}$ are self-similar variables.

In order to find expressions for magnetic-field components that satisfy the freezing-in conditions, we use the corollary to this condition

$$\frac{d}{dt}\left(\frac{\mathbf{B}\nabla S}{\rho}\right) = 0, \tag{7}$$

where S is an arbitrary quantity being conserved for the plasma motion. Assuming in (7) the quantity S sequentially equal to ξ and η, we immediately find the general form of desired expressions:

$$B_r = \frac{RL}{ab} f(\xi, \eta), \quad B_z = \frac{R^2}{a^2} g(\xi, \eta), \tag{8}$$

where f and g are certain functions. As a result, with allowance for expressions (3) and (4), we arrive at

$$f = -\frac{\psi_0}{2\pi} RL\xi\eta,$$
$$g = \beta + \frac{\psi_0}{2\pi}\left[L^2\eta^2 + \frac{\alpha - 1}{2}R^2(\xi^2 - 1)\right]. \tag{9}$$

In other words, in order to satisfy the freezing-in condition, the external homogeneous magnetic field must be time-dependent: $\mathbf{B}_{\text{ext}} = \beta\left(\frac{R}{a}\right)^2 \mathbf{e}_z$.

It is worth noting that these results could also be obtained by the self-similar extrapolation of solution (1), which leads to the following expression for the magnetic flux:

$$\Psi = \pi\beta\frac{R^2}{a^2}r^2 + \psi,$$
$$\psi = \frac{1}{2}\psi_0 R^2\left[\left(\frac{Lrz}{ab}\right)^2 + \frac{\alpha - 1}{4}R^2\left(\frac{r^2}{a^2} - 1\right)^2\right].$$

For the determination of time dependences of the configuration sizes, we should substitute expressions (6), (8), and (9) into the Euler equations. Assuming the pressure of the moving plasma to be related to the function ψ in the same manner as in the case of an immobile plasma, i.e.,

$$16\pi^3\frac{dP}{d\psi} = -\text{div}\frac{\nabla\psi}{r^2},$$

we obtain as a result

$$\ddot{a} = \Omega^2\frac{R^4}{a^3}\left[1 - \frac{b}{L}\left(1 - \frac{1}{\alpha}\right) - \frac{La^2}{\alpha bR^2}\right], \quad \ddot{b} = 0. \tag{10}$$

The solution of the second equation in Eqs. (10) is evident. At the same time, at $b = L$, constructing a solution to the first equation is easy for small radial oscillations in the vicinity of the steady state. Linearizing this equation, we find the relation for the radius of the magnetic axis

$$a = R\left(1 + \frac{u}{\omega}\sin\omega t\right),$$

where u is constant and $\omega = \Omega\sqrt{\frac{2}{\alpha}}$.

We now analyze the results obtained for the case of a thin toroidal pinch. First, we consider the steady-state solution. In the vicinity of the magnetic axis, the relationship

$$\psi \approx \frac{1}{2}\psi_0 R^2[z^2 + (\alpha - 1)q^2] \tag{11}$$

is valid. Here, $q = r - R$. Assuming that $\alpha = \lambda^2 + 1$, $\lambda = \frac{L}{D}$, we find that the cross section of magnetic surface (11) is an ellipse with the semiaxes L and D. The small parameter is the ratio of the transverse sizes of the pinch cross section to the magnetic-axis radius.

In accordance with formula (2), the plasma pressure of the thin toroidal pinch is

$$p = Q\left(1 - \frac{q^2}{D^2} - \frac{z^2}{L^2}\right),$$

where $Q = \frac{2\pi j_0^2 L^2}{\alpha c^2}$. We also find for the magnetic field that, to within the accepted accuracy,

$$B_r = -\frac{4\pi j_0}{\alpha c}z, \quad B_z = \beta + \frac{4\pi j_0\lambda^2}{\alpha c}q. \tag{12}$$

Magnetic field (12) includes the magnetic field formed by the plasma pinch, as well as the external confining magnetic fields, namely, the homogeneous field and quadrupole-type field. The latter has the same form as in the case of a rectilinear plasma pinch with the elliptic cross section [4]:

$$\mathbf{B} = \beta\mathbf{e}_z + \mathbf{B}_0 + \mathbf{B}_1, \tag{13}$$
$$B_{0r} = kz, \quad B_{0z} = kq, \quad k = \frac{4\pi j_0\lambda(\lambda - 1)}{c(\lambda + 1)(\lambda^2 + 1)},$$
$$B_{1r} = -\frac{4\pi j_0}{c(\lambda + 1)}z, \quad B_{1z} = \frac{4\pi\lambda j_0}{c(\lambda + 1)}q.$$

Supposing for the case of a moving toroidal pinch that $q = r - a$, we determine the function ψ in the vicinity of the magnetic axis:

$$\psi \approx \frac{1}{2}\psi_0 R^2 L^2\left[\frac{z^2}{b^2} + \left(\frac{qR}{aD}\right)^2\right].$$

Thus, the cross section of the magnetic surface represents an ellipse with the semiaxes b and $d = a\frac{D}{R}$. For the time-dependent solution, the density of the electric current flowing in the pinch and plasma pressure are functions of time:

$$j_\varphi = -j\frac{r}{a}, \quad j = j_0(1+\mu^2)\frac{DL^2}{\alpha d b^2}, \tag{14}$$

$$p = Q\frac{1+\mu^2}{\alpha}\left(\frac{LD}{bd}\right)^2\left(1 - \frac{q^2}{d^2} - \frac{z^2}{b^2}\right). \tag{15}$$

Here, $\mu = \frac{b}{d}$ is the ratio of the cross-section semiaxes.

We find for the magnetic field of a thin pinch

$$B_r = -\frac{4\pi j_0 DL^2}{\alpha c d b^2}z, \quad B_z = \beta\frac{D^2}{d^2} - \frac{4\pi j_0 DL^2}{\alpha c d^3}q. \tag{16}$$

We now represent magnetic field (16) in the form similar to (13)

$$B_{0r} = \kappa z, \quad B_{0z} = \kappa q, \quad \kappa = \frac{4\pi j\mu(\mu-1)}{c(\mu+1)(\mu^2+1)}, \tag{17}$$
$$B_{1r} = -\frac{4\pi j}{c(\mu+1)}z, \quad B_{1z} = \frac{4\pi\mu j}{c(\mu+1)}q.$$

Thus, in the case of a thin toroidal pinch, the solution obtained describes the time dependence of both the radius $a = \frac{Rd}{D}$ and the sizes b and d of the pinch cross-section with the variation of certain physical quantities. They are electric current (14) flowing in the pinch, plasma pressure (15), and external magnetic fields required to confine the plasma, i.e., quadrupole-type field (17) and the homogeneous field.

It is worth mentioning that the radial component of the plasma can be represented in the form $V_r = \dot{a} + \frac{q\dot{d}}{d}$, i.e., the ratio $\frac{q}{d}$ is a self-similar variable to within first-order-term accuracy. Therefore, the results obtained for the thin toroidal pinch correspond to solutions of magnetohydrodynamic equations in the framework of the self-similar approximation. This approach was applied previously in the study of electron-ring dynamics [5].

REFERENCES

1. L. I. Sedov, *Similarity and Dimensionality Methods in Mechanics* (Nauka, Moscow, 1981).
2. A. G. Kulikovskiĭ and G. A. Lyubimov, *Magnetohydrodynamics* (Fizmatgiz, Moscow, 1962; Addison-Wesley, Reading, Mass., 1965).
3. V. D. Shafranov, Vopr. Teor. Plazmy, No. 2, 92 (1963).
4. L. Zakharov and V. Shafranov, Vopr. Teor. Plazmy, No. 11, 118 (1982).
5. N. D. Naumov, Dokl. Akad. Nauk **346**, 468 (1996) [Phys. Dokl. **41**, 50 (1996)].

Translated by G. Merzon

Doklady Physics, Vol. 48, No. 1, 2003, pp. 21–23. Translated from Doklady Akademii Nauk, Vol. 388, No. 3, 2003, pp. 320–322.

PHYSICS

Production and Properties of Europium Polytantalate Single Crystals

V. S. Vasil'ev*, M. M. Pinaeva, and G. F. Pinaev*****

Presented by Academician V.V. Osiko October 16, 2002

Received October 16, 2002

Europium polytantalate was first observed (when investigating an Eu_2O_3–Ta_2O_5 system [1, 2]) as a phase that is characterized by a narrow homogeneity range of 11–16 mol % Ta_2O_5 and undergoes peritectoid transformation into α-Ta_2O_5 and $EuTa_3O_9$ phases in the temperature range 1623–1673 K. Its X-ray and luminescence properties were examined with polycrystalline samples. As a result, this material was proposed as a red-glow luminophor [3]. Later, it was established that the polytantalate composition corresponds to the formula $EuTa_7O_{19}$ [4].

Ln_2O_3–Ta_2O_5 systems [where Ln = Y, Sc, or a rare earth element (REE)], along with individual phases that are formed in them (in particular, $LnTa_7O_{19}$), were investigated in [5–9], and their optical, dielectric, and magnetic properties were studied in [9–14]. Particular attention has been given to Eu^{3+}-, Tb^{3+}-, Tm^{3+}-, and Nd^{3+}-activated polytantalates that exhibit intense photoluminescence in red, green, and blue visible regions and the near-IR region, as well as anti-Stokes luminescence and cathodoluminescence. The production of REE polytantalates in the form of single crystals and films is of considerable interest in view of their applications as laser media, optical memory elements, in microelectronics, and for detecting X and γ rays.

The aim of this work is to produce $EuTa_7O_{19}$ single crystals and to investigate their properties.

We chose the method of growing $EuTa_7O_{10}$ single crystals from a solution in a V_2O_5 melt. This method was complicated, because the melt was multicomponent, and competing processes of crystallizing foreign phases could proceed. Therefore, it was necessary to preliminarily study the multicomponent system in order to establish the optimum composition of the melt and the temperature and concentration limits that ensure the production of desirable single crystals.

As a result, we developed the following method of obtaining $EuTa_7O_{19}$ single crystals [15]: a mixture of 10–16 mol % Eu_2O_3, 14–15 mol % Ta_2O_5, and 70–75 mol % V_2O_5 was heated in a closed platinum crucible up to 1073 ± 20 K and was held at this temperature for 10–15 h; further, it was heated to 1473 ± 10 K and was held at this temperature for 40–60 h. Finally, the mixture was cooled to room temperature at a rate of 1–5 K/h.

The resulting single crystals were separated from the crystallized melt by treating it in concentrated hydrochloric acid under heating and with further rinsing in water. The X-ray diffraction and optical microscopy analysis of the undissolved residual made it possible to identify phases $EuTa_7O_{19}$, transparent amber-colored 1 × 2-mm crystals (Fig. 1), and $EuVO_4$, trans-

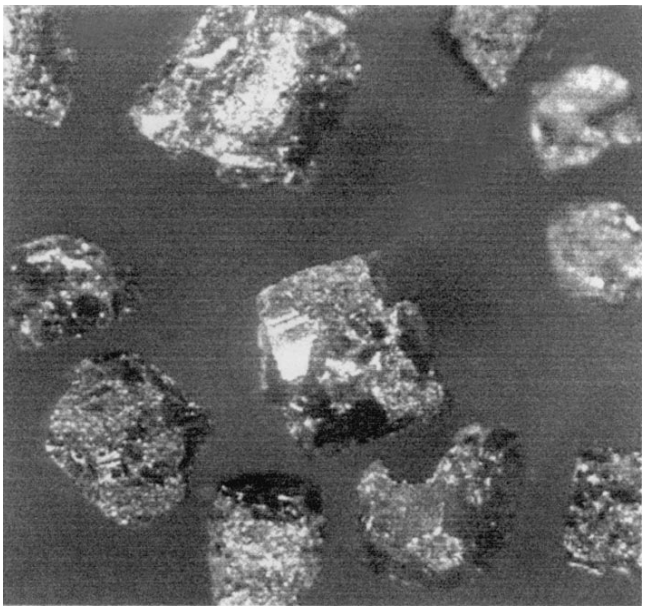

Fig. 1. $EuTa_7O_{19}$ single crystals.

* *University of Minnesota, Minnesota, USA*
e-mail: vladimir wasilyev@hanscom.af.mil

** *Belarussian State University of Informatics and Radio Electronics, ul. Brovki 17, Minsk, 220072 Belarus*
e-mail: vasokol@aw.bsuir.unibel.by

*** *Belarussian State Technological University, ul. Sverdlova 13a, Minsk, 220050 Belarus*
e-mail: root@bstu.unibel.by

1028-3358/03/4801-0021$24.00

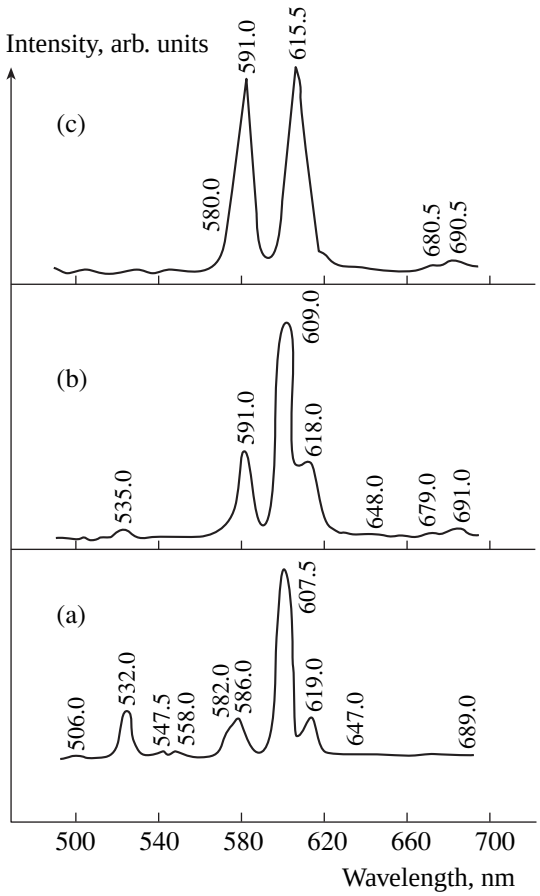

Fig. 2. Cathodoluminescence spectra of $EuTa_7O_{19}$ single crystals: (a) at 295 K and after annealing at (b) 1723 and (c) 1823 K.

parent colorless 3 × 2-mm crystals. In order to remove a possible V^{5+} impurity in the $EuTa_7O_{19}$ crystals, they were held in the flow of dry HCl at 873 K for 2 h and then at 1273 K for 2 h, but a noticeable decrease in crystal color was not observed.

Single crystals that were grown were identified by a Siemens D5005 diffractometer (CuK_α, λ = 0.5406 nm) and a Bruker AXS microdiffractometer. The parameters of a $EuTa_7O_{19}$ unit cell were determined by a SMART CCD diffractometer.

The surface morphology of the $EuTa_7O_{19}$ crystals was investigated with a scanning Hitachi S-800 microscope and a JEOL-840 microscope. The latter was also used for qualitative elemental analysis of the single crystals and products of their thermal treatment.

Photoluminescence of the $EuTa_7O_{19}$ single crystals was excited by the second harmonic of a Nd^{3+}:YVO_4 laser (λ = 532.25 nm), and cathodoluminescence was excited by the electron beam of the JEOL-840 microscope under voltage 10–40 kV and with a current density of 9 mA/m^2.

Spectra were recorded by a Mono CL2 "Cambridge" spectrometer with a monochromator resolution of 0.5 nm and a measurement accuracy of ±0.2 nm.

Our results indicate that the $EuTa_7O_{19}$ crystals have a block structure and are susceptible to twinning. In agreement with the data from [4], a unit cell is hexagonal and at 298 K has the parameters a = 0.621 nm, c = 1.998 nm, V = 0.66812 nm^3, ρ = 8420 kg/m^3, and Z = 2. Similar to $CeTa_7O_{19}$ crystals [5], we observed intragrowth needle-shaped Ta_2O_5 inclusions that could not be detected by X-ray analysis.

Analysis of the X-ray diffraction patterns of the single crystals under investigation shows that $EuTa_7O_{19}$ retains its crystalline structure up to 1623 K. Its peritectoid transformation into α-Ta_2O_5 and $EuTa_3O_9$ phases begins at 1723 K and completes at 1823 K. The crystals becomes turbid, acquire a milky yellow color, and melt in the temperature range 1823–1873 K.

The photoluminescence spectrum of $EuTa_7O_{19}$ single crystals is similar to those described earlier in [4, 9, 10, 14] for polycrystalline samples, which testifies to their chemical and phase identity. However, the $^5D_0$–$^7F_1$, $^5D_0$–$^7F_3$, and $^5D_0$–$^7F_4$ electron transitions of a Eu^{3+} ion in single crystals are better resolved than those in polycrystalline samples. The symmetry of the Eu^{3+} luminescence center correlates with the hexagonal symmetry of the crystal cell [9]. Upon heating a single-crystal sample up to 1623 K, weak 617- and 596-nm lines, which are characteristic for the Eu^{3+} luminescence center in $EuTa_3O_9$ [10], appear in the photoluminescence spectrum. As the sample is further heated, these lines dominate in the spectrum, whereas the intensity of the strongest 610-nm line in the $EuTa_7O_{19}$ spectrum decreases significantly. This behavior is an additional manifestation of the peritectoid transformation of polytantalate.

Compared to the photoluminescence spectrum of $EuTa_7O_{19}$ single crystals, all the lines of their cathodoluminescence spectrum (Fig. 2a) are shifted towards short wavelengths and broadened, and new 547- and 558-nm lines appear with the simultaneous disappearance of the 590- and 592-nm lines ($^5D_0$–$^7F_1$ transition). In addition, the relative intensity of the 610-nm line (the $^5D_0$–$^7F_2$ transition) decreases noticeably due to the change both in the character of charge transfer Eu^{3+} □ O^{2-} and in the structure of the luminescence center. The broadening of the cathodoluminescence spectral lines testifies to the appearance of lattice defects and oxygen vacancies, whose concentration most likely depends on the stream of high-energy electrons capable of forming new luminescence centers rather than on the conditions of crystal growth.

Comparison between Figs. 2a and 2c shows that, as in the case of photoluminescence, the spectrum of $EuTa_7O_{19}$ single crystals after annealing at 1823 K does not contain polytantalate spectral lines but represents a

Eu^{3+} spectrum in $EuTa_7O_{19}$. The spectrum shown in Fig. 2b contains spectral lines from both Figs. 2a and 2c and therefore characterizes an intermediate stage of the peritectoid transformation of $EuTa_7O_{19}$.

Cathodoluminescence intensity decreases with an increase in the treatment temperature of $EuTa_7O_{10}$ samples. With an increase in the accelerating voltage, the form of the cathodoluminescence spectra changes only slightly. Cathodoluminescence intensity increases insignificantly in the range V = 10–20 kV. In contrast, it increases sharply in the range V = 20–40 kV without saturation, which is of interest for practical usage of $EuTa_7O_{19}$ as a cathodoluminescent material.

ACKNOWLEDGMENTS

We are grateful to Prof. L.E. Fransis for help in experiments.

REFERENCES

1. M. M. Pinaeva, E. I. Krylov, and V. M. Ryakov, Izv. Akad. Nauk SSSR, Neorg. Mater. **3** (9), 1612 (1967).
2. M. M. Pinaeva, E. I. Krylov, and V. M. Ryakov, Izv. Akad. Nauk SSSR, Neorg. Mater. **4** (7), 1118 (1968).
3. M. M. Pinaeva and E. I. Krylov, Inventor's Certificate No. 199305, Byull. Izobret., No. 15/67 (1967).
4. V. S. Vasil'ev and M. M. Pinaeva, Zh. Neorg. Khim. **25** (4), 900 (1980); ASTM PDF-card 35-1191.
5. R. C. Roth, T. Negas, H. S. Parker, *et al.*, Mater. Res. Bull. **12**, 1173 (1977).
6. B. M. Gatehouse, J. Solid State Chem. **27**, 209 (1979).
7. B. Langenbach-Kuttert, J. Sturm, and R. Gruehn, Z. Anorg. Allg. Chem. **54** (3), 117 (1986).
8. U. Schaffrath and R. Gruehn, Z. Anorg. Allg. Chem. **58** (8), 43 (1990).
9. M. M. Pinaeva, V. V. Kuznetsova, V. S. Vasil'ev, S. F. Shkirman, and V. A. Svetlova, Zh. Prikl. Spektrosk. **27** (3), 442 (1997).
10. V. V. Kuznetsova, M. M. Pinaeva, and V. S. Khomenko, Zh. Prikl. Spektrosk. **13** (4), 733 (1970).
11. J. C. Michel, D. Morin, G. Primot, and F. Azel, C.R. Seances Acad. Sci., Ser. B **284**, 555 (1977).
12. M. G. Zuev, E. I. Yashin, F. A. Rozhdestvenskiĭ, and E. I. Krylov, J. Lumin. **21** (2), 217 (1980).
13. M. G. Zuev, E. D. Politova, and S. Yu. Stefanovich, Zh. Neorg. Khim. **36** (6), 1540 (1991).
14. S. Kubota, H. Yamane, M. Shimada, *et al.*, J. All. Comp. **275/277**, 746 (1998).
15. V. S. Vasil'ev and M. M. Pinaeva, Inventor's Certificate No. 873680, Byull. Izobret., No. 38/81 (1981).

Translated by Yu. Vishnyakov

Doklady Physics, Vol. 48, No. 1, 2003, pp. 24–29. Translated from Doklady Akademii Nauk, Vol. 388, No. 3, 2003, pp. 323–328.

PHYSICS

Cavitation and Thermonuclear Fusion. Estimates of the Parameters and a Possible Method of Obtaining Positive Energy Balance

V. A. Namiot

Presented by Academician V.L. Ginzburg August 19, 2002

Received August 23, 2002

The possibilities of generating thermonuclear neutrons at the collapse of cavitation cavities filled with a gas including deuterium or deuterium–tritium mixture are simply estimated. Some possibilities of increasing this neutron yield are discussed. However, a positive energy balance in ordinary (spherical) cavitation is estimated as impossible. A new approach is proposed that is based on so-called cylindrical cavitation and can in principle ensure a positive energy balance. In this approach, cavitation is used to recover thermal energy lost by a tritium ion beam in a deuterium target rather than to generate neutrons in the process of collapse.

Interest in the possible use of cavitation in the problem of controlled thermonuclear fusion was initiated by work [1], where thermonuclear neutrons were likely observed when cavitation cavities collapsed in a liquid involving deuterium. (There were earlier studies where such a possibility was discussed at least as a hypothesis and neutron yield was even measured [2], but a definite relation to cavitation was not established [2, 3, 15].)

This study aims to simply estimate the possibilities (and implicitly corroborate the results of [1]) and methods of increasing neutron yield and to suggest a method (based on so-called cylindrical cavitation [4, 5]) that can in principle ensure a positive energy balance.

1. ESTIMATES CONCERNING ACOUSTIC CAVITATION

The problem of the collapse of an empty cavitation cavity in inviscid incompressible fluid was first considered by Rayleigh [6], who obtained the following expressions for the collapse rate (velocity of the cavity boundary) $\dot{R}(R)$ and pressure $P(r, R)$:

$$\dot{R}(R) = \sqrt{\frac{2P_0}{3\rho_0}\left(\frac{R_0^3}{R^3} - 1\right)}, \quad (1)$$

$$P(r, R) = P_0\left(1 - \frac{R}{r}\right) + \frac{\rho_0(\dot{R}(R))^2}{2}\left(\frac{R}{r} - \frac{R^4}{r^4}\right), \quad (2)$$

where P_0 is the pressure applied to the fluid, ρ_0 is the fluid density, and R_0 is the initial radius of the cavity. As an estimate, Eq. (1) can be easily obtained in the approximation $R_0^3 \gg R^3$ as follows. The energy E_n released when the cavity collapses is equal to about $P_0R_0^3$. For an inviscid incompressible fluid, this energy transforms entirely to the kinetic energy of the fluid E_k. The mass and velocity of the moving fluid are about ρ_0R^3 and $\dot{R}(R)$, respectively. The condition $E_n \approx E_k$ takes the form

$$P_0R_0^3 \approx \rho_0R^3(\dot{R}(R))^2, \quad (3)$$

which agrees with Eq. (1) up to a factor of $\sqrt{\frac{2}{3}}$.

The viscosity effect was considered by Zababakhin [7]. To estimate this effect, it is reasonable to evaluate energy E_ν dissipated in the fluid due to viscosity. According to [7, 8], we have

$$E_\nu = 16\pi\eta\left|\int_{R_0}^{R} R\dot{R}(R)dR\right| \sim 32\pi\eta\sqrt{\frac{P_0}{\rho_o}}R_0^2, \quad (4)$$

where η is the fluid viscosity. The viscosity effect is substantial and negligible when $E_\nu \geq E_n$ and $E_n \gg E_\nu$, respectively. The latter condition is satisfied for low-viscosity fluids (water, mercury) at $P_0 > 1$–10 atm and $R_0 \sim 10^{-3}$–10^{-4} m.

The stability of collapse was analyzed by Birkhoff [9], who showed that the deviation from the spherical

Skobel'tsyn Institute of Nuclear Physics, Moscow State University, Vorob'evy gory, Moscow, 119899 Russia

1028-3358/03/4801-0024$24.00

shape δR (Fig. 1) increases slowly as $R^{-1/4}$ with collapse of the cavity. This dependence can be qualitatively obtained as follows. Let us consider the proper coordinate system, where the surface of the undisturbed sphere is at rest. There is a force directed against deviation δR, which must therefore satisfy the following oscillator equation with variable coefficients:

$$M'(R)(\delta\ddot{R}) = -K(R)(\delta R), \quad (5)$$

where $M'(R) \sim \rho_0 R^3$ and $K(R) \sim M'(R)\left(\frac{\dot{R}(R)}{R}\right)^2$ according to dimensions. The estimate of δR can be obtained in the adiabatic approximation (although, strictly speaking, this is insufficiently correct); i.e., $M'(R)$ and $K(R)$ are assumed to vary slowly enough to conserve the adiabatic invariant. In this case,

$$\delta R \sim \delta R(0)\left|\left(\frac{K(R)}{M'(R)}\right)^{1/2} K^{-1}(R)\right|^{1/2} \sim \sigma R(0)\left(\frac{R_0}{R}\right)^{1/4}. \quad (6)$$

This slowly developed instability at small initial perturbations likely does not restrict the collapse of the cavity.

The effect of fluid compressibility. In contrast to the collapse of an empty cavity in an incompressible fluid, when all the energy is transferred to a small mass $\sim\rho_0 R^3$, the basic part of the energy release in this case is spent on the compression of the fluid outside of this small region. Correspondingly, the compressibility of the fluid significantly weakens cumulation but does not eliminate it.

The collapse of an empty cavity in water was analyzed by Hunter [10] (see also [8, 11]), who took into account compressibility but ignored viscosity. The equation of state was taken in the form $P = B\left(\frac{\rho}{\rho_0}\right)^\nu$, where $B = 3000$ atm, $\nu = 7$, and ρ is the fluid density, which is similar to the gas case. The numerical solution to the problem was shown to become self-similar (as was expected [11]) for small R when the velocity of walls considerably exceeds the speed of sound. In this case, energy E_R in a region of about R behaves as $R^{5-\frac{2}{\alpha}}$, where $\alpha \approx 0.545$; i.e.,

$$E_R \approx E_n\left(s\frac{R}{R_0}\right)^{5-\frac{2}{\alpha}} \approx P_0 R_0^3\left(s\frac{R}{R_0}\right). \quad (7)$$

Here, $s \approx \frac{R_0}{R_C}$, where R_C is the cavity radius from which the asymptotic formulas of the self-similar mode are applicable. This radius can be estimated from the condition $\dot{R}(R_C) \approx c'$, where c' is the speed of sound in the fluid and $\dot{R}(R)$ is determined by Eq. (1). For $P_0 \geq 10$ atm, s is about 2–5, and $s = 1$ can be taken for estimates, because the equation of state is also approximate. For other fluids and other equations of state, α can vary, but Eq. (7) (and $s = 1$) can be used at least as a crude estimate even in these cases.

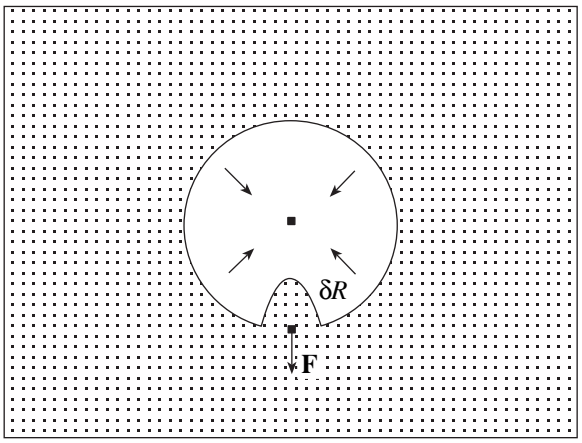

Fig. 1. Collapse of a spherical cavity, where δR is a disturbance on the surface and **F** is the force acting on the disturbed surface.

Cavity filled with a gas. At least at the initial stages of the collapse of a cavity filled with a gas unsolvable in the fluid, when nonlinear thermal conductivity is immaterial, the heating of the gas in the cavity can be considered as adiabatic [8]. In this case, the temperature and density of the substance in the cavity at the time when the walls stop can be determined from the condition

$$E_R \sim k_B T_k N \sim k_B T_0 N\left(\frac{R_0}{R_k}\right)^2, \quad (8)$$

where N is the number of gas particles in the cavity; k_B is the Boltzmann constant; T_0 and T_k are the initial and final temperatures, respectively; and R_k is the final radius of the cavity. Substituting Eq. (7) into Eq. (8), we find that the particle density at the time of collapse is

$$n_k \sim \frac{N}{R_k^3} \sim \frac{P_0}{k_B T_0}. \quad (9)$$

In particular, n_k can reach a value of 10^{29} m^{-3} for very high acoustic pressure $P_0 \sim 10^3$ atm and $T_0 \sim 10^{-2}$ eV and is lower by two to three orders of magnitude for normal acoustic pressures 1–10 atm.

Heat losses caused by electron thermal conductivity are the most dangerous form of heat losses, which restrict the maximum temperature of a plasma in a cavity. According to [11], the effective electron thermal conductivity can be written as $\left(\frac{\chi}{Z\Lambda}\right)T^{5/2}$, where $\chi \sim 10^{-10}$ J/(s m K), Z is the ion charge, Λ is the Coulomb

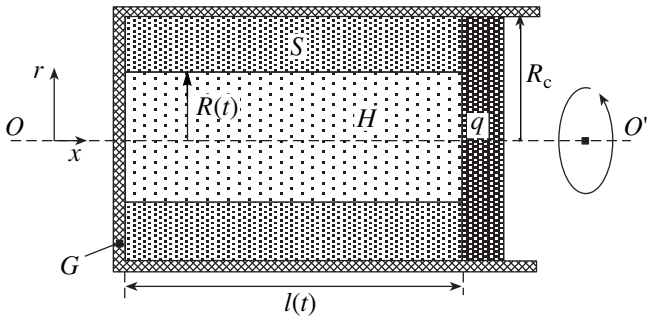

Fig. 2. Layout of cylinder G that has radius R_c and is filled with fluid S, where a cavity with radius $R(t)$ is filled with gas H; q is the piston whose position is specified by function $l(t)$.

logarithm, and T is the temperature. Equating E_R to the heat flux to walls during the time

$$\tau \sim \left(\frac{R_k}{\dot{R}(R_k)}\right) \sim \sqrt{\frac{\rho_0}{P_0}}\left(\frac{R_k}{R_0}\right)^{1/\alpha} R_0 \sim \sqrt{\frac{\rho_0}{P_0}}\left(\frac{R_k}{R_0}\right)^2 R_0$$

of the existence of the heated region, we obtain

$$T_k \le \left(\sqrt{\frac{P_0}{\rho_0}}\frac{P_0 R_0 Z\Lambda}{\chi T_0}\right)^{2/5}. \quad (10)$$

In particular, $T_k \le 10^3$ eV for $Z \sim 10$, $\Lambda \sim 10$, $P_0 \sim 10^3$ atm, $R_0 \sim 10^{-3}$ m, and $T_0 \sim 10^{-2}$ eV. Correspondingly, the estimate

$$N \sim n_k R_0^3 \left(\frac{T_0}{T_k}\right)^{3/2} \quad (11)$$

yields ~10^{12}–10^{13} in this case.

Neutron yield per cavitation collapse is estimated as

$$N_n \sim n_k N' \tau \langle \sigma v \rangle|_{T = T_k}, \quad (12)$$

where $\langle\sigma\rangle$ is the effective reaction cross section, $\langle v\rangle$ is the relative velocity of nuclei, and their product is averaged over the velocity distribution [12]. For the conditions described in [1], $N_n \sim 0.1$ even in the optimal case, which can likely be observed in experiment.

Method of increasing the neutron yield. The situation can be substantially improved in the case where a deuterium–tritium gaseous mixture is blown through a liquid metal (e.g., mercury) taken as a fluid in which cavitation is created and acoustic pressure is strongly increased up to (2–3) × 10^3 atm at the focus. In this case, N_n can reach 10^5 under the optimal conditions.

Energy balance. The conclusion on such a device as a setup with a positive energy balance rather than as a generator of neutrons is pessimistic. Comparing $E_{tot} = N_n E'$, where E' is the energy release per neutron, with E_n, we conclude that $\frac{E_{tot}}{E_n}$ is much less than unity (it is equal to about 10^{-5} or less) even in the optimal case, where neutrons release additional energy in the corresponding blanket surrounding the system. Thus, in order to obtain a positive energy balance (if it is possible), the cavitation scheme of the controlled thermonuclear fusion must be fundamentally changed. This change is discussed below.

2. CYLINDRICAL CAVITATION, ENERGY RECUPERATION, AND HYBRID THERMONUCLEAR FUSION

At present, thermonuclear neutrons can be obtained most simply by bombarding a deuterium target with tritium ions accelerated up to an energy of ~150 keV. Even if neutrons produced in the D–T reaction release additional energy in the natural-uranium blanket, energy spent on the heating of the target for the ionization of deuterium is higher than this total energy release. However, this excess is not so high and is equal to a factor of 3 for the optimal case. Therefore, this process can be made energy-profitable according to Carnot's theorem $K' \le \frac{T_f - T_i}{T_f}$, where T_f and T_i are the temperatures of the heater and cooler, respectively, by recovering energy spent on heating the target with the recovery factor K' exceeding 0.75. Thus, it is sufficient to ensure $T_f \sim 2000$ K (which is much lower than the melting temperature for molybdenum and the more so for tungsten) for the optimal case with $T_i \sim 300$–400 K.

As was shown in [4, 5], the cavitation process can be of interest for controlled thermonuclear fusion, not only as a method of reaching thermonuclear temperatures for a short time, but also as a method of recovering thermal energy with very high recovery factor K'. Indeed, the collapse of a cavitation cavity is accompanied by the adiabatic compression and heating of the gas up to sufficiently high (above several electronvolts) temperatures [8], although the initial gas temperature, as well as the temperature of the fluid, is close to room temperature during the whole process. Correspondingly, if one could feed additional heat into the cavity when it collapses and remove heat from the cavity when it expands, this temperature difference would ensure $K' \ge 0.95$–0.98. However, the real method of such a feed and removal of heat for ordinary (spherical) cavitation has not yet been proposed. In spite of this circumstance, we can consider an unusual cavitation process, so-called cylindrical cavitation [4, 5], where such a possibility could be realized at least in principle. In this case, only $K' \sim 0.8$–0.9 can be expected, but it is sufficient for a positive energy balance.

Cylindrical cavitation is the process of the collapse and expansion of a cylindrical cavity in a rotating fluid in a cylinder, where a piston moves (Fig. 2). This pro-

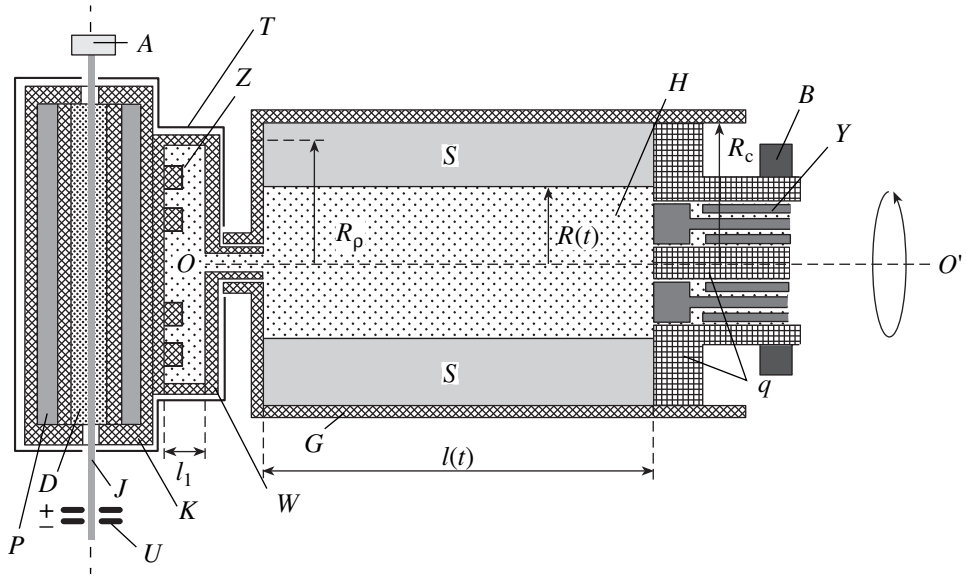

Fig. 3. Possible layout of the device under consideration: *A* is the source of accelerated tritium ion beam *J*, *D* is the deuterium gas, *P* is the blanket, *K* is the case, *T* is the heat-storage enclosure, *W* is the operating chamber of width l_1, *G* is a rotating cylinder of radius R_c, *S* is the fluid, $R(t)$ is the time-dependent cavity radius (R_ρ is the radius at the time of the maximum expansion), *H* is the working gas filling the cavity and chamber *W*, *q* is the piston whose position is specified by function $l(t)$, *Y* is the inlet–outlet valve automatically synchronized with the motion of the piston, *B* is the permanent magnet of the system for the direct transformation of the energy of piston motion to electrical energy (coils of this system are not shown), *U* is the compensator of beam-energy losses, and *Z* are wall protrusions for the initiation of the controlled turbulent mode.

cess is similar to the convenient cavitation. In particular, the collapse rate increases with decreasing radius [4], fluid viscosity is immaterial in most cases, the gas in the cavity is compressed adiabatically, the ratio of the initial to final volumes can be so large that T_f can substantially exceed T_i, etc. However, there are differences. In particular, the collapse of a cylindrical cavity, in contrast to a spherical one, is stable [4]. The energy of the moving fluid can be transmitted to the piston and then transformed to electrical energy. (For ordinary cavitation, this energy can be associated with turbulent motion, which considerably hinders its utilization.) Finally, the direct contact of the cavity with the piston and cylinder end makes it possible to comparatively easily feed and remove a substance and energy into and from the cavity through corresponding holes and valves at the required times.

Figure 3 shows one of the possible layouts of such a device, which could be used to recover energy released in a hybrid thermonuclear system. A tritium ion beam that is created by source *A* and accelerated up to an energy of ~150 keV passes through low-density deuterium gas *D*, whose density is chosen so that tritium ions lose ~20–30 keV over the length of chamber *K*. Generated neutrons release additional energy in blanket *P*. This energy, along with energy lost by the beam in *D*, is spent on heating working gas *H* (e.g., a light inert gas such as helium, neon, or argon) in chamber *W* connected with case *K* containing the blanket.

Let us discuss the recovery of energy. Chamber *G* is partially filled with fluid *S* and rotates about the *O*–*O*' axis. This rotation gives rise to the formation of a cylindrical cavity at the center of the chamber. As piston *q* moves in the chamber, cavity radius $R(t)$ varies with time. When the piston enters the cylinder, the cavity collapses, and the gas in it and in chamber *W* is compressed and heated adiabatically [4, 5]. Correspondingly, the cavity is expanded adiabatically at the reverse motion of the piston, and the gas in the cavity liberates its energy to the fluid and piston. At the time of maximum expansion t_i, valve *Y* is opened, and the working gas is partially replaced by a cooler gas. The gas removed from the cavity is then also cooled and used again.

The problem of feeding heat released in deuterium and in the blanket into the working gas is most difficult. This heat must be fed only during a short time interval near the collapse time t_f, when the working gas is maximally heated. The heat capacity of the blanket is too high to substantially change its temperature for such a short time. On the other hand, the gas thermal conductivity χ_H is sufficiently low and varies relatively slightly during the entire operating cycle. Therefore, the compression of the gas in the process of collapse is adiabatic [4]. Thus, it seems impossible to transfer heat from heated chamber walls *W* to gas *H* during a short time interval, when the gas is maximally heated.

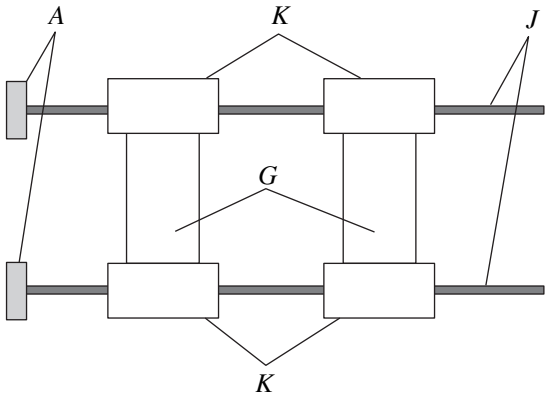

Fig. 4. *A* are sources of fast ion beams *J*, *K* are chambers for deuterium that are surrounded by the blanket, *G* are coupled recovery systems such as that shown in Fig. 1 (pistons of the systems are joined with each other, and, when the gas is compressed in one of systems, it expands in the other system and vice versa).

Nevertheless, this problem can be solved. For the laminar mode of gas motion, heat flux from the walls of chamber *W* to the gas is estimated as

$$S_{T(\text{lam})} \sim \chi_H \frac{\delta T}{l_1} S'_W, \tag{13}$$

where δT is the temperature difference between the walls and gas and l_1 and S'_W are the thickness and area of the walls of chamber *W*, respectively. In the case of developed turbulence, the heat flux is determined as

$$S_{T(\text{turb})} \sim k_B n_H \delta T v_{\text{turb}} S'_W, \tag{14}$$

where n_H is the density of gas *H* and v_{turb} is the characteristic velocity of turbulent motion and is determined by the velocity of directed motion at the passage to the turbulent mode, i.e., by the velocity

$$v_H(t) \approx \frac{2V_W R(t) l(t) \dot{R}'(t)}{R_1^2[\pi R^2(t) l(t) + V_W]} \tag{15}$$

with which the gas enters chamber *W*, where R_1 is the radius of the hole connecting chamber *W* with *G*, V_W is the volume of chamber *W* and $\dot{R}'(t)$ is the collapse rate of the cylindrical cavity. According to [4], $\dot{R}'(t)$ is estimated as

$$\dot{R}'(t) \approx \sqrt{\frac{P'}{\rho_0}} \frac{R_\rho}{R(t)}, \tag{16}$$

where P' is the pressure applied to the piston. In particular, $v_H(t)$ can reach ~(0.1–0.2)v_T, where v_T is the thermal velocity of atoms of gas *H*, near the time of collapse when $\frac{2V_W R(t) l(t)}{R_1^2[\pi R^2(t) l(t) + V_W]} \sim 2$–3 and $\dot{R}'(t) \sim 10^2$ m/s. Correspondingly, $S_{T(\text{turb})}$ can be higher than $S_{T(\text{lam})}$ by three to four orders of magnitude for $n_H \geq 10^{27}$ m^{-3}. Therefore, if one creates the conditions for the laminar motion of gas *H* during almost the entire operating cycle but the motion becomes turbulent near the collapse time, the gas is heated exactly at this time.

The turbulent mode arises formally when the Reynolds number of this flow exceeds a certain critical value R_{cr} [13]. In the case under consideration, the Reynolds number has the form

$$R_R = \frac{l_1 v_H(t) \rho_H(t)}{\eta}, \tag{17}$$

where $\rho_H(t)$ and η are the density and viscosity of gas *H*. The Reynolds number given by Eq. (17) reaches its maximum R_M at a time close to t_f (which is required in the case under consideration). For the transition to turbulence, the inequality $R_M > R_{\text{cr}}$ must be satisfied. One can control the R_{cr} value by varying the shape of chamber *W* or by introducing additional protrusions on the walls of the chamber.

The physical cause for changing the conditions of the transition to the turbulent mode due to the introduction of protrusions on the surface of chamber *W* is as follows. Chamber *W* can be treated as an acoustic cavity. The introduction of protrusions on the surface changes the phase velocity v_f of waves induced in it. In particular, it can be made much lower than the speed of sound in the gas. If $v_H(t)$ exceeds v_f, acoustic oscillations build up near t_f. When their amplitude becomes sufficiently high, the transition to the turbulent mode occurs. (Various other methods of initiating the transition to turbulence can be proposed.)

We discuss now the problem of optimizing energy expenses for the generation of neutrons. As fast ions move through deuterium, their energy decreases from the optimal value, which gives rise to a substantial decrease in the cross section σ_{DT} for the *D*–*T* reaction. Therefore, energy release decreases, whereas energy expenses remain. In order to avoid this behavior, it is necessary to compensate energy loss. Fast tritium ions are removed from the deuterium gas when cross section σ_{DT} is close to its maximum value and fall into capacitor *U*, where they are additionally accelerated to the optimum energy. Then, they fall into the next unit (Fig. 4), where they again pass through the deuterium gas, and so on. The total number of units *N*' is limited by the voltage that must be applied to capacitors compensating energy losses. To avoid an increase in the energy spread of fast ions, the condition

$$\left.\frac{dP'_H(E)}{dE}\right|_{E = E_1} > 0 \tag{18}$$

must be satisfied, where $P'_H(E)$ is the mass stopping power of a hydrogen ion of energy *E* in the molecular hydrogen medium and E_1 = 50 keV. According to data presented in [14], condition (18) is satisfied. In addi-

tion, the case $N' \gg 1$ is interesting, because the requirements for a source of fast ions can be weakened. Energy loss at acceleration is efficiently decreased by a factor of N'.

ACKNOWLEDGMENTS

I am grateful to V.I. Kogan and L.G. Golubchikov for numerous stimulating discussions.

REFERENCES

1. R. P. Taleyarkhan, C. D. West, J. S. Cho, *et al.*, Science **295**, 1868 (2002).
2. U. Fisher, H. Jager, and W. Lochte-Holtgreven, in *Proceedings of the VI European Conference on Controlled Fusion and Plasma Physics, 30 July–4 August, Moscow, 1973*.
3. A. I. Koldamasov, *Report on RKKhSTYa-3, Dagomys, Sochi, 1995*.
4. V. A. Namiot, Phys. Lett. A **257**, 99 (1999).
5. V. A. Namiot, Phys. Lett. A **299**, 418 (2002).
6. J. W. S. Rayleigh, Philos. Mag. **34**, 84 (1917).
7. E. I. Zababakhin, Prikl. Mat. Mekh. **24** (6) (1960).
8. A. D. Pernik, *Cavitation Problems* (Sudostroenie, Leningrad, 1966).
9. G. Birkhoff, Q. Appl. Math. **13** (4) (1956).
10. C. Hunter, J. Fluid Mech. **8**, 241 (1960).
11. Ya. B. Zel'dovich and Yu. P. Raizer, *Elements of Gas Dynamics and the Classical Theory of Shock Waves* (Nauka, Moscow, 1966; Academic, New York, 1968).
12. L. A. Artsimovich, *Controlled Thermonuclear Reactions* (Fizmatgiz, Moscow, 1963; Gordon and Breach, New York, 1964).
13. L. D. Landau and E. M. Lifshitz, *Course of Theoretical Physics*, Vol. 6: *Fluid Mechanics* (Nauka, Moscow, 1986; Pergamon, New York, 1987).
14. *Handbook of Physical Quantities*, Ed. by I. S. Grigoriev and E. Z. Meilikhov (Énergoatomizdat, Moscow, 1991; CRC Press, Boca Raton, 1997).
15. A. P. Andreev, D. S. Baranov, *et al.*, *Report on RKKhSTYa-8, Dagomys, Sochi, 2000*.

Translated by R. Tyapaev

Doklady Physics, Vol. 48, No. 1, 2003, pp. 30–33. Translated from Doklady Akademii Nauk, Vol. 388, No. 1, 2003, pp. 46–50.

TECHNICAL PHYSICS

Solid-State Synthesis and Martensitic Transformations in Thin Films

V. G. Myagkov[1,*], L. E. Bykova[1], and G. N. Bondarenko[2]

Presented by Academician V.V. Osiko September 23, 2002

Received September 12, 2002

At present, martensitic transformations are considered as a diffusionless transition of the high-temperature austenitic phase to the low-temperature martensitic phase. Since this transition proceeds through the collective displacement of atoms without the rearrangement of chemical bonds, martensitic transformations can occur at extremely low temperatures. The crystallographic aspects of martensitic transformations and microstructure of the martensitic phase are well studied (see, e.g., [1]). In contrast, chemical mechanisms are poorly studied, primarily because experimental data concerning the origin of the formation of a chemical bond and martensitic transformations are not available. In addition, distinct concepts of the chemical mechanisms of solid-state reactions are also absent. Solid-state reactions in thin films proceed at temperatures of 400–800 K, which are lower than the corresponding temperatures for bulk samples by 400–600 K. Diffusion along the edges of grains is the primary cause responsible for large mass transfer accompanying low-temperature reactions in thin films (see [2, 3] and references therein). The diffusion mass-transfer mechanism with Arhenius temperature dependence of diffusion implies that solid-state reactions at the film interfaces must proceed at any temperature, and the thickness of the reaction products depends only on temperature and annealing time. However, numerous investigations indicate that a phase that is called the first phase is first formed at the film interface at a certain temperature T_0 (initiation temperature). A further increase in annealing temperature gives rise to the appearance of new phases with the formation of a phase sequence (see, e.g., [3]). From the fundamental and practical viewpoints, it is important to know (i) which phase among numerous phases of a given binary system is formed first and (ii) what factors determine the initiation temperature T_0 for the first phase.

Although various rules and their modifications are proposed to predict the first phase [3], no general rule of the first phase explains the entire set of experimental data.

In [4], it was shown that the solid-state synthesis in thin films for high heating rates $\eta > \eta_{cr}$ can proceed as self-propagating high-temperature synthesis (SHS), which has the form of a surface combustion wave in thin films. Therefore, solid-state reactions in thin films can proceed both as an SHS wave for $\eta > \eta_{cr}$ and as reaction diffusion for $\eta < \eta_{cr}$. It was shown for the first time in [5, 6] that

(i) a phase with the minimum temperature of solid-phase transformation according to the phase-equilibrium diagram is first formed at the interface of two film condensates and

(ii) the initiation temperature T_0 of the solid-state reaction in thin films coincides with the solid-phase-transformation temperature T_K of the first phase ($T_0 = T_K$).

In particular, the initiation temperature T_0 of the solid-state reaction in the S/Fe two-layer thin-film system coincides with the temperature of the metal–insulator phase transition in the iron monosulfide, i.e., $T_0(S/Fe) = T_K(FeS)$ [5]. For the Au–Cu system classical in the ordered state, the initiation temperature T_0 of the solid-state reaction in Cu/Au two-layer films coincides with the Kurnakov temperature of the order–disorder transition in the CuAu alloy, i.e., $T_0(Cu/Au) = T_K(CuAu)$ [6]. Further investigations unambiguously showed that the Kurnakov temperature for many superstructures well studied in the ordered state determines the initiation temperature T_0 of the solid-state reaction in the corresponding two-layer film system. The structure mechanism of the above solid-phase transformations (metal–insulator and order–disorder) is determined by diffusion. For martensitic diffusionless transformations, where chemical bonds are not broken and diffusivity is extremely low, atomic transport is not very large, and compounds are not likely to be formed

[1] *Kirenskiĭ Institute of Physics, Siberian Division, Russian Academy of Sciences, Akademgorodok, Krasnoyarsk, 660036 Russia*

[2] *Institute of Chemistry and Chemical Technology, Siberian Division, Russian Academy of Sciences, Krasnoyarsk, Russia*

* *e-mail: miagkov@iph.krasn.ru*

1028-3358/03/4801-0030$24.00

at the martensitic-transformation temperature. However, solid-state reactions in Ni/Ti two-layer film samples surprisingly turned out to be initiated at the starting temperature A_S of the reverse martensitic transformation in titanium nickelide, i.e., $T_0(\text{Ni/Ti}) = T_K(\text{NiTi}) \sim 400$ K. This reaction was shown to be accompanied by the formation of martensitic phases in reaction products and to proceed in the reaction-diffusion mode up to heating rate $\eta \sim 20$ K/s [7].

The above-listed properties imply that the solid-state reaction in the Au/Cd film system must lead to the formation of martensite at the martensitic transformation temperature $T_K(\text{AuCd}) \sim 60$°C, because this temperature is the minimum temperature of the structural phase transformations in binary Au–Cd system.

The martensitic phases of AuCd alloy have attracted interest for 70 years, because they exhibit the shape memory effect and resinlike deformation, which is attributed to the processes of short atomic ordering of martensitic phases during aging at room temperature (see [8, 9] and references therein). It is known that, depending on content, the austenitic β_2 phase undergoes two martensitic transformations $\beta_2 \longrightarrow \gamma_2'$ and $\beta_2 \longrightarrow \zeta_2'$, where γ_2' is the orthorhombic phase for the Au–Cd 47.5 at. % alloy and ζ_2' is the trigonal phase with 49–52 at. % Cd. The lattice of γ_2' martensite is orthorhombic, the positions of atoms were continuously determined more precisely, and the crystal structure is now well known [10]. The structure of ζ_2' martensite is less studied. Refined data [11] indicate that the ζ_2' phase has the trigonal elementary cell. In the absence of reliable diffraction reflections from martensitic phases, diffraction reflections for the reaction products are determined according to the JCPDS database (cards 26-0256 and 26-0257).

In experiments, Au/Cd two-layer film samples deposited by vacuum sputtering at a pressure of 10^{-3} Pa on 0.18-mm thick glass substrates were used. To prevent reaction between Au and Cd films, these films were deposited at room temperature. The typical thickness of Cd and Au layers was ~100–250 and ~50–100 nm, respectively. The samples were heated at the rate $\eta \sim$ 5–10 K/s. The solid-state reaction between Au and Cd layers was actually initiated at $T_0(\text{Au/Cd}) = 340$ K and proceeded in the SHS mode, and front motion was easily visible. The propagation pattern of the reaction front was typical for two-layer film samples for which the SHS mode was realized. The electric resistance of the Au/Cd sample changed upon passing the SHS front (Fig. 1). The X-ray diffraction spectrum of the initial sample involves reflections only from the Au and Cd layers (Fig. 2a) and did not change upon 150-h annealing at 315 K. The diffraction pattern changed drastically as the SHS wave passed through the Au/Cd sample (Fig. 2b). The intensity of reflections from Au and Cd decreased, which testified to a reaction between Cd and Au layers. The analysis of diffraction reflections shown in Fig. 2b indicates that a mixture of the γ_2' and ζ_2' martensitic phases dominates in the reaction products. However, reflections with interplane distances d = 0.256 and 0.206 nm were not identified. These reflections can be attributed to intermediate martensitic phases arising due to the nonequilibrium synthesis process. A small amount of CdO was found in samples after the reaction. The remnant unreacted Cd layer also existed after the reaction. Therefore, the final reaction product is predominantly the $\gamma_2' + \zeta_2'$/Cd two-layer system consisting of the Cd film adjoining the substrate and the $(\gamma_2' + \zeta_2')$-martensite film. However, it is extremely surprising that the reaction can continue if an 80-nm Au layer is deposited on the upper surface of the reacted $\gamma_2' + \zeta_2'$/Cd sample. The SHS in such Au/$\gamma_2' + \zeta_2'$/Cd thin-film systems occurs with the same initiation temperature $T_0 = 340$ K. The qualitative diffraction pattern does not change after the passage of the second SHS front. However, reflections from Cd disappear completely (Fig. 2c), which implies that the reaction between Au and Cd films proceeds through the $(\gamma_2' + \zeta_2')$-martensite layer, which is a diffusion barrier for the reaction proceeding until the complete disappearance of the Cd layer. Indeed, subsequent Au layers deposited on reacted samples do not initiate the SHS wave. To determine the heat released as the SHS front passed, a chromel–copel thermocouple, where each layer was ~100 nm in thickness, was deposited on a glass substrate, and the (80-nm Au)/(200-nm Cd) film pair was then sputtered. However, the thermocouple did not detect any increase in the temperature of the (80-nm Au)/(200-nm Cd) sample as the SHS wave was passing. Therefore, (i) the SHS in the Au/$\gamma_2' + \zeta_2'$/Cd sample (Fig. 2c) proceeds in the solid phase, because the tem-

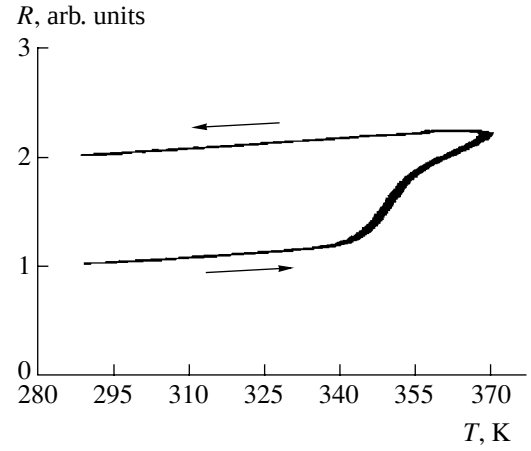

Fig. 1. Relative resistance R vs. substrate temperature T_S for the heating rate η = 5 K/s of the (80-nm Au/200-nm Cd) two-layer film sample. The arrows show the direct and reverse variation in resistance.

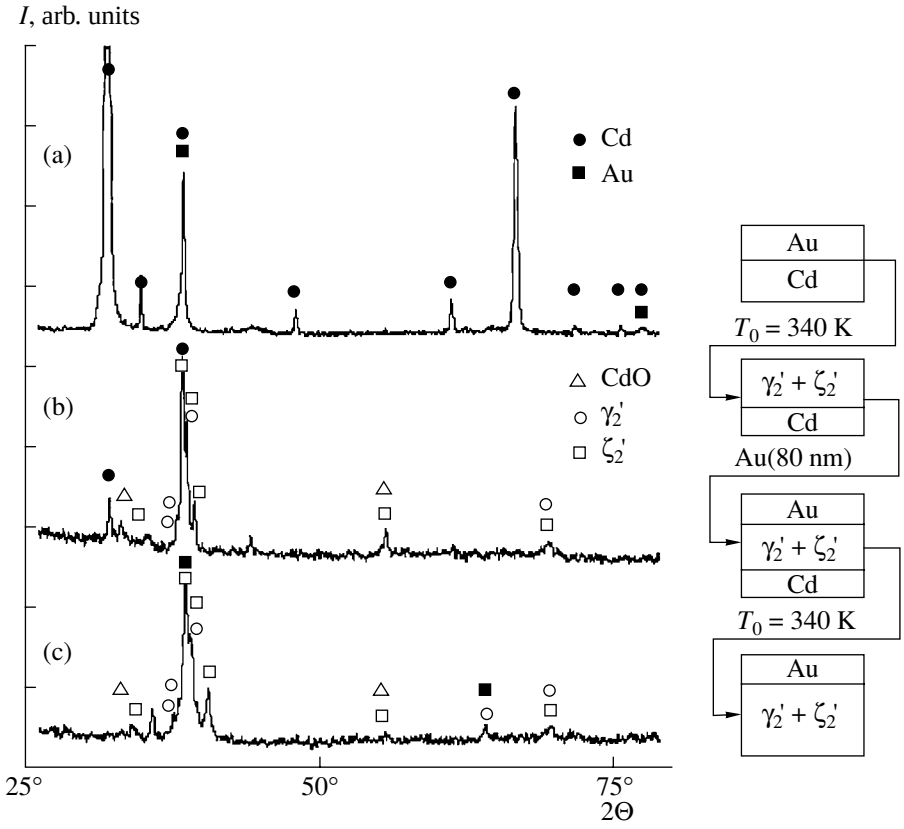

Fig. 2. Diffraction patterns of the (80-nm Au/200-nm Cd) two-layer film sample: (a) before the reaction, (b) after the passage of the SHS wave through the sample, and (c) after the secondary initiation of the SHS front in the reacted sample with the 80-nm Au layer deposited on it. The scheme in the right-hand part of the figure illustrates the corresponding changes in the phase content of the (80-nm Au/200-nm Cd) two-layer film sample.

perature of the γ_2'-martensite layer coincides with the initiation temperature T_0 = 340 K, and (ii) the solid-state synthesis in the film state between the Au and Cd layers is low-energy.

The velocity of the SHS front near the initiation temperature is $V_f \sim 10^{-2}$ m/s [4]. Assuming that the reaction begins at the interface of film reagents and propagates inside the sample bulk and along the sample surface with the same velocity, we estimate diffusivity as $D \sim dV_f = 2 \times 10^{-9}$ m^2/s, where d = 200 nm is the thickness of the reaction products, which is characteristic for the liquid phase. The typical diffusivity over grain edges in thin films is equal to $D_{gb} \sim 10^{-17}$ m^2/s [2]. The low temperature and the threshold character of atomic transport to depth 100–200 nm, together with extremely overestimated diffusivity D, indicate that diffusion along the edges of grains is not the basic mechanism of mass transfer accompanying the passage of the SHS wave in the Au/Cd sample.

Reaction between Ni and Al is one of the well-studied solid-state synthesis reactions. In particular, solid-state reactions in Al/Ni two-layer films and multilayers are actively studied (see [12, 13] and references therein). The initiation temperature of these reactions lies in the interval ~440–500 K [13], which coincides with the temperature interval of the formation of martensite in NiAl alloy [14]. Preliminary results indicate that the SHS in Mn/Fe two-layer films is initiated at ~500 K, which is close to the starting temperature of the martensitic transformation A_s = 470 K in 24MnFe alloy.

The above discussion indicates that the initiation temperature T_0 of the solid-state synthesis in two-layer film samples must coincide with the starting temperature of the reverse martensitic transformation A_s ($T_0 = A_s$) for a given binary system, if other structural transformations in the reaction product do not precede the martensitic transformation.

Since martensitic transformations can determine a solid-state reaction, the chemical and structural mechanisms must be identical. Therefore, a martensitic-like mechanism of atomic transport in the reaction can be as follows. As a result of chemisorption, the initial interface of the film reagents is a two-dimensional reaction product (martensite). When temperature increases up to the temperature of the reverse martensitic transformation, collective displacement transforms martensite to austenite. The reverse martensitic transformation is responsible for the approach of atoms of reagents and high stresses on both sides of the two-dimensional reac-

tion product. As a result, the activation energy for the initiation of the reaction decreases. The reaction is accompanied by the local diffusionless redistribution of atoms of reagents without transition to the liquid phase and with the formation of the martensite layer in the reaction products. Structural atomic rearrangement at the interface can occur through the formation of nanoclusters, whose ultrafast coherent rotation induces the directed ordered mixing of the reagents layers. Fast solid-phase diffusionless atomic rearrangement is responsible for the high effective diffusivity in the reaction. Reactions induced in thin films by martensitic transformations can be directed and cooperative with the formation of the orientational relations between the lattices of reagents and the martensitic phase.

It is well known that martensite is formed under mechanical stresses. Mechanical loads strongly affect the kinetics and temperature of martensitic transformations. Therefore, solid-state reactions determined by martensitic transformations can be initiated by pressure or impact. Indeed, the solid-state synthesis in Ni + Al powders is initiated by impact loads [15]. Thadhani [15] suggested the martensitic reaction mechanism but did not attribute it to martensitic transformations in NiAl alloy. The martensitic-like mechanism discussed above is expected to be able to ensure high rates of mass transfer in the shock-wave-induced synthesis. Therefore, the solid-state synthesis in Au + Cd powder systems must also be initiated by shock-wave compression.

In summary, we arrive at the following conclusions.

(i) The temperature of the martensitic transformation in binary alloys is the initiation temperature of the synthesis between alloy atoms if other structural transformations do not precede the martensitic transformation.

(ii) The solid-state synthesis in Au/Cd film samples proceeds in the SHS mode and is accompanied by the formation of martensitic phases in the reaction products.

(iii) Low-energy diffusionless processes are responsible for atomic transport up to 200 nm in Au/Cd-film samples during the reaction.

ACKNOWLEDGMENTS

This work was supported by the Krasnoyarsk Science Foundation (project no. 11F001C).

REFERENCES

1. H. Warlimont and L. Delaey, *Martensite Transformations in Copper-, Silver-, and Gold-Based Alloys* (Pergamon, Oxford, 1974; Nauka, Moscow, 1980).
2. *Thin Films. Interdiffusion and Reactions*, Ed. by J. Poate, K. Tu, and J. Mayer (Willey, New York, 1978; Mir, Moscow, 1982).
3. L. A. Clevenger, B. Arcort, W. Ziegler, *et al.*, J. Appl. Phys. **83** (1), 90 (1998).
4. V. G. Myagkov and L. E. Bykova, Dokl. Akad. Nauk **354** (6), 777 (1997).
5. V. G. Myagkov, L. E. Bykova, G. N. Bondarenko, *et al.*, Dokl. Akad. Nauk **371** (6), 763 (2000) [Dokl. Phys. **45**, 157 (2000)].
6. V. G. Myagkov, L. E. Bykova, G. N. Bondarenko, *et al.*, Pis'ma Zh. Éksp. Teor. Fiz. **71** (5), 268 (2000) [JETP Lett. **71**, 183 (2000)].
7. V. G. Myagkov, L. E. Bykova, L. A. Li, *et al.*, Dokl. Akad. Nauk **382** (4), 463 (2002) [Dokl. Phys. **47**, 95 (2002)].
8. R. W. Cahn, Nature (London) **374**, 120 (1995).
9. X. Ren and K. Otsuka, Nature (London) **379**, 579 (1997).
10. T. Suzuki and K. Fujimoto, Scr. Metall. **37** (10), 1525 (1997).
11. M. Kogachi, H. Ishibashi, T. Ohba, *et al.*, Scr. Metall. **42** (9), 841 (2000).
12. U. Rothhaar, H. Oechsner, M. Scheib, and R. Muller, Phys. Rev. B **61** (2), 974 (2000).
13. C. Michaelsen, K. Barmak, and G. Lucadanno, J. Appl. Phys. **80** (12), 6689 (1996).
14. P. L. Potapov, N. A. Poliakova, and V. A. Udovenko, Scr. Mater. **35** (3), 423 (1996).
15. N. N. Thadhani, J. Appl. Phys. **76** (4), 2129 (1994).

Translated by R. Tyapaev

Doklady Physics, Vol. 48, No. 1, 2003, pp. 34–37. Translated from Doklady Akademii Nauk, Vol. 388, No. 1, 2003, pp. 51–55.

TECHNICAL PHYSICS

Features of Thermoelastic Martensitic Transformations in [001] Titanium–Nickel Single Crystals

E. Yu. Panchenko[1,*], I. V. Kireeva[1], Yu. I. Chumlyakov[1], V. B. Aksenov[1], Corresponding Member of the RAS S. P. Efimenko[2], I. Karaman[3], and H. Sehitogly[4]

Received September 12, 2002

Deformation in titanium–nickel polycrystals at $T > M_s$ [M_s is the start temperature of the direct B2–B19' martensitic transformation (MT) upon cooling] leads to the formation of stress martensite, which is thermodynamically unstable at $T > A_f$ (A_f is the finish temperature of the reverse B19'–B2 MT upon heating). If the direct B2–B19' MT under loading is not accompanied by plastic deformation, the reverse B19'-B2 MT occurs when the load is removed, and, as a result, the phenomenon of superelasticity is observed [1]. The low yield stress of the high-temperature B2 phase favors the development of plastic deformation in the process of the MT under loading, and, consequently, the mobility of martensite–austenite interfaces decreases [1]. In the process of unloading, the reverse B19'–B2 MT occurs partially or is completely suppressed. In this case, stress martensite is stabilized by plastic deformation and superelasticity is absent. Thus, in order for superelasticity (SE) to appear, it is necessary, first, to apply a load at $T > A_f$ and to form thermodynamically unstable martensite and, second, to suppress the processes of plastic flow in the B2 phase in the MT under loading.

In twinned titanium–nickel single crystals and polycrystals near the stoichiometric composition, the necessary conditions of the appearance of superelasticity, which is not observed in the quenched state, are achieved by thermomechanical treatment—cold deformation up to strain $\varepsilon = 30\%$ and subsequent annealing at $T = 673$–773 K [1, 2]. In titanium–nickel alloys with nickel content $C_{Ni} > 50.6$ at. %, superelasticity is observed after both thermomechanical treatment and aging of previously quenched alloys at $T = 673$–823 K [1–3]. Consequently, the formation of a high density of crystal-structure defects—dislocations and twins in stoichiometric titanium–nickel alloys—and the precipitation of disperse particles along with dislocations in aging titanium–nickel alloys result in the hardening of the high-temperature B2 phase and the appearance of superelasticity [1–3].

In this study, using Ti–50.3 at. % Ni and Ti–51 at. % Ni single crystals oriented along the [–111], [001], and [–117] directions, we analyze the principle possibility of obtaining superelasticity in quenched titanium–nickel single crystals that are free from crystal-structure defects and disperse particles. The formulation of the problem is based on the following concepts. First, slip deformation in B2 intermetallides (including titanium–nickel) having high energies of the antiphase interface are realized by $a\langle 100\rangle\{110\}$ dislocations [4]. The Schmid factor for these slip systems in crystals oriented for tensile and compressive deformations along the [001] direction is equal to zero. Consequently, a high-strength state in titanium–nickel single crystals can be obtained by decreasing the Schmid factor for slip systems in the [001] orientation [4]. Second, deforming stresses in the B2 phase in titanium–nickel can be increased by deviating nickel content from the stoichiometric value, i.e., by taking $C_{Ni} > 50$ at. % [5]. If these factors actually suppress plastic flow processes of the B2 phase in the MT under loading, superelasticity is possible in quenched Ti–51 at. % Ni crystals with the tension–compression axis along the [001] direction. In quenched Ti–51 at. % Ni crystals with the deformation axis along the [–111] direction, where the Schmid factor is nonzero ($m_{[-111]} = 0.47$), as well as in Ti–50.3 at. % Ni single crystals, the low strength properties of the B2 phase will favor the development of plastic flow in the B2–B19' MT under loading, and superelasticity is impossible.

The experimental technique was presented in detail in [6]. The start (M_s) and finish (M_f) temperatures of the direct B2–B19' MT upon cooling and the respective temperatures A_s and A_f of the reverse B19'–B2 MT upon

[1] *Siberian Institute of Technical Physics, Tomsk State University, Novo-Sobornaya pl. 1, Tomsk, 634050 Russia*

[2] *Baĭkov Institute of Metallurgy, Russian Academy of Sciences, Leninskiĭ pr. 49, Moscow, 117334 Russia*

[3] *Texas A&M University, College Station, TX 77843-3123, USA*

[4] *University of Illinois at Urbana-Campaign, 1206 West Green St., Urbana, IL 61801-3080, USA*

* *e-mail: chum@phys.tsu.ru*

1028-3358/03/4801-0034$24.00

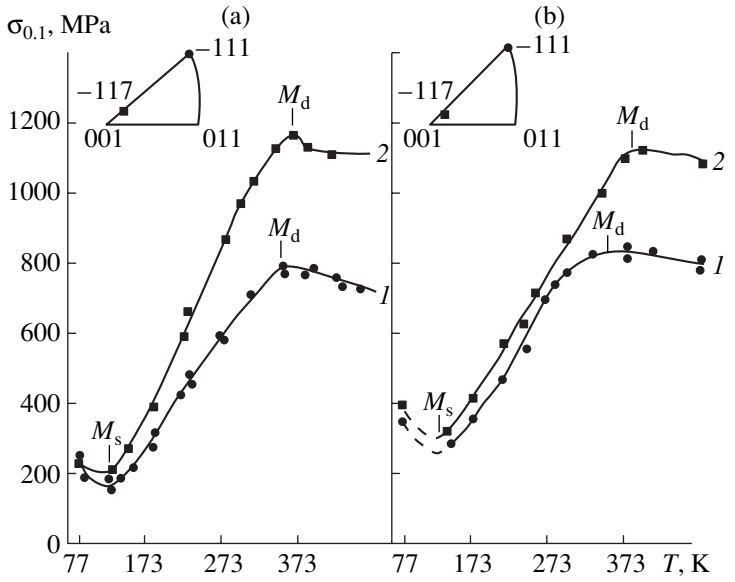

Fig. 1. Temperature dependence of the yield stress for quenched Ti–51 at. % Ni single crystals whose axis is directed along (*1*) [–111] and (*2*) [–117] directions as obtained under (a) tension and (b) compression.

heating were determined from the temperature dependence of electrical resistivity (Table 1).

Figure 1 shows the dependence of the yield stress $\sigma_{0.1}$ on testing temperature for quenched Ti–51 at. % Ni crystals under tension and compression. It is seen that, in the high-temperature B2 phase at $T > M_d$ (M_d is the temperature at which the critical stresses for the formation of stress martensite are equal to the stress of plastic deformation in the B2 phase), crystals with the tension–compression axis along the [–117] direction are "hard," because their $\sigma_{0.1}$ values are larger than those for "soft" crystals oriented along the [–111] direction. For the [001] and [–117] orientations (the [–117] orientation is deviated from the [001] pole by 12°), $\sigma_{0.1}$ in the high-temperature B2 phase is large (Fig. 1, Table 2), because the Schmid factor for $a\langle 100\rangle\{110\}$ systems is close to zero ($m_{[-117]} = 0.19$ and $m_{[001]} = 0$), and slip deformation is therefore hindered. The minimum of $\sigma_{0.1}(T)$ coincides with the start temperature M_s of the MT upon cooling (Table 1). In the temperature range $M_s < T < M_d$ of the development of the MT under loading, $\sigma_{0.1}$ increases with a rise in temperature (Fig. 1) and the slope $\alpha = \dfrac{d\sigma_{0.1}}{dT}$ depends on the orientation of the crystal and the type of deformation (tension or compression, see Table 2). In this temperature range, $\sigma_{0.1}(T)$ is described by the Clapeyron–Clausius relationship [1]

$$\frac{d\sigma}{dT} = -\frac{\Delta H}{\varepsilon_0 T_0}, \qquad (1)$$

where T_0 is the phase equilibrium temperature, ΔH is the enthalpy of the transformation, and the lattice strain ε_0 in the process of the MT can be experimentally obtained from the shape memory effect (Table 1). This effect in the quenched crystals depends on their orientation and the type of deformation (tension or compression) and is close to values calculated in the model that takes into account only lattice deformation (Table 2). This means that, being heated higher than A_f, a completely untwinned B19'-martensite single crystal, which is obtained under deformation at $T < M_s$, is transformed to a B2-phase single crystal. The dependence of the slope $\alpha = \dfrac{d\sigma_{0.1}}{dT}$ on the orientation of crystals and the type of deformation (tension or compression) in the

Table 1. Temperatures of the B2–B19' thermoelastic martensitic transformations in titanium–nickel single crystals

Chemical composition	Thermal treatment	M_s, K	M_f, K	A_s, K	A_f, K
Ti–50.3 at. % Ni	0.5-h annealing at 1203 K, water quenching	265	243	270	293
Ti–51 at. % Ni	0.5-h annealing at 1203 K, water quenching	150	123	168	190
	0.5-h annealing at 1203 K, water quenching and 1-h aging at 673 K	≤77 K	–	–	–

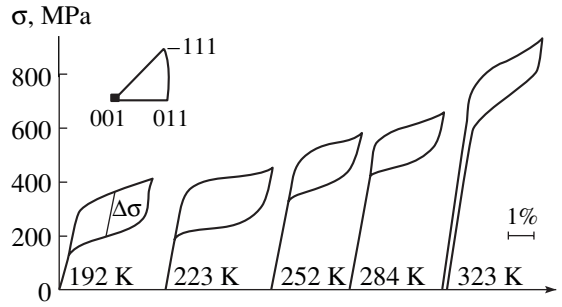

Fig. 2. Superelasticity curves for Ti–51 at. % Ni single crystals in the quenched state under compression along the [001] direction.

temperature range of the MT under loading (Table 2) can be explained by Eq. (1). The values of the shape memory effect for [–117] and [001] Ti–51 at. % Ni and Ti–50.3 at. % Ni monophase single crystals under tensile deformation are less than those for [–111] crystals, i.e., $\varepsilon_{0[-117],\,[001]} < \varepsilon_{0[-111]}$, and therefore $\alpha_{[001],\,[-117]} > \alpha_{[-111]}$ in the [–117] and [001] orientations according to Eq. (1) (Table 2). Under compression (Fig. 1b), as well as under tension, deforming stresses in the high-temperature B2 phase ($T > M_d$) depend strongly on orientation. However, slope α is independent of orientation in the temperature range $M_s < T < M_d$ of the MT under loading. Therefore, ε_0 is independent of orientation according to Eq. (1). This conclusion is corroborated by the closeness of ε_0 values both measured and calculated with inclusion of only lattice deformation for these orientations under compression (Table 2).

It is impossible to investigate superelasticity effects in TI–51 at. % Ni single crystals whose tensile axis is oriented along the [–117] and [001] directions, because these crystals undergo brittle fracture near the yield stress. In other orientations ([–111], [–112], and [122]), superelasticity is not observed in quenched single crystals under tension.

In Ti–51 at. % Ni monophase single crystals oriented near the [001] direction, we observed superelasticity under compression for the first time (Fig. 2). Superelasticity in [–117] and [001] quenched single crystals is observed in the temperature ranges 60 and 130 K, respectively. The strength properties of the B2 phase in [001] single crystals are higher than those for [–117] crystals by 200 MPa (Table 2). Consequently, the temperature range, where superelasticity in the quenched titanium–nickel single crystals is observed, is determined by deforming stresses in the high-temperature B2 phase. Superelasticity is not observed in the quenched [001] and [–111] Ti–50.3 at. % Ni crystals under tension, primarily because the strength properties of the B2 phase in them are considerably lower than those in Ti–51 at. % Ni crystals (Table 2). The measured values of the shape memory effect and superelasticity in quenched Ti–51 at. % Ni [001] single crystals Ti–50.3 at. % Ni under compression coincide with the calculated values of lattice strain ε_0 under the B2–B19' MT in this orientation (Table 2). Consequently, in [001] Ti–51 at. % Ni quenched crystals, deformation accompanying measurements of both the shape memory effect ($T < M_s$) and superelasticity ($T > A_f$) results in the same final product, a defect-free B19'-martensite crys-

Table 2. Strength and functional properties for titanium–nickel single crystals for various Ni contents and orientations of the tension–compression axis

Chemical composition	Thermal treatment	Deformation	Orientation	$\sigma_{0.1}$ (473 K), MPa	$\frac{d\sigma}{dT}$, MPa/K	Shape memory effect, ε_0, %		ΔT_{SE}, K	ε_{SE}, % at $T = A_f + 10$ K
						theor. [1, 7]	exp.		
Ti–50.3 at. % Ni	0.5-h annealing at 1203 K, water quenching	Tension	[–111]	530	1.6	9.8	9.6	No SE	
			[001]	580	5.3	2.7	2.7		
Ti–51 at. % Ni	0.5-h annealing at 1203 K, water quenching	Tension	[–111]	700	2.1	9.8	8.8	No SE	
			[–117]	1100	4.3	5.0	4.5	Failure at $\varepsilon < 1\%$	
		Compression	[–111]	800	3.6	3.6	3.4	No SE	
			[–117]	1100	3.0	5.3	4.8	60	4.3
			[001]	1300	3.25	4.2	4.15	130	4.2
	0.5-h annealing at 1203 K, water quenching and 1-h aging at 673 K	Tension	[–111]	1000	*2.5*	9.8	5.4	150	4.2
		Compression	[001]	1400	3.0	4.2	4.1	150	4.0

tal, which is transformed to the B2-phase single crystal at $T > A_f$, when load is removed.

The precipitation of disperse Ti_3Ni_4 particles (30 nm in size) in [001] crystals after 1-h aging at 673 K increases the strength properties of the B2 phase and extends the temperature range where superelasticity is observed by 30 K compared to the monophase crystals (Table 2). The values of the shape memory effect and superelasticity in aging [001] crystals are equal to each other and are virtually identical to those obtained for monophase crystals (Table 2).

The aging of [–111] crystals decreases the value of the shape memory effect for tension–compression deformation compared to monophase crystals (Table 2) and leads to the appearance of the superelasticity effects [3], which are absent in the quenched state of these crystals. The $\Delta\sigma$ value, which is determined from the height of a mechanical hysteresis loop for strain equal to half the superelasticity value (Fig. 2), decreases with increasing testing temperature in [–111] aging crystals and depends only slightly on testing temperature in [001] quenched and aging crystals (Fig. 3). The difference in the temperature dependences of $\Delta\sigma$ in [–111] and [001] aging crystals is attributed to the features of the fine structure of B19' martensite crystals. Electron-microscope investigations showed that the $\langle 110\rangle\{0.7201\ 1\ -1\}$ type-II twinning and compound twinning prevail in monophase single crystals and single crystals containing disperse $\langle 001\rangle\{100\}$ particles, respectively [8]. Disperse particles hinder detwinning in [–111] aging crystals, whereas type-II twins in the monophase crystals have high mobility. Therefore, the shape memory effect in [–111] aging crystals is less than that in the same quenched crystals (Table 2). In [001] aging crystals, compound twins do not contribute to the measured values of the shape memory effect and superelasticity, because the Schmid factor for $\langle 001\rangle\{100\}$ compound twins in these crystals is equal to zero. Therefore, the experimental values of the shape memory effect and superelasticity in quenched and aging [001] crystals coincide with the calculated value of the lattice strain $\varepsilon_{0,\,theor}$ (Table 2). Thus, the final product after deformation at both $T < M_s$ and $T > A_f$ in aging [001] and [–111] crystals is the same B19' martensite with a high density of geometrically necessary $\langle 001\rangle\{100\}$ twins.

Finally, the field of external stresses in [–111] aging crystals can interact with compound twins, because the Schmid factor for multiple twinning in this orientation is nonzero. This interaction is absent in [001] aging crystals, because the Schmid factor for multiple twinning equals zero. Therefore, the mechanical-hysteresis value $\Delta\sigma$ in [001] aging crystals is independent of testing temperature and, accordingly, of applied loads, whereas the fine structure of the B19' martensite in [–111] crystals can depend on deforming stresses and can be responsible for the temperature dependence of mechanical hysteresis $\Delta\sigma$ (Fig. 3, curve *3*).

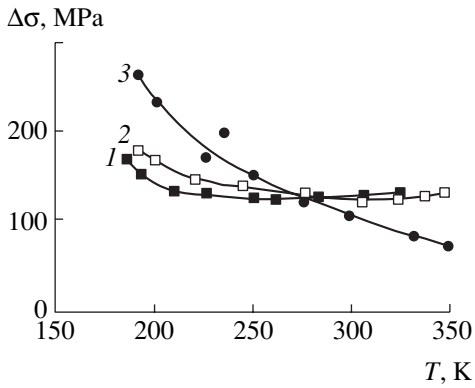

Fig. 3. Temperature dependence of mechanical hysteresis $\Delta\sigma$ for Ti–51 at. % Ni single crystals with (*1*) [001] orientation under compression after 0.5-h quenching from 1203 K, (*2*) [001] orientation under compression after 0.5-h quenching from 1203 K and 1-h annealing at 673 K, and (*3*) [–111] orientation under tension after 0.5-h quenching from 1203 K and 1-h annealing at 673 K.

Thus, quenched Ti–51 at. % Ni single crystals, where defects of the crystal structure and disperse particles are absent, exhibit superelasticity when the compression axis is close to the [001] direction. It is shown that superelasticity and the temperature range where it is observed in titanium–nickel single crystals are controlled by deforming stresses of the high-temperature B2 phase.

ACKNOWLEDGMENTS

This work was supported by the Russian Foundation for Basic Research (project no. 02-02-16019) and the Ministry of Education of the Russian Federation (project no. E00-3.04.29).

REFERENCES

1. K. Otsuka and C. M. Wayman, *Shape Memory Materials* (Cambridge Univ. Press, Cambridge, 1998).
2. E. Hornbogen, V. Mertinger, and D. Wurzel, Scr. Mater. **44**, 171 (2001).
3. Yu. I. Chumlyakov, S. P. Efimenko, I. V. Kireeva, *et al.*, Dokl. Akad. Nauk **381** (5), 610 (2001) [Dokl. Phys. **46**, 849 (2001)].
4. N. S. Surikova and Yu. I. Chumlyakov, Fiz. Met. Metalloved. **89** (2), 98 (2000).
5. V. G. Pushin, V. V. Kondrat'ev, and V. N. Khachin, *Pretransition Phenomena and Martensitic Transformations* (Ural. Otd. Ross. Akad. Nauk, Yekaterinburg, 1998).
6. K. Gall, H. Sehitogly, I. Karaman, *et al.*, Acta Mater. **48**, 3311 (2000).
7. S. Miyaski, S. Kimura, K. Otsuka, and Y. Suzuki, Scr. Metall. **18**, 883 (1984).
8. M. Nishida, C. M. Wayman, and A. Chiba, Metallography **21** (3), 275 (1988).

Translated by Yu. Vishnyakov

Doklady Physics, Vol. 48, No. 1, 2003, pp. 38–41. Translated from Doklady Akademii Nauk, Vol. 388, No. 2, 2003, pp. 189–192.

MECHANICS

Conditions of Stability in the Sense of Joukowski for the Orbits of Equations of Celestial Mechanics

O. V. Druzhinina

Presented by Academician V.V. Rumyantsev June 28, 2002

Received August 27, 2002

In this study, the conditions of stability in the sense of Joukowski for orbits of the equations of celestial mechanics were found. The problem of stability of orbits was first considered in [1]. The related notion of stability in the sense of Jacobi was introduced and investigated in [2].

Here, we introduce the following definitions.

Definition 1. Let C_0^+ be the semiorbit of the solution $\varphi(t) = (x^0(t), y^0(t))$ to the equations of motion

$$\ddot{x} = f_1(t, x, y, \dot{x}, \dot{y}), \quad \ddot{y} = f_2(t, x, y, \dot{x}, \dot{y}) \tag{1}$$

with the energy integral

$$\dot{x}^2 + \dot{y}^2 = g(x, y, h), \tag{2}$$

where the functions f_1, f_2, and g are such that the solution exists and is unique. A segment of the semiorbit C_0^+ is called *stable in the sense of Joukowski* if the continuation of the perturbed-motion trajectory

$$x = x^0(t) + \delta x(t), \quad y = y^0(t) + \delta y(t) \tag{3}$$

always approaches the segment to a distance less than the first order of smallness when the difference between the initial data of the semiorbit C^+ and the corresponding point of the segment of the semiorbit C_0^+ has smallness higher than the first order.

The point that lies in the segment of the semiorbit C_0^+ and is conjugate with the point (x_0, y_0) in this sense is named the kinetic focus of this point [3]. For isoenergetic variations, these are kinetic focuses in the sense of Maupertuis. Definition 1 is equivalent to the following proposition: a segment that belongs to the semiorbit C_0^+ of Eqs. (1) and is adjacent to the point (x_0, y_0) is stable in the sense of Joukowski if its points have kinetic focuses in the sense of Maupertuis.

Russian Open State Technical University of Railway Transport, ul. Chasovaya 22/2, Moscow, 125993 Russia

Definition 2. The semiorbit C_0^+ of Eqs. (1) is called *stable in the sense of Joukowski* if each of its segments is stable in the sense of Joukowski.

Definition 2 renders concrete the definition of semiorbit stability proposed in [4].

Let the Lagrange function have the form

$$L = T(\dot{x}, \dot{y}) - \Pi(x, y), \tag{4}$$

where $T(\dot{x}, \dot{y}) = \frac{1}{2}(\dot{x}^2 + \dot{y}^2)$ is the kinetic energy and $\Pi(x, y)$ is the potential. Since this Lagrange function (4) explicitly lacks time t, the corresponding mechanical system has the energy integral [3]

$$\sum_{i=1}^{2} \dot{x}_i \frac{\partial L}{\partial \dot{x}_i} - L = h, \tag{5}$$

where h is a constant.

Let points c_0 and c at time t lie in the semiorbits C_0^+ and C^+, respectively, and cd be the linear segment orthogonal to the semiorbit C_0^+. The lengths of arc c_0d and segment cd are δs and $\delta n = z$, respectively.

Let α and β be the lengths of the arcs of the semiorbit C_0^+ from a certain fixed point O to the points c_0 and d, respectively. It is evident that

$$\delta s = \alpha - \beta. \tag{6}$$

We take the quantities α and δn as Lagrange's generalized coordinates. This is always possible, because the positions of the points of the semiorbit C^+ adjacent to the semiorbit C_0^+ are uniquely defined in terms of α and δn.

Theorem 1. *Semiorbit C_0^+ is stable in the sense of Joukowski if the inequality*

$$\Pi_{zz}^0 + 3\dot{\beta}^2 R_{c_0}^{-2} > 0 \quad \forall c_0 \in C_0^+ \tag{7}$$

1028-3358/03/4801-0038$24.00

is valid. Here, β is the length of the arc of the semiorbit C_0^+ from a fixed point to the point c_0 and R_{c_0} is the radius of curvature of the semiorbit at the point c_0.

The principal ideas of the proof are as follows. We consider the semiorbit C^+ that is adjacent to the given semiorbit C_0^+ and has the same energy. Let Lagrange function (4) in the coordinates $(\alpha, \delta n)$ have the form

$$L = \frac{1}{2}(\dot{\delta n})^2 + \frac{1}{2}(1 + R^{-1}\delta n)^2\dot{\alpha}^2 - \Pi(\delta n, \alpha), \quad (8)$$

where R is the radius of curvature of the semiorbit C^+ at the point c_0.

Lagrange's equations of motion corresponding to Eq. (8) have the form

$$\ddot{\delta n} - (1 + R^{-1}\delta n)R^{-1}\dot{\alpha}^2 = -\Pi_{\delta n}, \quad (9)$$

$$\frac{d}{dt}[(1 + R^{-1}\delta n)^2\dot{\alpha}]$$

$$+ (1 + R^{-1}\delta n)R^{-2}\dot{\alpha}^2\frac{dR}{d\alpha}\delta n = -\Pi_\alpha. \quad (10)$$

These equations have the energy integral

$$\frac{1}{2}(\dot{\delta n})^2 + \frac{1}{2}(1 + R^{-1}\delta n)^2\dot{\alpha}^2 + \Pi = h. \quad (11)$$

Equations (9) and (10) linearized with respect to $(\alpha, \delta n)$ have the form

$$\ddot{\delta n} + R_{c_0}^{-2}\dot{\beta}^2\delta n - (\dot{\beta}^2 + 2\dot{\beta}\dot{\delta s})\left[R_{c_0} + \delta s\left(\frac{dR}{d\beta}\right)_{c_0}\right]^{-1}$$

$$= -[\Pi^0_{\delta n} + \delta s\Pi^0_{\delta\beta} + \Pi^0_{\delta n\delta n}\delta n], \quad (12)$$

$$\frac{1}{2}(1 + 2R_{c_0}^{-1}\delta n)(\dot{\beta}^2 + 2\dot{\beta}\dot{\delta s})$$

$$+ \Pi_{c_0} + \delta s\Pi^0_\beta + \delta n\Pi^0_{\delta n} = h. \quad (13)$$

Here, the superscript 0 denotes that the derivatives are calculated at the point $c_0 \in C_0^+$. It is easy to find that

$$R_{c_0}^{-1}\dot{\beta}^2 = \Pi^0_{\delta n}, \quad \ddot{\beta} = -\Pi_\beta, \quad (14)$$

$$\frac{1}{2}\dot{\beta}^2 + \Pi_{c_0} = h, \quad (15)$$

because β and $\dot{\beta}$ correspond to the known solution.

Substituting Eqs. (12) and (13) into Eqs. (10) and (11), we arrive at the respective equations

$$\dot{\beta}\dot{\delta s} - s\ddot{\beta} + 2R_{c_0}^{-1}\dot{\beta}^2\delta n = 0, \quad (16)$$

$$\ddot{\delta n} - R_{c_0}^{-2}\dot{\beta}^2\delta n + s\left[R_{c_0}^{-2}\dot{\beta}^2\left(\frac{dR}{d\beta}\right)^0 + \Pi^0_{\delta n}\right]$$

$$- 2R_{c_0}^{-1}\dot{\beta}\dot{\delta s} = -\delta n\Pi^0_{\delta n\delta n}. \quad (17)$$

From (12), it follows that

$$\Pi^0_{\delta n} = -R_{c_0}^{-2}\dot{\beta}^2\left(\frac{dR}{d\beta}\right)^0 + 2R_{c_0}^{-1}\dot{\beta}\frac{d}{d\beta}\left(\frac{d\beta}{dt}\right)$$

$$= -2R_{c_0}^{-1}\dot{\beta}^2\left(\frac{dR}{d\beta}\right)^0 + 2R_{c_0}^{-1}\beta. \quad (18)$$

Consequently, Eq. (18) reduces to the form

$$\ddot{\delta n} - R_{c_0}^{-2}\dot{\beta}^2\delta n - R_{c_0}^{-1}(\dot{\beta}\dot{\delta s} - s\ddot{\beta}) = -\delta n\Pi^0_{\delta n\delta n}. \quad (19)$$

Eliminating the difference $\dot{\beta}\,\dot{\delta s} - s\ddot{\beta}$ from Eqs. (16) and (19), we obtain the variational equation

$$\ddot{\delta n} + (\Pi^0_{\delta n\delta n} + 3R_{c_0}^{-2}\dot{\beta}^2)\delta n = 0. \quad (20)$$

Let us write Eq. (20) in the form

$$\ddot{\delta n} + \Theta\delta n = 0, \quad (21)$$

where the function Θ is defined by the formula

$$\Theta = \Pi^0_{\delta n\delta n} + 3R_{c_0}^{-2}\dot{\beta}^2. \quad (22)$$

We consider only variations δs and δn such that the roundabout (perturbed) motion $s = s^0(t) + \delta s(t)$, $n = n^0(t) + \delta n(t)$ belongs to the same isoenergetic family (h) as the reference motion $s = s^0(t)$, $n = n^0(t)$. In this case, the variational equations admit the energy integral, which is linear with respect to the variations δs, δn and their rates $\dot{\delta s}$ and $\dot{\delta n}$. This energy integral can be formally obtained from energy integral (5) by varying and retaining only the terms of the first order of smallness.

Stepanov [2] showed that, in the isoenergetic case, Θ can be represented as a function of the constant h, coordinates of the point c_0 at the reference semiorbit, and the angle φ_0 between the velocity in the reference semiorbit and the abscissa axis.

If the function $\Theta(x, y, \varphi)$ along the semiorbit C_0^+ is positive, every perturbed semiorbit C^+ approaches C_0^+.

At the last stage of proving Theorem 1, the following fact from the Sturm–Liouville theory [5] is used.

Lemma. *Let the function Θ in Eq. (21) be defined in the interval (t_1, t_2) and vary between $p_1^2 > 0$ and $p_2^2 > 0$. In this case, any function that is a solution z to Eq. (21) and is equal to zero at $t_3 \in (t_1, t_2)$ has another zero $t_4 \in (t_1, t_3)$, where $t_1 - t_3$ lies between $\frac{\pi}{p_1}$ and $\frac{\pi}{p_2}$ provided that the last interval is sufficiently small compared to (t_1, t_2).*

Using the lemma, we obtain the proposition of Theorem 1.

Now, let C_0^+ be a periodic orbit C_0 with perimeter l. We take α as an independent variable and designate $\dot{\alpha}$ as γ. Then, it follows from Eq. (20) that

$$\frac{d^2\delta n}{d\alpha^2} + \gamma^{-1}\frac{d\gamma}{d\alpha}\frac{d\delta n}{d\alpha} + (\gamma^{-2}\Pi_{zz}^0 + 3R_{c_0}^{-2})\delta n = 0. \quad (23)$$

Let k be an arbitrary integer. If $z = \varphi_0(\alpha)$ is the solution to Eq. (23), the functions

$$z_k = \phi_0(\alpha + kl), \quad k = 1, 2, \ldots \quad (24)$$

also are the solutions to Eq. (23). Let us consider three solutions z_k, z_{k+1}, and z_{k+2} for a fixed k. Since Eq. (21) is linear, the solutions must be related as

$$z_{k+2} = c_1 z_{k+1} + c_2 z_k, \quad (25)$$

where the constants c_1 and c_2 are independent of α and k.

Let us show that c_1 and c_2 depend only on the unperturbed orbit C_0. Indeed, let

$$\tilde{z}_k = \psi(\alpha + kl), \quad k = 1, 2, \ldots \quad (26)$$

represent the set of solutions generated by another solution $z = \varphi(\alpha)$ to Eq. (23). Since these solutions must be related as

$$\tilde{z}_k = c_3 z_{k+1} + c_4 z_k, \quad (27)$$

where c_3 and c_4 are constants, $\tilde{z}_k$ satisfies Eq. (25) with the same c_1 and c_2. From the equations

$$\frac{d^2 z_k}{d\alpha^2} + \gamma^{-1}\frac{d\gamma}{d\alpha}\frac{dz_k}{d\alpha} + (\gamma^{-2}\Pi_{zz}^0 + 3R_{c_0}^{-2})z_k = 0, \quad (28)$$

$$\frac{d^2 z_{k+1}}{d\alpha^2} + \gamma^{-1}\frac{d\gamma}{d\alpha}\frac{dz_{k+1}}{d\alpha} + (\gamma^{-2}\Pi_{zz}^0 + 3R_{c_0}^{-2})z_{k+1} = 0, \quad (29)$$

it is easy to derive the equality

$$\frac{d}{d\alpha}\left(z_{k+1}\frac{dz_k}{d\alpha} - z_k\frac{dz_{k+1}}{d\alpha}\right) = -\gamma^{-1}\frac{d\gamma}{d\alpha}\left(z_{k+1}\frac{dz_k}{d\alpha} - z_k\frac{dz_{k+1}}{d\alpha}\right),$$

from which it follows that

$$z_{k+1}\frac{dz_k}{d\alpha} - z_k\frac{dz_{k+1}}{d\alpha} = c_5\gamma^{-1}, \quad (30)$$

where c_5 is a constant. Replacing the subscript k with $k + 1$ in Eq. (30), we obtain

$$z_{k+2}\frac{dz_{k+1}}{d\alpha} - z_{k+1}\frac{dz_{k+2}}{d\alpha} = c_5\gamma^{-1}. \quad (31)$$

From Eqs. (25), (30), and (31), we have the relation

$$z_{k+1}\frac{dz_k}{d\alpha} - z_k\frac{dz_{k+1}}{d\alpha} = (c_1 z_{k+1} + c_2 z_k)\frac{dz_{k+1}}{d\alpha} - z_{k+1}\frac{d}{d\alpha}(c_1 z_{k+1} + c_2 z_k) = -c_2\left(z_{k+1}\frac{dz_k}{d\alpha} + z_k\frac{dz_{k+1}}{d\alpha}\right), \quad (32)$$

according to which $c_2 = -1$. Consequently, the function z_k that is generated by an arbitrary solution to Eq. (23) is also the solution to the difference equation

$$z_{k+2} - Mz_{k+1} + z_k = 0, \quad (33)$$

where the constant M depends only on the reference orbit C_0. The general solution to Eq. (33) has the form

$$z_k = f_1\lambda_1^k + f_2\lambda_2^k, \quad (34)$$

where f_i, $i = 1, 2$ are arbitrary functions of the period α chosen such that z satisfies Eq. (23) and the numbers λ_i, $i = 1, 2$ are the roots of the quadratic equation

$$\lambda^2 - M\lambda + 1 = 0. \quad (35)$$

Relationship (29) means that the equality

$$\frac{z_k + z_{k+2}}{z_{k+1}} = M$$

is valid for all the orbits C roundabout with respect to the reference orbit C_0.

The roots of Eq. (35) are real for $|M| \geq 2$ and complex for $|M| < 2$. Therefore, the reference periodic orbit C_0 is stable and unstable in the sense of Joukowski if $|M| < 2$ and $|M| \geq 2$, respectively. This statement can be formulated as the following theorem.

Theorem 2. *A periodic orbit C_0 is stable in the sense of Joukowski if and only if $|M| < 2$ in Eq.* (35).

Example. We consider the equations

$$\ddot{x} = \Pi_x, \quad \ddot{y} = \Pi_y. \quad (36)$$

Here, $\Pi = -\frac{1}{r}$, where $r^2 = x^2 + y^2$. For negative energy integral $h < 0$, all the orbits of Eqs. (36) are ellipses. Let the trajectory C be the ellipse

$$r = \frac{p_0}{1 - e_0\cos\varphi}.$$

It is evident that the quantities e_0, p_0, and h_0 are related as

$$2h_0 = \frac{1 - e_0^2}{p_0}.$$

We consider the family of ellipses $p = r(1 - e_0\cos\varphi)$.

The condition of contact with the orbits is

$$\dot{p} = \dot{r}(1 - e_0\cos\varphi) + re_0\dot{\varphi}\sin\varphi = 0. \quad (37)$$

The second derivative is given by the expression

$$\ddot{p} = \ddot{r}(1 - e_0\cos\varphi) + 2e_0\dot{r}\dot{\varphi}\sin\varphi + e_0r\dot{\varphi}^2\cos\varphi + e_0r\ddot{\varphi}\sin\varphi, \quad (38)$$

which can be represented as

$$\ddot{p} = \frac{(1 - e_0^2)(1 - e_0\cos\varphi)^2}{r(1 - 2e_0\cos\varphi + e_0^2)} - (p^{-1} - p_0^{-1}). \quad (39)$$

Assuming that $p_0 > 0$, one can always choose numbers p_- and p_+ such that $0 < p_- < p_0 < p_+$. This ring contains the orbit C. From Eq. (39), it follows that

$$\ddot{p} > 0 \quad \text{if} \quad p_- \le p < p_0;$$
$$\ddot{p} < 0 \quad \text{if} \quad p_0 < p \le p_+.$$

All the Kepler ellipses with nonzero $p_0 \neq 0$ are stable in the sense of Joukowski, because the function Θ in Eq. (21) is positive. Stepanov [2] showed that, if $\frac{p}{1+e} \ge -\frac{1}{4h}$, ellipses are stable in the sense of Jacobi. This example illustrates that the notion of stability in the sense of Jacobi introduced in [2] differs from the notion of stability in the sense of Joukowski.

ACKNOWLEDGMENTS

I am grateful to Academician V.V. Rumyantsev and Prof. A.A. Shestakov for attention to this study. This work was supported by the Ministry of Education of the Russian Federation (project no. 020702-2-075).

REFERENCES

1. N. E. Zhukovskiĭ, Uch. Zap. Mosk. Univ., Otd. Fiz.-Mat., No. 4, 1 (1882).
2. V. V. Stepanov, Astron. Zh. **13** (5), 435 (1936).
3. A. I. Lur'e, *Analytical Mechanics* (GIFML, Moscow, 1961).
4. O. V. Druzhinina, Dokl. Akad. Nauk **355** (3), 339 (1997) [Phys. Dokl. **42**, 392 (1997)].
5. E. A. Coddington and N. Levinson, *Theory of Ordinary Differential Equations* (McGraw-Hill, New York, 1955; Inostrannaya Literatura, Moscow, 1958).

Translated by V. Bukhanov

Doklady Physics, Vol. 48, No. 1, 2003, pp. 42–45. Translated from Doklady Akademii Nauk, Vol. 388, No. 2, 2003, pp. 193–196.

MECHANICS

Some Properties of the Set of Homogeneous Solutions of Elasticity Theory

Corresponding Member of the RAS G. G. Sebryakov, M. D. Kovalenko*, and N. N. Tsybin

Received May 30, 2002

We study the basic properties of the characteristic set of homogeneous solutions of elasticity theory. It is known that homogeneous solutions of elasticity theory do not form a basis in the classical sense, i.e., on a segment. In particular, there are no sets of functions biorthogonal to homogeneous solutions in the classical sense. Here, we show that a set of functions biorthogonal to homogeneous solutions can be uniquely constructed by generalizing classical concepts of a function basis. The biorthogonal relation constructed for homogeneous solutions is of fundamental importance for solving boundary-value problems of elasticity theory in a rectangle [1].

Let us consider the following set of homogeneous solutions defined in the segment $|y| \le 1$:

$$\sigma(\lambda_k, y) = (\sin\lambda_k - \lambda_k\cos\lambda_k)\cos\lambda_k y - \lambda_k y\sin\lambda_k\sin\lambda_k y, \quad (1)$$

where numbers λ_k form the set $\{\pm\lambda_k, \pm\bar{\lambda}_k\}_{k=1}^{\infty} = \Lambda$ of all complex zeros of the entire function of exponential type two

$$L(\lambda) = \lambda + \sin\lambda\cos\lambda.$$

The set of functions (1) arises in particular when the first basic problem of elasticity theory is solved in the semi-strip $\{|y| \le 1, x \ge 0\}$ with free longitudinal sides [1].

Let us represent an even function $f(y)$ that is specified in the segment $|y| \le 1$ and is self-balanced (i.e., its integral over this segment is equal to zero) in the form of the series

$$f(y) = \sum_{k=1}^{\infty} A_k\sigma(\lambda_k, y) + \bar{A}_k\sigma(\bar{\lambda}_k, y), \quad |y| < 1 \quad (2)$$

in the set of homogeneous solutions (1) with coefficients A_k. Since the function is even, the sum in Eq. (2) can be calculated only over λ_k satisfying the condition $\mathrm{Re}\,\lambda_k > 0$.

The function

$$\sigma(\lambda, y) = (\sin\lambda - \lambda\cos\lambda)\cos\lambda y - \lambda y\sin\lambda\sin\lambda y \quad (3)$$

generates the set of homogeneous solutions (1). Function (3) is the even part of the more general function

$$\sigma_e(\lambda, y) = (\sin\lambda - \lambda\cos\lambda)e^{i\lambda y} + i\lambda y\sin\lambda e^{i\lambda y}, \quad (4)$$

which can be represented as the following differential operation for function $e^{i\lambda y}$:

$$\sigma_e(\lambda, y) = D(\lambda)\{e^{i\lambda y}\},$$
$$D(\lambda) = \lambda\sin\lambda\frac{d}{d\lambda} + (\sin\lambda - \lambda\cos\lambda). \quad (5)$$

To construct a set of functions biorthogonal to homogeneous solutions (1), we use general classical methods [2, Appendix III; 3, ch. IV]. Let a certain (λ_ν-dependent) set of even functions $s_\nu(y)$ ($\nu \ge 1$) be defined in the real axis y so that

$$\int_{-\infty}^{\infty}\sigma_e(\lambda, y)s_\nu(y)dy = \frac{L(\lambda)}{(\lambda^2 - \lambda_\nu^2)r_\nu} = R_\nu(\lambda), \quad (6)$$
$$\lambda \in \mathbb{R}, \quad \lambda_\nu \in \Lambda, \quad r_\nu = \lambda_\nu^2 - \bar{\lambda}_\nu^2, \quad \nu \ge 1.$$

If the set of functions $\{s_\nu(y)\}_{\nu=1}^{\infty}$ (square-integrable in the support in $|y| < 1$) satisfying Eq. (6) existed, it would be the desired biorthogonal set, because function $R_\nu(\lambda_k)$ is equal to $M_k = \dfrac{\cos^2\lambda_k}{\lambda_k r_k}$ and zero when $\lambda_\nu = \lambda_k$ and $\lambda_\nu \ne \lambda_k$, respectively. In this case, λ_ν and $\bar{\lambda}_\nu$ are different, because $R_\nu(\bar{\lambda}_\nu) = \bar{R}_\nu(\lambda_\nu) = 0$ for all $k, \nu \ge 1$. However, this set of functions cannot exist, because the set of homogeneous solutions is not minimal in the segment $|y| \le 1$. Nevertheless, a certain generalization of the classical concept of biorthogonality in a segment enables us to construct the biorthogonal relation. In this case, the biorthogonal set of functions is uniquely determined in the class of functions for which the Borel

State Research Institute of Aviation Systems (GosNIIAS), ul. Viktorenko 7, Moscow, 125319 Russia

** e-mail: m.kovalenko@voskresensk.ru, m.kovalenko@mtu-net.ru*

1028-3358/03/4801-0042$24.00

transform is a quasi-entire function of exponential type one that is square-integrable in the real axis [4] (we recall that, in the classical case, it is an entire function with the same properties [5]).

Taking Eq. (5) into account, one can represent Eqs. (6) in the compact form

$$D(\lambda)\{S_\nu(\lambda)\} = R_\nu(\lambda), \quad \nu \geq 1, \tag{7}$$

where $S_\nu(\lambda)$ is the Fourier transform of the function $s_\nu(y)$. For each λ_ν, Eq. (7) provides the following ordinary differential equation for the function $S_\nu(\lambda)$:

$$\frac{dS_\nu(\lambda)}{d\lambda} + \left(\frac{1}{\lambda} - \cot\lambda\right)S_\nu(\lambda) = \frac{R_\nu(\lambda)}{\lambda\sin\lambda}, \quad \nu \geq 1, \tag{8}$$

whose solution is $\frac{\sin\lambda}{\lambda}$ const [which is equivalent to the self-balance of function (3)]. The solution of the inhomogeneous equation can be represented as (see [6, p. 440])

$$S_\nu(\lambda) = \frac{\sin\lambda}{\lambda}\int_0^\lambda \frac{R_\nu(t)}{\sin^2 t}dt.$$

Using the Mittag-Leffler expansion [7] for the meromorphic function in the integrand, we represent the function $S_\nu(\lambda)$ in the form

$$S_\nu(\lambda) = -\frac{2\sin\lambda\ln|\lambda|}{\lambda\lambda_\nu^2 r_\nu} - \frac{2\lambda_\nu^2}{r_\nu}\sum_{n=1}^{\infty}\frac{\sin\lambda\ln\left|\lambda^2-\omega_n^2\right|}{\lambda(\omega_n^2-\lambda_\nu^2)^2}$$

$$-\frac{2}{r_\nu}\sum_{n=1}^{\infty}\frac{\omega_n^2\sin\lambda}{\lambda(\lambda^2-\omega_n^2)(\omega_n^2-\lambda_\nu^2)}, \quad \omega_n = n\pi, \tag{9}$$

where both series converge uniformly and are functions square-integrable over the entire axis. Therefore, $S_\nu(\lambda) \in L_2(-\infty, \infty)$. Since the second series consists of entire functions of exponential type one from $L_2(-\infty, \infty)$, it is an entire function with the same properties. Therefore, according to the Paley–Wiener theorem [5], the Fourier transform of the second series is a finite function from $L_2(-1, 1)$. The Fourier transform of the second series is easily found in the form

$$\psi_\nu(y) = \frac{1}{2r_\nu}\left(\frac{\cos\lambda_\nu y}{\lambda_\nu\sin\lambda_\nu} - \frac{1}{\lambda_\nu^2}\right).$$

The first term in Eq. (9) and the terms of the first series are not entire functions. Therefore, their Fourier transforms are not finite functions from the class $L_2(-\infty, \infty)$. Let us consider functions $\frac{\sin\lambda}{\lambda}\ln|\lambda|$ and $\frac{\sin\lambda}{\lambda}\ln\left|\lambda^2-\omega_n^2\right|$ in detail. According to the known property of the logarithm, the latter function is represented as the sum of two functions. Therefore, we can consider all the three functions as one function $\frac{\sin\lambda}{\lambda}\ln|\lambda\mp\omega_n|$, $n = 0, 1, 2,\ldots$, setting $\omega_0 = 0$. For complex λ, this function admits analytic continuation $\frac{\sin\lambda}{\lambda}\ln(\lambda\mp\omega_n)$ as a quasi-entire function of exponential type one that is square-integrable in the real axis [4, 8].

We consider cuts $\{\bar\Gamma: x = 0, |y| \leq 1\}$ and $\{\kappa: y = 0, |x| \leq 0\}$ in the plane $\mathbb{C}(p)$ of the complex variable $p = x + iy$. Let T be the cut formed by the imaginary-axis segment $\bar\Gamma$ and ray κ, and let C be an arbitrary contour enclosing cut T. This contour can consist of a circle, which has its center at the origin and encloses the cut $\bar\Gamma$, and infinite branches over the upper and lower edges of cut κ [8]. We suppose that contour C is passed in the positive (counter-clockwise) direction. In this case, the quasi-entire function $\frac{\sin\lambda}{\lambda}\ln(\lambda\mp\omega_n)$ can be represented as the Borel transform of the function $g_{\mp n}(p)e^{\mp\omega_n p}$ (see [4, p. 768, example 2]), i.e.,

$$\frac{\sin\lambda}{\lambda}\ln(\lambda\mp\omega_n) = \frac{1}{2\pi i}\int_C e^{\mp\omega_n p}g_{\mp n}(p)e^{\lambda p}dp, \quad \mathrm{Re}(\lambda\mp\omega_n) > 0, \quad n = 0, 1, 2, \ldots, \tag{10}$$

where the Borel transform $g_{\mp n}(p)$ of the quasi-entire function $\frac{\sin(\lambda\pm\omega_n)}{\lambda\pm\omega_n}\ln\lambda$ is analytic and single-valued in the region $\mathbb{C}(p)\backslash T$ [4]. To determine function (10) for $\mathrm{Re}(\lambda\mp\omega_n) < 0$, it is necessary to turn cut κ and contour C with respect to the origin by 180° [4, p. 763, Eq. (1.11)].

For quasi-entire exponential-type functions that are square-integrable over the real axis, such as $\frac{\sin\lambda}{\lambda}\ln(\lambda\mp\omega_n)$, the circle enclosing cut $\bar\Gamma$ can approach arbitrarily close to the imaginary axis [4]. In this case, in terms of the following jumps of the function $g_{\mp n}(p)$ in cuts $\bar\Gamma$ and κ:

$$\text{(a)}\ g_{\mp ny}(y) = \frac{1}{2\pi}\lim_{\varepsilon\to 0}[g_{\mp n}(iy+\varepsilon) - g_{\mp n}(iy-\varepsilon)],$$
$$\text{(b)}\ g_{\mp nx}(-u) = \frac{1}{2\pi i}[g_{\mp n}(ue^{-i\pi}) - g_{\mp n}(ue^{i\pi})], \tag{11}$$

where $\varepsilon > 0$ and $-x = u$, the Borel transform given for the quasi-entire function under consideration by

Eq. (10) is represented in the form of the sum of Laplace and Fourier integrals:

$$\frac{\sin\lambda}{\lambda}\ln(\lambda \mp \omega_n) = \int_0^\infty e^{\mp\omega_n u} g_{\mp nx}(-u)e^{-\lambda u}du + \int_{-1}^{1} e^{\mp i\omega_n u} g_{\mp ny}(y)e^{i\lambda y}dy, \quad (12)$$

$$\mathrm{Re}(\lambda \mp \omega_n) > 0, \quad n = 0, 1, 2, \ldots .$$

According to [4, 8], the Laplace integral in Eq. (12) is a quasi-entire minimum-type function. According to the Paley–Wiener theorem [5], the Fourier integral in Eq. (12) is an entire function of exponential type one and is square-integrable in the real axis.

Formula (12) provides the following representation for the analytic continuation $S_{a\nu}(\lambda)$ of function (9) to complex λ:

$$S_{a\nu}(\lambda) = \int_0^\infty s_{\nu x}(-u)e^{-\lambda u}du + \int_{-1}^{1} s_{\nu y}(y)e^{i\lambda y}dy, \quad (13)$$

where

$$s_{\nu x}(-u) = -\frac{2}{\lambda_\nu^2 r_\nu}g_0(-u) - \frac{2\lambda_\nu^2}{r_\nu}\sum_{n=1}^{\infty}\frac{g_{\mp nx}(-u)e^{\pm\omega_n u}}{(\omega_n^2 - \lambda_\nu^2)^2}, \quad u \ge 0,$$

$$s_{\nu y}(y) = -\frac{2}{\lambda_\nu^2 r_\nu}g_0(y) - \frac{2\lambda_\nu^2}{r_\nu}\sum_{n=1}^{\infty}\frac{g_{\mp ny}(y)e^{\pm i\omega_n y}}{(\omega_n^2 - \lambda_\nu^2)^2} + \psi_\nu(y), \quad |y| \le 1. \quad (14)$$

Thus, function $S_{a\nu}(\lambda)$ for each $\nu \ge 1$ is the Borel transform of function $\{s_{\nu x}(-u), s_{\nu y}(y)\}$ defined in contour *T*. We recall that representation (13) is valid for $\mathrm{Re}(\lambda \mp \omega_n) > 0$. To obtain an analogue of Eq. (13) for $\mathrm{Re}(\lambda \mp \omega_n) < 0$, it is necessary, as was mentioned above, to turn cut κ and contour *C* in Eq. (10) by 180° and introduce jumps similar to Eq. (11), but in the positive *x* semiaxis (for more details, see [4]). In what follows, we consider that integrals given by Eqs. (13) are supplemented by the corresponding integrals associated with the turn of the integration contour so that functions $S_{a\nu}(\lambda)$ are defined for all λ. Formula (13) can also be considered as an analytic continuation of the Fourier transform

$$S_\nu(\lambda) = \int_{-\infty}^{\infty} s_\nu(y)e^{i\lambda y}dy$$

to complex λ values, for which the above integral does not exist. In this case, functions $s_\nu(y)$ are definitely related to functions $s_{\nu x}$ and $s_{\nu y}$ [4]. Thus, Eqs. (6) can be replaced by the following formulas valid for complex λ values:

$$\int_0^\infty s_{\nu x}(-u)D(\lambda)\{e^{-\lambda u}\}du + \int_{-1}^{1} s_{\nu y}(y)D(\lambda)\{e^{i\lambda y}\}dy = R_\nu(\lambda), \quad \nu \ge 1, \quad (15)$$

which can be written in the following form equivalent to Eq. (7):

$$D(\lambda)\{S_{a\nu}(\lambda)\} = R_\nu(\lambda), \quad \nu \ge 1. \quad (16)$$

Substitution of $\lambda = \lambda_k$ into Eqs. (15) yields the equalities

$$\int_0^\infty s_{\nu x}(-u)[(\sin\lambda_k - \lambda_k\cos\lambda_k) - \lambda_k u\sin\lambda_k]e^{-\lambda_k u}du + \int_{-1}^{1} s_{\nu y}(y)[(\sin\lambda_k - \lambda_k\cos\lambda_k) + i\lambda_k y\sin\lambda_k]e^{i\lambda_k y}dy = \begin{cases} M_k, & \lambda_k = \lambda_\nu \\ 0, & \lambda_k \ne \lambda_{\nu,} \end{cases} \quad \nu, k \ge 1, \quad (17)$$

which can be treated as the biorthogonal relations for the set of the homogeneous solutions under consideration and, by using Eqs. (16), can be represented in the form

$$D(\lambda)\{S_{a\nu}(\lambda)\}_{\lambda=\lambda_k} = \begin{cases} M_k, & \lambda_\nu = \lambda_k \\ 0, & \lambda_\nu \ne \lambda_k, \end{cases} \quad \nu, k \ge 1. \quad (18)$$

It can be proved that the set of functions that are given by Eqs. (14) and biorthogonal to homogeneous solutions in the sense of Eqs. (17) or (18) is unique in the class of functions for which the Borel transform $S_{a\nu}(\lambda)$ is a quasi-entire function of exponential type one and is square-integrable in the real axis.

Let even self-balanced function $\sigma(\lambda, y)$ given by Eq. (3) be specified in the segment $|y| \le 1$. Taking its expansion (2) in the set of homogeneous solutions given by Eqs. (1), we continue the function to the entire real axis according to Eq. (3). The correspondence

$$\sigma(\lambda, y) \sim \sum_{k=1}^{\infty} A_k\sigma(\lambda_k, y) + \bar{A}_k\sigma(\bar{\lambda}_k, y), \quad \lambda, y \in \mathbb{R} \quad (19)$$

of the resulting function to the series is the even part of

the more general correspondence

$$\sigma_e(\lambda, y) \sim \sum_{k=1}^{\infty} A_k \sigma_e(\lambda_k, y) + \bar{A}_k \sigma_e(\bar{\lambda}_k, y), \quad \lambda, y \in \mathbb{R}. \tag{20}$$

The sign ~ in Eqs. (19) and (20) means that the series on the right-hand sides of Eqs. (19) and (20) cannot converge to the function under consideration over the entire axis $y \in (-\infty, \infty)$. However, these series can converge to this function in the interval (–1, 1) for the corresponding choice of expansion coefficients A_k.

Analytically continuing Eq. (20) to the left-hand half-plane of the complex variable $\mathbb{C}(p)$ and to the semiaxis $x \le 0$ (e.g., as in [4, Sect. 2]) and substituting $-x = u$, we obtain

$$D(\lambda)\{e^{-\lambda u}\} \sim \sum A_k D(\lambda)\{e^{-\lambda u}\}_{\lambda = \lambda_k} + \bar{A}_k D(\lambda)\{e^{-\lambda u}\}_{\lambda = \bar{\lambda}_k}. \tag{21}$$

We multiply Eqs. (20) and (21) by functions $s_{\nu y}(y)$ and $s_{\nu x}(-u)$, respectively, integrate the results with respect to y and u, respectively, over the corresponding supports, and sum the results. In view of Eqs. (15) and (17), we arrive at the ordinary algebraic equation for each $\nu \ge 1$ for the determination of unknown expansion coefficients A_ν. The solution of this equation has the form

$$A_\nu = \frac{R_\nu(\lambda)}{M_\nu}, \quad \nu \ge 1, \quad \lambda \in \mathbb{R}. \tag{22}$$

Statement. *Let variables $y, t \in R$. Then,*

$$\frac{1}{2}[\delta(t+y) + \delta(t-y) - \theta(1-|t|)] = \sum_{k=1}^{\infty} 2\mathrm{Re}\left\{ s_k(t) \frac{\sigma(\lambda_k, y)}{M_k} \right\}, \quad |y| < 1 \tag{23}$$

and

$$\theta(1-|t|)\ln 2 + \frac{1}{2}\sum_{m=1}^{\infty} \frac{\theta(2m+1-|t|) - \theta(2m-1-|t|)}{m} + [\delta(t+1) + \delta(t-1)] = \sum_{k=1}^{\infty} 2\mathrm{Re}\left\{ s_k(t) \frac{\sigma(\lambda_k, 1)}{M_k} \right\},$$

where δ and θ are the delta function and unit step function, respectively.

Thus, series (23) and, therefore, expanded function $f(y)$ generally discontinuous at points $y = \pm 1$. However, function $f(y)$ can always be continued beyond the segment $|y| \le 1$ so that series (23) converges uniformly to the expanded function over the entire segment.

ACKNOWLEDGMENTS

This work was supported by the International Science and Technology Center, project nos. 1536 and 1538.

REFERENCES

1. M. D. Kovalenko and S. V. Shibirin, Dokl. Akad. Nauk **356** (6), 763 (1997) [Phys.-Dokl. **42**, 570 (1997)].
2. B. Ya. Levin, *Root Distribution of Whole Functions* (GITTL, Moscow, 1956).
3. A. F. Leont'ev, *Series of Exponents* (Nauka, Moscow, 1976).
4. M. D. Kovalenko, Fundam. Prikl. Mat. **3**, 761 (2001).
5. N. I. Akhiezer, *Lectures in the Theory of Approximation* (Nauka, Moscow, 1965; Ungar, New York, 1956).
6. I. N. Bronshtein and K. A. Semendyaev, *Handbook on Mathematics* (GITTL, Moscow, 1953).
7. M. A. Lavrent'ev and B. V. Shabat, *Methods of the Theory of Functions of a Complex Variable* (GITTL, Moscow, 1958).
8. A. Pflüger, Comment. Math. Helv **8** (89), 89 (1935/1936).

Translated by R. Tyapaev

Doklady Physics, Vol. 48, No. 1, 2003, pp. 46–50. Translated from Doklady Akademii Nauk, Vol. 388, No. 3, 2003, pp. 329–333.

MECHANICS

Description of Dynamic Effects Accompanying Vibrations of Strings Near T-Beam Stops

V. L. Krupenin

Presented by Academician K.V. Frolov August 5, 2002

Received August 22, 2002

1. The authors of [1–12] theoretically and experimentally investigated vibroimpulsive systems with parallel impact pairs and/or with distributed impact elements and found the possibility of the existence of synchronous periodic regimes of clap-type motion. In these regimes, spatially separated sections of concentrated or distributed impact elements can synchronously collide with the corresponding sections of various stops, and standing-wave profiles are broken. At the same time, the authors of [6, 9–14] investigated strings interacting with point stops of motion, and experimental results for these systems were reported in [14]. The T-beam stop under consideration is simulated by an object composed of the mentioned rectilinear and point stops.

2. We consider a string vibrating near a T-beam stop (Fig. 1a). The extended section of the stop is parallel to the static-equilibrium axis of the string. The desired bend $u(x, t)$; $t \geq 0$, $x \in \left[-\frac{1}{2}, \frac{1}{2}\right]$ satisfies the conditions

$$u(x, t) \geq \Delta > -1; \quad u(0, t) \geq \Delta_1 > \Delta. \tag{1}$$

When these inequalities are strict, the system is described by the linear wave equation $\Box u \equiv u_{tt} - u_{xx} = 0$, where the unit mass per unit length and unit tension are taken without loss of generality. The boundary and initial conditions

$$u\left(-\frac{1}{2}, t\right) = u\left(\frac{1}{2}, t\right) = 0, \; u(x, 0) = u_0(x), \; u_t(x, 0) = 0 \tag{2}$$

are assumed to provide the existence and uniqueness of the solution to the Cauchy problem for the equation $\Box u = 0$, at least in the generalized sense [15]. In addition, when studying standing waves, which are in a certain sense similar to the first form of vibrations, we assume that the function $u_0(x)$ is unimodal and even in the segment $x \in \left[-\frac{1}{2}, \frac{1}{2}\right]$ (Fig. 1a). We derive the relationships describing the interaction of the string with an obstacle.

When string points reach flat sections of the stop, conditions similar to those given in [4, 11] are conserved: for $x \neq 0$, if $u \leq 0$, $\Box u \geq 0$. Using the generalized solutions, we require that $\mathrm{supp}\,\Box u \subset \{(x, t), x = 0, |u(x, t)| = \Delta\}$. It is assumed that, similar to the case of a linear string in the sense of generalized functions, energy is not lost during the impact; i.e., $(|u_x|^2 + |u_t|^2)_t = (2u_t u_x)_x$. In the nonlinear case under consideration, this relationship is postulated and, in particular, expresses the hypothesis of interaction, because it immediately

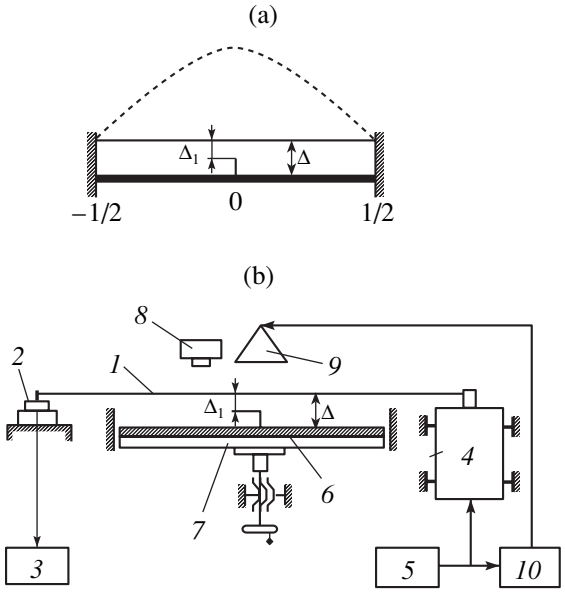

Fig. 1. (a) String and T-beam stop; (b) experimental bench: (*1*) rubber cord, (*2*) force sensor, (*3*) cathode-ray oscilloscope, (*4*) armature of electrodynamic exciter, (*5*) master generator, (*6*) Getinaks T-stop, (*7*) carrier, (*8*) photographic camera, (*9*) lamp, and (*10*) stroboscopic motion analyzer.

Laboratory of Vibroengineering Systems, Blagonravov Institute of Engineering Science, Russian Academy of Sciences, M. Khariton'evskiĭ per. 4, Moscow, 101990 Russia

e-mail: krupenin@online.ru

1028-3358/03/4801-0046$24.00

leads to an analogue of the classical hypothesis about absolutely elastic impact:

$$u_t(x, t-0) = -u_t(x, t+0),$$
$$(x, t) \in \operatorname{supp}\Box u; \quad u(x, t) = \Delta; \quad x \neq 0. \tag{3}$$

The introduction of certain analogues of coefficients of restitution is associated not only with the type of the distributed impact element [6] but also with the type of the established standing wave [3] and is not considered in this paper.

As the middle sections interact with the stops at $x = 0$, temporal lags of the string are formed [10–14]. In this case, during the lag, the reaction force $R_k(t)$ of the "point section" of the stop acts on the string at $u(0, t) = \Delta_1$, where $t \in [t_k, \theta_k]$; t_k and θ_k are the times of the onset and end of the lag, respectively; and k is the integer subscript corresponding to the kth interaction.

In this case, the function $\Phi_0[u]$ that symbolically expresses the force of the impact interaction can be represented as the sum of two generalized functions: $\Phi_0[u] = \Phi_1[u] + \Phi_2[u]$. Moreover, $\Phi_1[u] = J(x)\delta[t - t_n(x)]\gamma(x; \Delta)$ for the nth interaction, where $J(x)$ is the density of the impact momentum; $t_n(x)$ is the distribution of the nth impact "phase" defined in this case as a solution to the equation $u[x, t_n(x)] = \Delta$, where $x \neq 0$; and $\delta(t)$ is the Dirac δ function.

The indicator function $\gamma(x; \Delta) = 0$ for x values at which the string does not interact with the flat section of the stop, and $\gamma(x; \Delta) = 1$ when such an interaction is possible.

For the second component of the interaction force in the certain jth case (cf. [13]),

$$\Phi_2[u] = R_j(t)\delta(x)[\eta(t - t_j) - \eta(t - \theta_j)],$$
$$R_j(t) = u_x(-0, t) - u_x(+0, t) \geq 0, \quad t \in [t_j, \theta_j],$$

where $\eta(t)$ is the unit step function. Consequently, the problem under analysis can be written in the form of the Klein–Gordon nonlinear equation $\Box u - \Phi_0[u] = 0$ with boundary and initial conditions (2).

Considering the conservative nonlinear problem, we seek periodic standing waves with a certain period $T(E) = \dfrac{2\pi}{\omega}$, where ω is the string-vibration frequency and E is the total energy of the system. We use the methods of the time–frequency analysis of the vibroimpulsive processes [9, 15] and pass to the following integral equation of T-periodic vibrations:

$$u(x, t) = \int_0^T \int_{-1/2}^{1/2} \chi(x, y; t - s)\Phi_0[u(x, t - s)]\,ds\,dy. \tag{4}$$

In this case, the periodic Green's function of the string has the form [13, 15]

$$\chi(x, y; t) = \sum \sin\pi n\left(x + \frac{1}{2}\right)\sin\pi n\left(z + \frac{1}{2}\right)\chi_n(t),$$
$$n = 1, 2, \ldots.$$

Here, the functions $\chi_n(t)$ are the "elementary" periodic Green's functions of linear oscillators with the frequencies of the string spectrum $\{\Omega_n\} = \{2\pi n\}$ and, for $0 \leq t < T$, have the form [9, 15]

$$\chi_n(t) = (2\Omega_n \sin 0.5\Omega_n T)^{-1} \times \cos[\Omega_n(t - 0.5T)].$$

Substituting the expression for the impact force into Eq. (4) and assuming that only one interaction event occurs for each period of the desired periodic motion, we represent the desired process in the form

$$u(x, t) = \int_{-1/2}^{-1/2} J(y)\gamma(y; \Delta)\chi(x, y; t - \varphi(y))\,dy + \int_{t\bar{1}}^{\theta_1} R(s)\chi(x, 0; t - s)\,ds, \tag{5}$$

where $\varphi(x)$ is the impact-phase distribution.

3. Studying waves with broken profiles similar to the claps mentioned in Section 1, we put $u_0(x) = L(1 - 2|x|)$ in the second initial condition in Eqs. (2), where $L = \text{const} > 0$ is related to the total energy E in a one-to-one manner. Without the stops, the linear string vibrates with the period $T_0 = 2$.

Standing waves can have two types of profile. If the initial potential energy is insufficient and $|\Delta_1| \leq L$, $|\Delta| > L$, there is a standing wave interacting only with a T-beam projection; this case was discussed in [10–14]. If $|\Delta_1| \leq |\Delta| \leq L$, double interaction (Fig. 2) is possible.

The first case can be considered similar to, for example, [10–14]. According to [10, 13], $t_1 = \dfrac{1}{2}(L - \Delta_1)L^{-1}$, $\theta = 1$, $R(s) = 4L$, and the standing-wave period $T \equiv T_1$ is related to the energy parameter L as $T_1 = \dfrac{1}{2}(3L - \Delta_1)L^{-1}$. Correspondingly, $L(\omega_1) = \Delta_1\omega_1(3\omega_1 - 4\pi)^{-1}$ and $\omega_1 = \dfrac{2\pi}{T_1}$. Since $\Delta_1 < 0$ in this case, vibrations are possible only when $\pi < \omega_1 < \dfrac{4}{3}\pi$. The first inequality follows from the linearity of the system for $\omega_1 = \pi$: $L = -\Delta_1$.

For the second type of profile, $T \equiv T_2 = 1 + 2|\Delta|L^{-1}$. Correspondingly, $L(\omega_2) = 2|\Delta|\omega_2(2\pi - \omega_2)^{-1}$, and vibrations are possible if $\omega_0 < \omega_2 < 2\pi$, where ω_0 is the frequency of free vibrations that corresponds to the occurrence of claps (when string sections reach the flat sec-

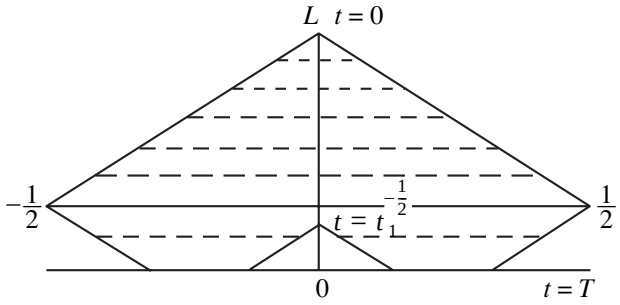

Fig. 2. Profile of the "double-interaction" string.

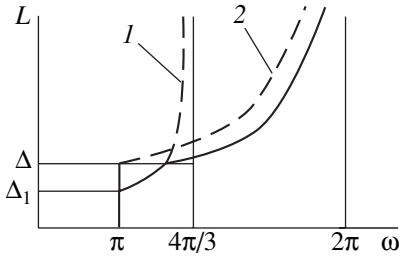

Fig. 3. "Skeleton curve."

tion of the T-stop). It is evident that $\omega_0 = 8\pi|\Delta|(2|\Delta| - |\Delta_1|)^{-1}$.

Figure 3 shows (solid line) the energy parameter $L = L(\omega)$ $\left(\omega = \frac{2\pi}{T}\right.$ is the frequency of free standing waves of the given type$\left.\right)$ for the given standing wave and the "skeleton curves" of the systems with a (*1*) point stop and (*2*) rectilinear extended stop. The solid curve is characteristic for rigid systems [6, 9, 15]. Thus, for this nonlinear system, we obtain the half-interval of "natural" frequencies $\Lambda = \{\omega|\ \omega \in [\pi, 2\pi)\}$ [9, 15].

The parameters that enter into three-functional representation (5) and are necessary for finding the desired standing wave are determined conventionally. For waves of the first type, the problem was virtually solved in [13]. This solution has the form

$$u(x, t) = B_{02}(L; x, t)$$

$$= 8L\sum D_k(t_0; \omega_1; t - \varphi)\sin k\pi\left(1 + \frac{1}{2}\right),$$

where $D_k(t_0; \omega_1; t)$ is the easily calculated T_1-periodic function [13] and the summation is hereafter performed over positive integer subscripts.

After some transformations, waves of the second type (whose evolution is shown in Fig. 2) are represented in the form

$$u(x, t) = B_{01}(L; x, t - \varphi_0) + B_{02}(L; x, t),$$
$$\varphi_0 = 1 + |\Delta|L.$$

Here, the function B_{02} has the form similar to that given above; the limits of integration in Eq. (5) (the lag time) depend on the gap Δ;

$$B_{01}(L;\ x, t - \varphi_0)\ =\ 8L(\pi^2 n)^{-1}\sum\chi_n(t - \varphi_0)$$
$$\times \sin\frac{1}{2}\pi n\left(b + d + \frac{1}{2}\right)\sin\frac{1}{2}\pi nb\sin\pi n\left(x - \frac{1}{2}\right),$$

where the numbers b and d are determined by the geometric parameters Δ and Δ_1 and by the energy parameter L; and $J(y) = 4L$.

4. Designating the obtained solution as $W(L; x, t)$, we consider the problem with more general initial conditions (2): $u(x, 0) = u_0(x)$; $u_t(x, 0) = 0$, where the function $u_0(x)$ is assumed to be even and unimodal at the segment $x \in \left[-\frac{1}{2}; \frac{1}{2}\right]$ (see Section 1).

We seek the solution (see [8, 10–13]) to the general problem in the form

$$u(x, t) = W[L; y_1(x, t); y_2(x, t)],$$
$$y_{1,2}(x, t) = g(x + t) \pm g(x - t).$$

Without loss of generality, we take $L = 1$. The function $g(x)$ depending in particular on the initial and boundary conditions is defined in two steps. First, it is defined for $x \in \left[-\frac{1}{2}; \frac{1}{2}\right]$ as

$$g(x)\ =\ \begin{cases}\frac{1}{2}[1 - u_0(x)], & 0 \le x \le \frac{1}{2}\\ 0, \quad x\ =\ 0\\ \frac{1}{2}[u_0(x) - 1], & -\frac{1}{2} \le x \le 0.\end{cases} \qquad (6)$$

Second, the definition is completed by the two transformations

$$g(x + 1) = \frac{1}{2} - g(-x),\ \ g(x + 2) = 1 + g(x),\ \ x \in R, \quad (7)$$

which convert the function $u_0(x)$ that is unimodal and even on the segment $\left[-\frac{1}{2}; \frac{1}{2}\right]$ into the odd function $g(x)$ increasing monotonically over the whole real axis. In this case, if, for example, $u_0(x) \in C^2\left[-\frac{1}{2}; \frac{1}{2}\right]$, it is easy to show that $g(x) \in C^2(R^1)$. In addition, $-\frac{1}{2} \le y_1(x, t) \le \frac{1}{2}$, $y_1(x, t + 2) = y_1(x, t)$, and $y_2(x, t + 2) = y_2(x, t) + 2$;

Fig. 4. Broken profile of the string in stroboscopic illumination.

i.e., the function y_1 is periodic with the period $T_0 = 2$ of vibrations of the linear string, whereas the function y_2 evolves.

Taking into account the definition of functions g and $y_{1,2}$, it is easy to establish that the representation $u = W$ satisfies the initial equation $\Box u - \Phi_0[u] = 0$, i.e., all the conditions of interaction that were formulated in Section 2, configuration restrictions (1), and boundary conditions (2) (cf. [4]).

Substituting the representation $u = W$ (here, $L = 1$!) into initial Klein–Gordon equation (10), making certain transformations, and taking into account that the sum or difference of two traveling waves satisfies the linear wave equation, we arrive at the equation

$$2g'(x + t)g'(x - t)\Box w - \Phi_0[w(y_1, y_2)] = 0.$$

In this case, taking into account that the function $g(x)$ increases and the solution $W(x, t)$ satisfies the second inequality (1), we find that $W \le 0$ for $\Box W \ge 0$ and arbitrary admissible values of the arguments of the function W. Similarly, we can verify that other conditions from Section 2 are also satisfied, for example, $R_0 = 8g'(t) > 0$.

Thus, the formula $u = W$ does in fact specify the desired process, because the assumption $L = 1$ does not restrict generality. The structure of this solution is completely determined by the structure of the above representing series B_{01} and B_{02}; i.e., the solution is constructed as a series every term of which is the product of a T-periodic time function Q_{1k} by a certain function Q_{2k} of the coordinate x:

$$u(x, t) = w[L; y_1(x, t); y_2(x, t)]$$

$$= \sum Q_{1k}[L; y_1(x, t)]Q_{2k}[L; y_2(x, t)].$$

All the functions Q_{1k} are T-periodic functions of the variable y_1 and, at the same time, $y_1(x, t + 2) \equiv y_1(x, t)$ and $y_2(x, t + 2) \equiv y_2(x, t) + 2$. The period (see Section 3) is $T = T_1 = \frac{1}{2}(3L_* - \Delta_1)L^{-1}$ for $|\Delta_1| \le L$, $|\Delta| > L$, $|\Delta_1| \le |\Delta| \le L$, and $T = T_2 = 1 + 2|\Delta|L^{-1}$ for $|\Delta_1| \le |\Delta| \le L$. The last series defines a periodic process if and only if the quantities T and $T_0 = 2$ are commensurable. Thus, the problem under study can have a periodic solution if and only if the period T is a rational number. Otherwise, the solution is almost periodic (cf. [8, 10–13]).

The methods of time–frequency analysis can be similarly applied to other cases, such as a stop with a T-beam on either side of the string and various combinations of the stop types. In addition, solutions can also be constructed for systems with weak nonconservative forces.

5. Figure 1b shows the layout of the Alligator–T-Beam experimental bench. T-beam stop *6*, which is made of Getinaks (a paper-based laminate), is mounted on carrier *7* handled by a micrometer screw, which varies the adjustable gap Δ. Rubber cord *1* is used as a distributed elastic element. Standing waves are visualized by stroboscopic motion analyzer *10*, and the flashes of lamp *9* are synchronized by pulses from the master generator.

The experimental results agree satisfactorily with the above conclusions.

We visualized periodic standing waves of only the two types described above. The waves of the first type were observed upon passing linear resonance and were the same as those described in [14]. The waves of the second type arose when increasing the excitation amplitude, excitation frequency (frequency pulling), or gap Δ (amplitude pulling).

Figure 4 shows the characteristic profile of the string for $f = 27.3$ Hz, $\Delta_1 = 20$ mm, and $\Delta = 25$ mm (the photography was performed by A.I. Sternin). Using this installation for regimes with trapezoidal profiles of claps, we detected the usual dynamic effects characteristic for "impact vibrators" [3, 4, 9, 14, 15]. In addition, aperiodic waves of a more complicated nature were also detected.

ACKNOWLEDGMENTS

This work was supported by the Russian Foundation for Basic Research, project no. 01-01-00297.

REFERENCES

1. L. Amerio and G. Prouse, Rend. Mat. Ser. **6**/**8** (2), 563 (1975).
2. V. L. Krupenin, Izv. Akad. Nauk SSSR, Mekh. Tverd. Tela, No. 1, 25 (1986).
3. A. M. Veprik and V. L. Krupenin, Mashinovedenie, No. 6, 39 (1988).
4. V. L. Krupenin, Dokl. Akad. Nauk **313** (6), 1390 (1990) [Sov. Phys. Dokl. **35**, 743 (1990)].

5. V. L. Krupenin and A. M. Veprik, in *Proceedings of the II European Conference on Nonlinear Oscillations, Czech* (CTU, Prague, 1996), Vol. 1, p. 229.
6. V. K. Astashev and V. L. Krupenin, Probl. Mashinostr. Nadezhnosti Mash., No. 5, 13 (1998).
7. V. L. Krupenin, in *Proceedings of the Euromech Colloquium, Sept. 15–18, 1998* (Springer, Heidelberg, 1999), p. 39.
8. V. L. Krupenin, Probl. Mashinostr. Nadezhnosti Mash., No. 3, 20 (1997).
9. V. L. Babitsky and V. L. Krupenin, *Vibration of Strongly Nonlinear Discontinuous Systems* (Springer, Heidelberg, 2001).
10. H. Cabannes and A. Haraus, Int. J. Nonlinear Mech. **55** (5/6), 449 (1981).
11. H. Cabannes, Acustica **55**, 14 (1984).
12. C. Citrini and C. Marchionna, Eur. J. Mech. A/Solids **8** (1), 73 (1989).
13. V. L. Krupenin, Probl. Mashinostr. Nadezhnosti Mash., No. 2, 29 (1992).
14. V. K. Astashev and V. L. Krupenin, Dokl. Akad. Nauk **379** (3), 23 (2001).
15. V. I. Babitskiĭ and V. L. Krupenin, *Vibrations in Strong Nonlinear Systems* (Nauka, Moscow, 1985).

Translated by V. Bukhanov

Doklady Physics, Vol. 48, No. 1, 2003, pp. 5–8. Translated from Doklady Akademii Nauk, Vol. 388, No. 1, 2003, pp. 41–45.

PHYSICS

Possible Relation between Optical Breakdown and Metallization of Extremely Pure Transparent Dielectrics

S. V. Karpenko[1,*], A. P. Savintsev[2], and A. I. Temrokov[1]

Presented by Academician V.E. Fortov March 3, 2002

Received April 17, 2002

The development of laser facilities and in particular of the technique of generating intense light fluxes is being held back, because intense laser radiation induces an optical breakdown leading to irreversible changes in the optical elements of lasers. Interest in the optical-breakdown phenomenon in transparent dielectrics is primarily associated with the practical requirements of laser facilities, because the focusing and transfer of intense laser pulses are impossible without revealing mechanisms of the laser destruction of dielectrics. Laser destruction is of its own scientific interest as one of the fundamental problems concerning the physics of the interaction of intense electromagnetic radiation with matter.

In this paper, we propose a mechanism of the optical breakdown of extremely pure solid dielectrics that is associated with the stepwise narrowing of the gap, i.e., with the metallization of a dielectric in the intense field of the light wave of laser radiation. Metallization theory is treated in terms of the electron density functional.

The theoretical concept of the mechanism of optical self-breakdown is based on familiar experimental facts [1–3]. Laser radiation interacting with a substance is supposed to induce intense tunnel, impact, or multiphoton ionization of the substance matrix [4, 5]. This ionization results in the nonlinear accumulation of free charges, which, in turn, gives rise to an increase in absorption, production of plasma in the focal volume, and further destruction of a sample in intense light fields.

However, the previous mechanisms of optical breakdown do not explain the entire body of experimental data. In particular, familiar mechanisms of optical self-breakdown imply the pre-threshold ionization of the matrix; i.e., the appearance of free electrons accompanies pre-threshold excitation. However, experiments [1, 5] demonstrate in particular that the formation of color centers and self-luminescence in silicate glasses and quartz, where breakdown thresholds are very high (about 10^{13} W/cm^2), are not observed, even when the power of laser radiation is equal to 0.95–0.98 of the threshold power, if the energy of a radiation quantum is lower than $0.5E_{gv}$, where E_{gv} is the width of the dielectric gap in volume. These results cannot be explained by avalanche and multiphoton ionization. In particular, it is difficult for this theory to explain the experimental observation that the threshold of optical breakdown depends only slightly on the incident-light frequency, because the probability $\omega^{(n)}$ of the n-photon process is proportional to the nth power of the incident-radiation intensity I; i.e., $\omega^{(n)} \sim I^n$ [6].

Glebov *et al.* [1, 5] proposed a mechanism of the optical self-breakdown of dielectrics that was attributed to the stepwise change in the optical parameters of a medium, in particular, to the stepwise appearance of the spectrum of electron states corresponding to the delocalization of valence electrons, i.e., the metallization of the substance at the breakdown strength of the electric field of laser radiation. In a definite sense, this transformation is similar to the Mott dielectric–metal transition [7] but concerns only the electron subsystem. As a result, a metallic nucleus is formed at the center of the caustic of the focusing lens. The absorption of laser radiation in this nucleus gives rise to the appearance of a plasma cloud in the focal volume and the further destruction of the sample.

According to experimental data [4, 8], laser radiation induces a pressure of several megabars in a dielectric. Let us estimate the pressure of omnidirectional compression at which the gap of the dielectric disappears (metallization occurs).

We consider alkali halide crystals, whose thresholds of breakdown by laser radiation are on the same order of magnitude as corresponding values for silicate glasses [9]. The behavior of energy bands for compression of a crystal is shown schematically in Fig. 1, where E_1 and E_2 are the electron energy levels in the filled and empty bands, respectively; the equilibrium interparticle

[1] *Research Institute of Applied Mathematics and Automation, Kabardino-Balkar Scientific Center, Russian Academy of Sciences, Nalchik, Russia*

[2] *Kabardino-Balkar State University, ul. Chernyshevskogo 173, Nalchik, 360004 Russia*

* *e-mail: sv_karpenko@mailru.com*

1028-3358/03/4801-0005$24.00

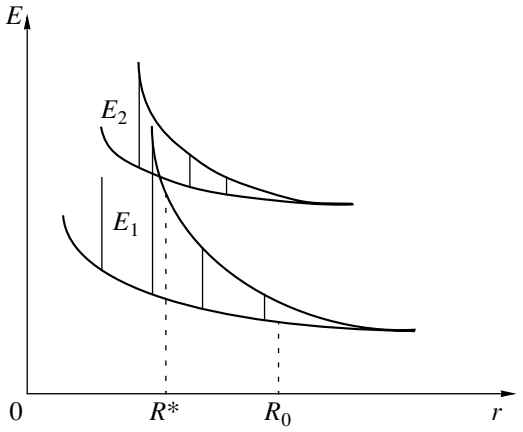

Schematic behavior of the energy bands of a compressed crystal.

spacing R_0 at normal pressure corresponds to the minimum of the thermodynamic potential of the crystal; and R^* is the interatomic spacing in the crystal when the energy bands intersect. When the crystal is compressed, bands are shifted upward by different amounts. Some levels of lower bands often rise faster than levels of upper free bands. When the upper level of a filled band intersects with the lower level of an empty band, electrons can occupy energy levels in both bands. Beginning with this instant, an electron of the crystal can gain kinetic energy from the external electric field. Therefore, the crystal becomes a conductor; i.e., it transitions to the metallized state. In this study, the omnidirectional-compression pressure at which a dielectric is metallized is calculated in the electron-statistical model by the density-functional method [10].

We consider ion crystals with the NaCl-type lattice (B1 structure). These crystals undergo polymorphic transition to the B2 structure at pressures of tens and hundreds of kilobars (which are much lower than the metallization pressure) [10, 11]. For this reason, the thermodynamics of the ion-crystal phase will be described in the model of a perfect crystalline lattice having B2 structure (CsCl type) consisting of point charges of opposite sign [11]. Temperature is taken to be equal to absolute zero. The thermodynamic potential of the ion lattice has the form [11]

$$G_{B2}(R) = \sum_{j=1}^{7} N_j U_j(a_j R) - \frac{\alpha_\mu}{R} - V\frac{\partial}{\partial V}\left[\sum_{j=1}^{7} N_j U_j(a_j R)\right], \quad (1)$$

where $\alpha_\mu = 1.76268$ is the Madelung constant of the B2 structure; $U_{B2}(R) = \sum_{j=1}^{7} N_j U_j(a_j R)$ is the pair interaction potential of ions, which is self-consistently calculated in the theory of an inhomogeneous electron gas [10]; $a_j = R_j/R_1$ is the ratio of the radii of the jth and first coordination spheres; and N_j is the number of nearest neighbors in the jth coordination sphere.

Thermodynamic potential (1) must be supplemented by the following term corresponding to the surface energy of the crystal [11]:

$$G_{B2}^{surf} = 4\pi r^2 K\sigma, \quad (2)$$

where σ is the specific free surface energy (surface energy in what follows), r is the radius of the crystalline nucleus, and K is the factor representing the deviation of the crystal shape from the perfect spherical shape, for which $K = 1$. The surface energy is calculated by summing over the plane grids within the semi-infinite crystal. In the zeroth approximation, we have [11]

$$\sigma(nkl) = \frac{1}{2} n_0(nkl)\sum_i (\beta^{(i)} - 1) W_\infty^{(i)}, \quad (3)$$

where $\beta^{(i)} = \dfrac{W_S^{(i)}}{W_\infty^{(i)}}$ is the ratio of the sums over the infinite plane grid and infinite lattice for the ith type of the interaction between ions; n_0 is the number of particles per unit area of the grid; n, k, and l are the Miller indices; and $W_S^{(i)}$ and $W_\infty^{(i)}$ are the ith-type interaction energy of a particle in the grid and in the bulk of the crystal, respectively.

Thus, the thermodynamic potential of the dielectric phase of the ion crystal is written as

$$G_{B2} = \sum_{j=1}^{7} N_j U_j(a_j R) - V\frac{\partial}{\partial V}\left[\sum_{j=1}^{7} N_j U_j(a_j R)\right] - \frac{\alpha_\mu}{R} + 2\pi r^2 K n_0(nkl)\sum_i (\beta^{(i)} - 1) W_\infty^{(i)}. \quad (4)$$

In what follows, the dielectric phase with the CsCl structure and metallized state of the crystal will be referred to as phases I and II, respectively. In calculations, we suppose that the surface for phase I consists of (110) faces, for which the surface energy is minimal. The thermodynamic potential of this phase is calculated by Eq. (4) for $T = 0$ K.

The thermodynamic potential of the metallized phase is calculated (volume part) in the Gombas model [12], which satisfactorily describes the properties of alkali metals, and (surface part) in the jellium model [10].

According to the former model, the metal-lattice energy per pair of atoms is

$$U_m = -0.0772Z - \frac{0.9Z^2 + 0.516Z^{4/3}}{R_m} + \frac{1.105Z^{5/3}}{R_m^2} + \frac{3Z\left(\frac{Zr_0^2}{6} - \frac{5r_0^2}{32\pi}\right)}{R_m^3} + \left(\frac{3}{4\pi}\right)^{\frac{1}{3}} C_a r_0^3 \frac{Z^{\frac{4}{3}}}{R_m}, \quad (5)$$

where Z is the oxidation state of the metal, R_m is the nearest-neighbor spacing, r_0 is the radius of the ion in the metal, and $C_a = 0.738$ is the constant of the Gombas model. In order to determine the oxidation state of the metallized phase, we consider NaCl, where the conduction band is formed by single (double) ionization of negative halogen ions. Since the ionization potential of a Na^+ ion is high (47.25 eV), this ion is unlikely to lose an electron. The metal with $Z = 0.5$ appears to be energetically favorable, because the ionization potential of a Cl atom is quite high (13 eV), and the energy gain appearing upon the transition to phase II is compensated by the energy necessary to form Na^+ ions. Thus, the lattice of the metallized phase consists of Na^+ ions and Cl atoms, and one valence electron falls per lattice volume V_m corresponding to a pair of these atoms.

The volume part of the thermodynamic potential of phase II in the presence of external pressure is

$$G_{mv} = N\left(U_m - \frac{\partial U_m}{\partial V_m} V_m\right), \quad (6)$$

where N is the number of pairs of oppositely charged ions in the original crystal.

The surface energy of the metallized phase is calculated by the following jellium-model [10] formula, which disregards both the contribution from the ion sublattice and the discreteness of ions:

$$\sigma_m = -\frac{C}{\beta^3} - \frac{B}{\beta} + A\beta, \quad (7)$$

where

$$A = 9.67 \times 10^{-3} n_+,$$

$$B = -5.266 C_a n_+^{4/3} - 2.289 C_a n_+^{4/3} + \frac{0.22 n_+}{\beta(1 + 0.079 n_+^{4/3})} + 0.084 n_+ \left(\frac{1}{3} - \frac{\alpha}{2} + \alpha^2 + \alpha^3 \ln\frac{\alpha}{1+\alpha}\right),$$

$$C = -1.5\pi n_+^2,$$

$\alpha = 0.079\left(\frac{2}{n_+}\right)^{1/3}$, and $\beta = 2.18$ [10]. The valence-electron density n_+ is related to the distance R_m of phase II as

$$n_+ = \frac{3\sqrt{3}}{8} R_m^{-3}. \quad (8)$$

Taking Eqs. (6) and (7) into account, we obtain the total thermodynamic potential of the cubic crystal in the form

$$G_{II} = G_{mv} + AN + 6d_m^2 \sigma_m N, \quad (9)$$

where A is the electron affinity potential for Cl and d_m is the length of the crystal edge in phase II.

Calculations are simplified by supposing that parameter β depends only slightly on the jellium density n_+, which varies with increasing pressure. This supposition is supported by the fact that this parameter takes very close values for metals whose n_+ values differ by an order of magnitude [10]. Thus, the metallization pressure can be determined from the equality of the thermodynamic potentials of phases I and II:

$$G_I = G_{II}. \quad (10)$$

Our results for the metallization pressure for massive samples are presented in the table, which also includes the results of other studies [13–15] where the metallization pressure for ion crystals was calculated. For comparison, the table also presents our results for the pressure of polymorphic B1–B2 transition, which occurs under the omnidirectional compression of a crystal [11].

Similar to the polymorphic transformation [11], the metallization pressure increases as the size of a crystal sample under investigation decreases. In [11], we observed that, in contrast to other alkali-halide crystals, the pressure of polymorphic transformation for a LiF crystal decreases rather than increases as its size

Pressures of metallization and polymorphic B1–B2 transition in massive samples of alkali-halide crystals

Crystal	p_{met}, Mbar				p(B1–B2), kbar [11]
	this study	[13]	[14]	[15]	
LiF	27	–	–	–	300
LiCl	20	–	14	–	149
LiBr	18	–	–	–	100
NaF	22	–	–	–	154
NaCl	15	1.3	11	13	138
NaBr	12	1.7	16	–	45
KF	9	0.8	–	17	89
KCl	6	0.5	4	10	29
KBr	5	–	–	–	29
RbF	2	–	–	–	34
RbCl	2	–	–	–	17
RbBr	1.5	–	–	–	14

decreases. This behavior is attributed to the fact that the surface energy of this compound in the B2 structure is lower than the value in the B1 structure. For this reason, the inclusion of the surface contribution to the thermodynamic potential of the crystal "accelerates" the phase transition and reduces the pressure of polymorphic transformation. However, in the dielectric–metal transition, the LiF crystal behaves similarly to other alkali-halide compounds being investigated; i.e., the metallization pressure increases with decreasing sample size. The density-functional calculation indicates that the surface energy of the metallized phase of LiF is higher than the value for the dielectric phase with the CsCl structure by 15–20%. Therefore, it is reasonable to expect an increase in the metallization pressure for small samples. Our calculations corroborate this expectation.

On the whole, our calculations for the metallization pressure agree satisfactorily with the results obtained by other authors, except the results of [13], where data are obviously underestimated. On the other hand, the electron effects ignored in our model must be taken into account more rigorously. In particular, effects associated with the deformation of electron shells of atoms when a crystal is compressed must be analyzed further, and shell effects may contribute considerably.

Thus, the pressures at which the dielectric–metal phase transition takes place were calculated by the method of the electron density functional, and the results indicate that the pressure induced in dielectrics, including alkali-halide crystals, under optical breakdown caused by an intense laser pulse is approximately equal to the omnidirectional-compression pressure at which a substance is metallized. Therefore, the optical breakdown of extremely pure transparent dielectrics can result from the stepwise narrowing of the gap in an intense field of a light wave due to high pressures.

REFERENCES

1. L. B. Glebov, O. M. Efimov, M. N. Libenson, and G. T. Petrovskiĭ, Dokl. Akad. Nauk **287** (5), 1114 (1986).
2. A. A. Manenkov and A. M. Prokhorov, Usp. Fiz. Nauk **148** (1), 179 (1986).
3. S. Satpathy, N. E. Christensen, and O. Jepsen, Phys. Rev. B **32**, 6793 (1985).
4. S. I. Anisimov, A. M. Prokhorov, and V. E. Fortov, Usp. Fiz. Nauk **142** (3), 395 (1984).
5. L. B. Glebov, O. M. Efimov, and G. T. Petrovskiĭ, Kvantovaya Élektron. (Moscow) **10** (3), 1490 (1983).
6. N. B. Delone and V. P. Krainov, *Nonlinear Ionization of Atoms by Laser Radiation* (Fizmatlit, Moscow, 2001).
7. N. F. Mott, *Metal–Insulator Transitions* (Taylor & Francis, London, 1974; Nauka, Moscow, 1979).
8. A. N. Babushkin and A. Yu. Volkova, in *Proceedings of the XVII International Conference on State Equations of Matter, Chernogolovka, Inst. of Problems of Chemical Physics, 2002*, p. 30.
9. A. Yu. Basharin and A. P. Savintsev, in *Proceedings of the XVII International Conference on State Equations of Matter, Chernogolovka, Inst. of Problems of Chemical Physics, 2002*, p. 109.
10. V. F. Ukhov, R. M. Kobeleva, G. V. Dedkov, and A. I. Temrokov, *Electronic and Statistical Theory of Metals and Ionic Crystals* (Nauka, Moscow, 1982).
11. D. L. Vinokurskiĭ, S. V. Karpenko, A. Kh. Kyarov, and A. I. Temrokov, Dokl. Akad. Nauk **381** (6), 756 (2001) [Dokl. Phys. **46**, 835 (2001)].
12. P. Gombas, *Die Statistische Theorie des Atoms und ihre Anwendungen* (Springer-Verlag, Wein, 1949; Inostrannaya Literatura, Moscow, 1951).
13. V. A. Zhdanov, V. A. Kuchin, and V. V. Polyakov, Izv. Vyssh. Uchebn. Zaved. Fiz., No. 3, 57 (1973).
14. J. L. Feldman, B. M. Klein, M. J. Mehl, and H. Krakauer, Phys. Rev. B **42**, 2752 (1990).
15. A. K. McMahan, Phys. Rev. B **29**, 5982 (1984).

Translated by R. Tyapaev

Doklady Physics, Vol. 48, No. 1, 2003, pp. 51–55. Translated from Doklady Akademii Nauk, Vol. 388, No. 3, 2003, pp. 334–339.

MECHANICS

Sound Scattering in a Wake beyond a Vortex Ring in a Continuously Stratified Liquid

V. E. Prokhorov and Yu. D. Chashechkin

Presented by Academician A.Yu. Ishlinskiĭ September 23, 2002

Received September 30, 2002

Acoustical probing is one of the rapidly developing methods aimed at determining physical properties and identifying processes in both a stratified ocean and the atmosphere [1, 2]. In this connection, the problem arises to determine the nature of elementary scatterers that may have physical (bubbles and suspensions), biological, or mechanical (turbulence, vortices, discontinuities) origin. The identification is based on empirical regularities for the given class of scatterers [3], which are found in scale-sized and laboratory conditions. Recently, when studying scattering on turbulent flows in fluids [1] and gases [2], particular attention was given to the role of compact formations, i.e., plane vortex bundles and ring vortices, as well as coherent structures [4–6]. In this case, we observe the existence of zero scattering levels in the forward and backward directions. These levels are determined by the form of the scattering coefficient when the scattering occurs on an immobile single two-dimensional vortex with the circulation parameter Γ:

$$\frac{\rho_s}{\rho_i} = \frac{\varepsilon}{\sqrt{2}}\left|2i\sum_{m=1}^{\infty}\phi_m \sin(i\theta m)\right|. \qquad (1)$$

Here, ρ_i and ρ_s are the amplitudes of density variations in the incident and scattered waves, $\varepsilon = \dfrac{\Gamma}{c_0\lambda} \ll 1$ is a small parameter of the problem, θ is the angle between the vectors of the impinging and scattered waves, ϕ_m is the eigenfunction of the problem under consideration, c_0 is the unperturbed speed of sound, and λ is the wavelength of the sonic wave. The equation of state is taken in the form $p\rho^{-\gamma} = \text{const}$, where γ is the adiabatic constant [4].

Institute for Problems in Mechanics,
Russian Academy of Sciences,
pr. Vernadskogo 101, building 1, Moscow, 119526 Russia
e-mail: prohorov@ipmnet.ru, chakin@ipmnet.ru

Solution (1) has been constructed under the assumption of the smallness of the parameter ε and uses nonreflective boundary conditions. This solution agrees with the results of laboratory experiments conducted in the air medium [4]. However, according to data of the laboratory experiments in a stratified fluid [5], a compact vortex intensely scatters ultrasound in all directions similarly to the hydrodynamic wake beyond an obstacle [6].

In the present paper, we describe results of the ultrasound backscattering from both a sole vortex ring moving in a continuously stratified fluid and its hydrodynamic wake while simultaneously recording the optical pattern of the flow by the shadow method.

The experiments were carried out in a basin with the dimensions $240 \times 60 \times 40$ cm^3, which was filled with linearly stratified solution of the common salt. The buoyancy period T_b was determined by measurements with a contact sensor detecting the electrical conduction of fluctuations excited by a density marker and attained 6.7 s in the experiments under discussion.

The vortex ring moving in the horizontal direction is formed by a pulse pushing on a portion of the fluid from a nozzle 2 cm in diameter [5]. The flow pattern and density markers are observed from the side by an IAB-458 shadow device (with a visual-field diameter of 23 cm). The photograms of shadow images are introduced into a computer to be used in the calculation of spatial spectra and determination of perturbation scales on the basis of software developed in the "Matlab" medium. A vortex and its wake are probed by a vertical sonic beam in pulse mode (with a carrying frequency of 1 MHz, pulse duration of 40 μs, repetition period of 0.32 s, and beam width of 3 cm at the vortex-motion horizon). A signal formed as a result of sonic-beam reflection from the basin bed made of organic glass is employed for the active-sonar calibration. Echo signals are introduced via a special interface in real-time mode into a personal computer and are stored in the form of a two-dimensional matrix. Each matrix element corresponds to the current scattering level, while the ordering numbers of the matrix rows and columns correspond to the occurrence depth of a scattering inhomogeneity and to a current time, respectively. In this experiment, a receiver

1028-3358/03/4801-0051$24.00

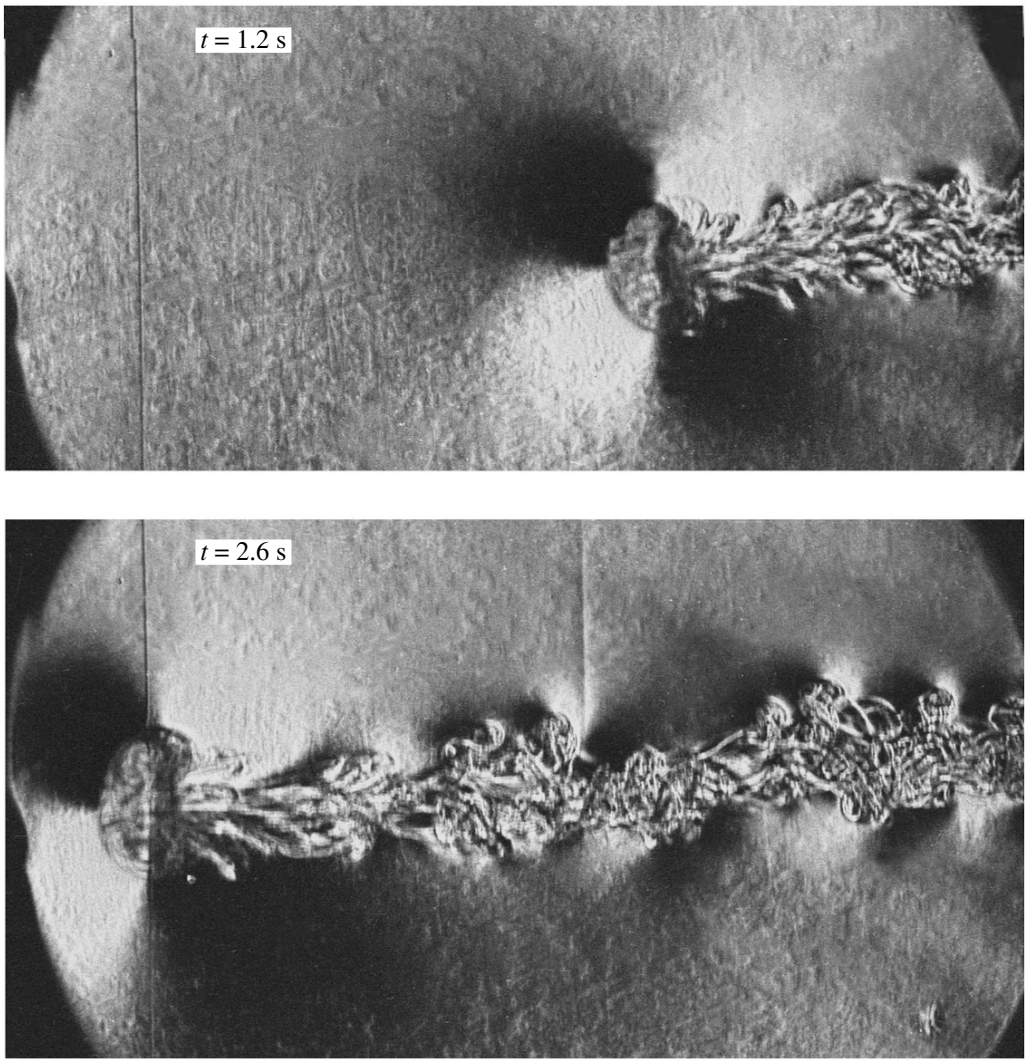

Fig. 1. Successive schlieren photograms of a ring vortex moving in a stratified liquid. The time elapsed from the start is (a) $t = 1.2$ and (b) 2.6 s.

with electronic gain adjustment and a dynamic range of 4×10^3 is employed. The data-processing software performs data grouping, transformation of echograms into periodgrams, and spectral analysis. For comparison with available scale-sized data, the output scattering levels are estimated in units of the dimensionless scattering cross section $\sigma = m_V\lambda$, where m_V is the cross section for scattering per unit volume per unit solid angle and λ is the wavelength of the sonic wave [5].

Consequent photograms of a vortex with a diameter $D = 3$ cm, which moves with a velocity $U = 8$ cm s^{-1}, as well as the wake beyond it, are presented in Fig. 1. The dimensionless quantities being determined by the vortex parameters are the Reynolds number $\mathrm{Re} = \frac{UD}{\nu} = 2200$, the Frude number $\mathrm{Fr} = \frac{U}{ND} = 2.8$, and the dimensionless stratification scale $C = \frac{g}{N^2 D} = 370$. Here, g is the acceleration of gravity and $\nu = 0.01$ cm^2 s^{-1} is the kinematic viscosity.

The light and dark spots ahead of the vortex illustrate a blocking effect: the damping of the fluid, which is similar to that ahead of a solid three-dimensional obstacle [7]. The leading high-gradient vortex shell with low-scale shape inhomogeneities is more convex than the bed one. A thin finely structured density wake adjoins the vortex. At the external boundary of this wake, regular secondary structures characteristic of the given mode and represented by a sequence of thin vortices are clearly seen. As is shown in Fig. 1, the motion trajectory is a wavy line, which is caused by a small inclination of the vortex at the initial moment. Buoyancy forces return the vortex to the horizon of neutral buoyancy and symmetrize the vortex shape.

The thin vertical line at the center in Fig. 1 ($t = 2.6$ s) is the density wake beyond the gas bubble captured at the moment of vortex appearance. The bubble floats up vertically after escaping from the wake domain. In the case under consideration, the bubble resides within the zone subjected to the action of the sound. This allows us to record it by the scattered signal at a considerable segment of the trajectory.

The scattering level R (vertical axis) normalized to its maximum value R_m as a function of the depth and the dimensionless age $\left(t_\mathrm{b} = \dfrac{t}{T_\mathrm{b}}\right)$ of the vortex flow shown in Fig. 1 is presented in Fig. 2. In it, three groups of signals are isolated. The first group is represented by two pulses that correspond to the vortex motion across the sonic beam. The second group adjoins the first group. The second group is composed of signals with increasing amplitudes, which come from depths rapidly decreasing with time according to a linear law. Comparison with the shadow pattern (Fig. 1, $t = 2.6$ s) makes it possible to identify this sequence as an echo from the air bubble floating up with constant velocity. As the bubble floats up, its radius increases, the intensity of scattering by the bubble enhances and begins to exceed the level of scattering by the vortex. The commensurability of the scattering intensities testifies to a rather high scattering capability of a sole vortex, since air bubbles are considered to be the most intense scatterers of sound in seas and they exceed in this extent biological and hydrophysical components [3].

The third group of the scattering signals $\dfrac{R}{R_m}$, with considerably smaller amplitudes, is positioned along the time axis. The depth of occurrence for this group virtually does not vary with time. This group represents echo signals from the wake that, residues near a horizon of the neutral buoyancy in which the vortex moves. The lifetime of the acoustical wake for the given mode of the motion attains about four buoyancy periods. In this case, the optical wake, whose initial segment was shown in Fig. 1, is visualized in the density-gradient field for a longer time (on the order of 50 T_b).

The relation between the scattering levels for the vortex and the wake is illustrated by the time dependence of the dimensionless backscattering cross section σ (Fig. 2). This cross section is an invariant of the acoustical modeling. The given curve is calculated using values of the echo signal, which are extracted from the 28-cm horizon with a moving average within a 0.6-s time window. The maximum echo levels (10^{-5}–10^{-8}) are observed within the initial segment, which corresponds to the passage of the vortex, of the air bubble, and of the near wake. In the far wake, the average scattering levels are lower by almost three orders of magnitude. The maximum values of the scattering cross section, which were measured at the moment of the vortex passage, correspond to those

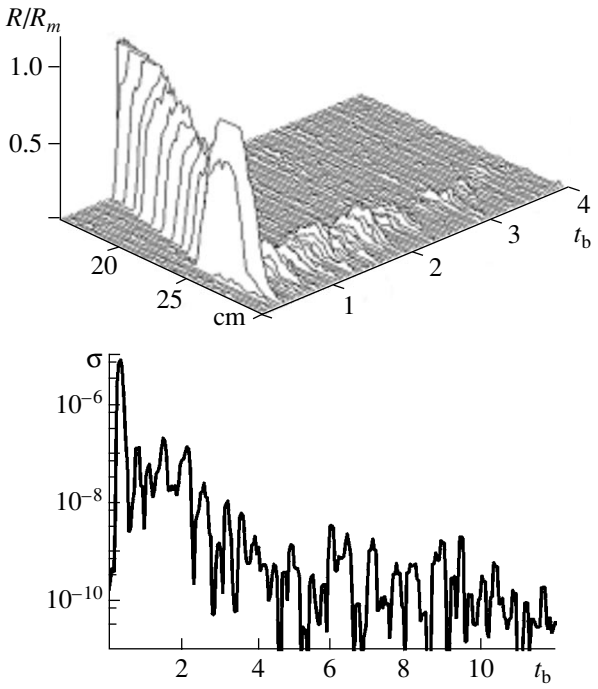

Fig. 2. Echo-signal characteristics for a vortex flow: the normalized level of backscattering $\dfrac{R}{R_m}$ and dimensionless cross section σ of volume scattering are shown.

observed in the ocean in the case of scattering by bubbles. In sea conditions, signals on the order of 10^{-6}–10^{-8} and of 10^{-9} and lower are formed by a fine dispersed biological suspension and by turbulence, respectively [3]. Thus, the ring vortex of an average intensity and its wake form an echo signal whose variability range covers the sound-scattering levels in the natural medium.

In digital form, the wake fragment shown in Fig. 3 is a matrix with the values of its elements characterizing the blackening density of the shadow image, the ordering numbers of rows and columns corresponding to the horizontal coordinate with the step of 0.017 cm. The matrix obtained is applied in calculations of spatial spectra for the gradient of the blackening density of the optical image, which is proportional to the fluid-density gradient. As a result of the calculation, two matrices are obtained, each of them containing a family of one-dimensional spectra $S_x(\kappa_x)$ and $S_z(\kappa_z)$ for horizontal κ_x and vertical κ_z wave numbers [6]. The spectral families obtained characterize the distribution of the vertical scales along the horizontal coordinate x and of the horizontal scales over the depth z. The amplitudes S_x and S_z normalized to the absolute maximum of the spectral matrix are expressed in terms of the blackening intensity in the (z, κ_x) and (x, κ_z) planes (Fig. 3).

The spectrum S_x of horizontal wave numbers expresses the symmetry of the basic flow pattern with respect to the wake axis. This spectrum is concentrated

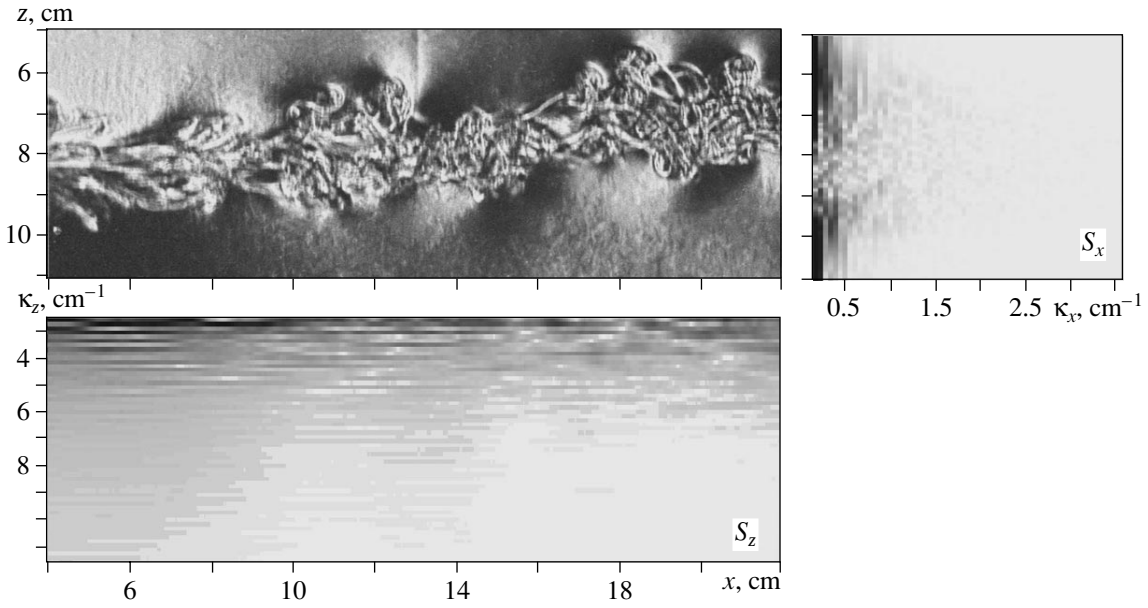

Fig. 3. Schlieren image of a wake fragment and its spectral images S_x and S_z.

in a considerably narrower range of wave numbers than the spectrum of vertical wave numbers S_z (vertical spectrum). The comparison of halftone images of the spectra S_x and S_z exhibits sharp anisotropy of the wake structure in which extended horizontal scales (where $\kappa_x < 1.5$ cm^{-1}) are combined with short vertical ones (where $\kappa_z > 10$ cm^{-1}). An increase in the vertical wake sizes is limited by buoyancy forces that do not affect the flow in the horizontal plane.

In the left part of the vertical spectrum in Fig. 3, the sequence of contrasting horizontal bands with 0.6-cm^{-1} steps is clearly seen. This sequence corresponds to the spectrum of a rectangle with the width of 1.7 cm, which is equal to the average height of the initial wake segment. The upper spectrum boundary κ_m characterizes fine-structure flow elements. At the wake onset, κ_m attains about 10 cm^{-1} and then decreases and is stabilized at the value of 6.5 cm^{-1} at distances exceeding 10 cm from the vortex core. The given wave number corresponds to inhomogeneities of the scale δ = 0.15 cm, which coincide with the sound wavelength. Structures on such a scale are efficient coherent ultrasound scatterers.

These anisotropic structures form the directed scattering with maxima corresponding to the mirror direction (with respect to the horizontal plane). As far as the scattering structure participates in the oscillatory motion, this direction is realized doubly for a period of attached internal waves. By virtue of this fact, immediately after the passage of the vortex, the acoustical pulses arrive at the antenna's input. Their repetition frequency is close to the doubled frequency ω of internal waves on the scattering horizon. In Fig. 4, we demonstrate a record of echo signals from a wake, which are normalized to their own maximum W_m. The scattering maxima grow during the first two oscillations and rapidly decay during the subsequent three. The value of the initial maximum is determined by the phase of wave oscillations.

In order to identify the character of the motion in the scattering domain, the energetically significant segment of the echo signal ($t < 3T_b \approx 25$ s) is approximated by a finite series containing m Gaussian-shaped pulses. Their amplitudes a_t and arrival times t_i are taken from the experimental curve $\frac{W}{W_m}$. At the same time, the durations τ_i are given as equal and are selected from the condition of the best coincidence with experimental data:

$$A(t) = \sum_{1}^{m} a_i \exp\left[-2\left(\frac{t-t_i}{\tau}\right)^2\right]. \qquad (2)$$

For the first five pulses (m = 5), the parameters of the model signal are a_m = 0.63, 1.00, 0.91, 0.39, and 0.22; t_m = 5.7, 10.2, 14.4, 18.0, and 21.6 s. The best approximation corresponds to $\tau_m = \tau_0 = 2$ s.

The frequency spectra $\frac{F}{F_m}$ of the original signal and sequences (2) normalized to their own maxima (curves *1* and *2* in Fig. 4) are consistent with each other. The isolated secondary spectral peaks are positioned at the same frequency f_m = 0.25 Hz. The process with the indicated parameters corresponds to scattering from a single inhomogeneity that performs damping oscillations within the zone of the sonic beam under the action of internal waves with a circular frequency $\omega = \pi f_m$ =

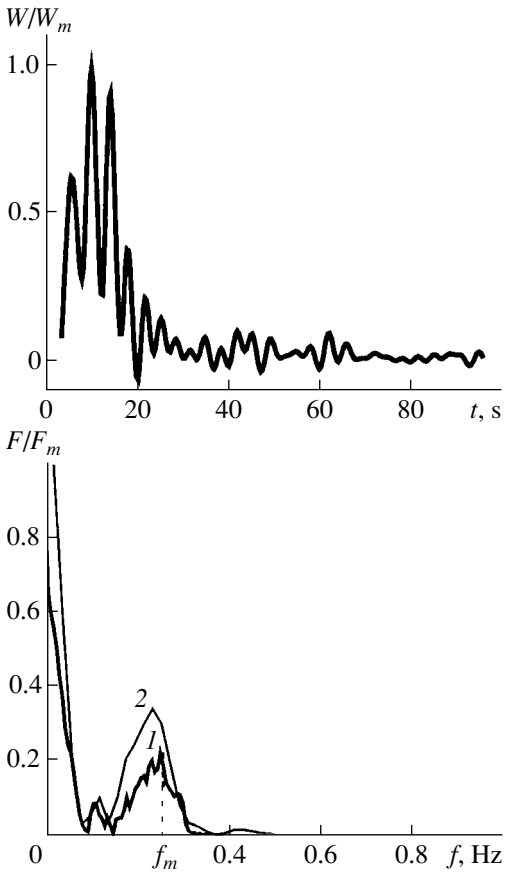

Fig. 4. Normalized characteristics of the echo signal from the wake. The echo-signal level $\frac{W}{W_m}$ and frequency spectra $\frac{F}{F_m}$ for echo signal (*1*) and approximating function (*2*) are shown.

0.8 s^{-1}. The given value is used in the calculation of the characteristic thickness of the scattering inhomogeneity.

High-resolution optical methods show that, in addition to internal waves, thin high-gradient interlayers exist in the wake beyond a solid body. These interlayers are formed due to the separation of boundary layers or, directly, in the bulk of the continuously stratified fluid [8]. The scales of the interlayer thicknesses, i.e., of internal boundary flows, are determined by both the kinematic viscosity and wave frequency in the velocity field $\left(\delta_\nu = \sqrt{\frac{2\nu}{\omega}}\right)$, as well as by the diffusivity in the salinity field $\left(\delta_s = \sqrt{\frac{2\kappa_s}{\omega}}\right)$ [9]. For an aqueous solution of common salt, the ratio of the thicknesses of dynamic and concentration layers is $\frac{\delta_u}{\delta_s} = \sqrt{\frac{\nu}{\kappa_s}} = 27$. In the conditions of the given experiments, the value of the oscillation frequency $\omega = 0.8$ s^{-1} corresponds to the scales $\delta_\nu = 0.16$ cm and $\delta_s = 0.005$ cm. The former value is close to the $\delta = 0.15$ cm found experimentally in accordance with the vertical spectra (Fig. 3). This consistency indicates the noticeable role of internal dynamic boundary layers in the formation of acoustically contrasting structures in laboratory and full-sized conditions. For detection of these structures against the background of a totality of bulk undirected scatterers, algorithms of coherent processing with the phase correction of the scattered sound-pulse front are efficient.

ACKNOWLEDGMENTS

The work was supported by the Ministry of Industry, Science, and Technology of the Russian Federation (Program for the Support of Unique Experimental Facilities, project no. 02-01) and by the Russian Foundation for Basic Research (project nos. 02-05-06367 and 09-01-00434).

REFERENCES

1. M. H. Orr, L. R. Haury, P. P. Wiebe, and M. G. Briscoe, J. Acoust. Soc. Am. **108**, 1595 (2000).
2. V. E. Ostashev, T. M. Georges, and G. H. Goedecke, J. Acoust. Soc. Am. **109** (4), 2682 (2001).
3. *Physics of the Ocean*, Vol. 2: *Hydrodynamics of the Ocean*, Ed. by V. M. Kamenkovich and A. S. Monin (Nauka, Moscow, 1978).
4. T. Colonius, S. A. Lele, and P. Moin, J. Fluid Mech. **260**, 271 (1994).
5. V. V. Mitkin, V. E. Prokhorov, and Yu. D. Chashechkin, Izv. Akad. Nauk, Mekh. Zhidk. Gaza, No. 6, 92 (2001).
6. V. V. Mitkin, V. E. Prokhorov, and Yu. D. Chashechkin, Dokl. Akad. Nauk **377** (2), 201 (2001) [Dokl. Phys. **46**, 202 (2001)].
7. E. Ya. Sysoeva and Yu. D. Chashechkin, Izv. Akad. Nauk SSSR, Mekh. Zhidk. Gaza, No. 4, 82 (1991).
8. Yu. D. Chashechkin and V. V. Mitkin, Dokl. Akad. Nauk **362**, 625 (1998) [Dokl. Phys. **43**, 636 (1998)].
9. Yu. V. Kistovich and Yu. D. Chashechkin, Prikl. Mekh. Tekh. Fiz. **39** (5), 88 (1998).

Translated by G. Merzon

Doklady Physics, Vol. 48, No. 1, 2003, pp. 9–12. Translated from Doklady Akademii Nauk, Vol. 388, No. 2, 2003, pp. 177–180.

PHYSICS

Novel Designs of Semiconductor Lasers

Academician V. A. Gelovani and V. I. Shveĭkin

Received May 17, 2002

Semiconductor, or diode, lasers are the key and indispensable elements in informatics and telecommunication facilities, in devices for optical memory, printing, material processing, and pumping of optical-fiber and solid-state lasers, etc.

The fundamental disadvantage of modern facet diode lasers is the small emission area on the output facet in the vertical plane. This circumstance is responsible for the high density of laser radiation from the output facet and for the large divergence of laser radiation in the vertical plane. The high radiation density limits output power because of catastrophic damage to the facet and significantly decreases the reliability and service life of diode lasers.

Much effort is directed to overcoming this critical disadvantage and in particular to hardening the output facet surface.

There were also attempts to extract radiation from the active layer into a substrate by means of leaking radiation. For example, such diode lasers were proposed and implemented in [1–5]. However, lasing in them is similar to that in conventional facet diode lasers (it occurs in a thin active wave-guide region), and radiation flowing into a semiconductor substrate is directly extracted. In spite of the high output-radiation directivity achieved in this case, these diode lasers have the following disadvantages:

(i) the use of a substrate as an inflow region limits both laser wavelengths and necessary outflow angles;

(ii) since two kinds of radiation—inclined leaking and divergent facet—are simultaneously present on the same facet, the efficiency of diode lasers decreases because of technological difficulty in separating these radiations.

In this study, we propose novel designs of diode lasers based on [6, 7] and on new principles of using leaking radiation, i.e., radiation flowing from the active region (optical wave guide) under certain conditions, in lasing. These designs of diode lasers with leaking radiation in the optical resonator, along with their other advantages, provide a multiple increase in the size of the emission area on the output surface of diode lasers.

Figure 1 shows one of the possible simple designs of a heterostructure for the proposed leaking-mode diode lasers. The active region of this heterostructure consists of two quantum-well InGaAs layers *1* and *2* and three barrier GaAs layers *3*, *4*, and *5*. On the side of the *p*-type layer (on the barrier layer *4*), there is cladding $Al_xGa_{1-x}As$ layer *6*, which is adjacent to highly doped *p*-type contact GaAs layer *9*. On the side of the *n*-type layer, barrier layer *5* borders on inflow $Al_yGa_{1-y}As$ layer *7*, whose thickness is as a rule largest. Next, reflective (for leaking radiation) $Al_xGa_{1-x}As$ layer *8* is located on *n*-type GaAs substrate *10*. The inflow-layer composition satisfies the condition $y < x$.

Despite a certain resemblance between conventional modern diode lasers and leaking-mode diode lasers, there is a radical difference between them. In the former case, leaking radiation is reduced to virtually negligible values, because it represents the loss of laser radiation. In contrast, quite intense leaking radiation from the active layer into the inflow layer is formed in the range of operating currents in the latter case. This is achieved by choosing the composition and thicknesses of the layers of the laser heterostructure so that the refractive index n_{in} of the inflow layer exceeds the effective refractive index n_{eff} for the entire heterostructure, at least in a given range of currents [6, 7]. In this case, leaking radiation distributed over the entire surface of

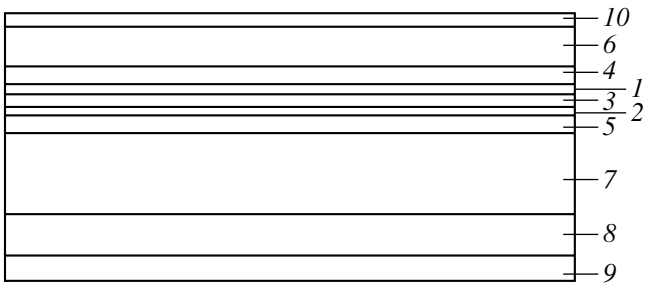

Fig. 1. Scheme of the simplest construction of a heterostructure for a leaking-mode diode laser: (*1* and *2*) active InGaAs layers; (*3*–*5*) barrier layers; (*6*) cladding *p*-type layer; (*7*) outflow layer; (*8*) reflective *n*-type layer for leaky radiation; (*9*) contact p^+-type layer; and (*10*) *n*-type GaAs substrate.

Institute of System Analysis, Russian Academy of Sciences, pr. 60-letiya Oktyabrya 9, Moscow, 117312 Russia
e-mail: aswl@isa.ru

1028-3358/03/4801-0009$24.00

the active layer (which consequently has a small divergence angle) will penetrate into the inflow layer along the longitudinal axis of the optical resonator at certain divergence angles $\varphi = \pm\cos\frac{n_{\text{eff}}}{n_{\text{in}}}$ in two opposite directions. Since $\tan\varphi \gg \frac{d_{\text{in}}}{L_{\text{res}}}$ in the case under consideration (where d_{in} is the thickness of the inflow layer and L_{res} is the length of the optical resonator), leaking radiation is multiply reflected in the vertical plane from the cladding and reflective layers, as well as from the mirrors of the optical resonator (with reflectivities R_1 and R_2). As a result, wave-guide-mode radiation is formed in leaking-mode diode lasers. Therefore, output radiation will be directed approximately at a right angle to the plane of the optical output facet, and its directivity pattern will depend mainly on the number of the excited mode and the thickness of the inflow layer.

In applications, it is often required to obtain the zeroth (fundamental) mode. The main feature of the diode lasers under consideration is that the stable control of the fundamental mode in them is possible at large values of inflow-layer thickness (at least up to 10 μm, as we verified experimentally). Therefore, small divergence angles of radiation $\theta_\perp$ in the vertical plane can be obtained (in our experiments, we obtain $\theta_\perp = 6.9°$). In the available diode lasers with a broadened wave-guide [8], higher order modes appear even at wave-guide-layer widths exceeding 1 μm. Such a significant difference is attributed to the fundamentally different mechanism of the mode formation in leaking-mode diode lasers, where the index (number) of the excited mode is strictly determined by the outflow angle φ, which depends in turn on the thickness of the inflow layer.

In order to create efficient leaking-mode diode lasers with high-quality radiation, it is necessary to control the current-density dependence of the localization factor Γ of optical radiation in the active layer. For lasing thresholds to be low for low current densities, it is desirable that the fraction of this radiation that is determined by Γ is comparatively large, i.e., comparable with Γ for conventional diode lasers. In this case, leaking radiation may be insignificant or even virtually absent. After the threshold current of emission is achieved in the remaining range of operating currents, it is sufficient only to maintain the reached threshold level of emission in the active layer. Here, leaking radiation will increase with increasing current above the threshold, and, for a sufficient excess of emission threshold, radiation leaving the inflow layer will prevail in total output radiation.

When experimentally realizing novel diode lasers, we focused on the production of laser radiation whose wavelength is near 980 nm. This range of wavelengths is successfully used to create diode pumping modules of optical-fiber amplifiers and lasers. The basic parameters of the structure were calculated by mathematical simulation based on the above conditions of the balance of leaking radiation before and after achieving the emission threshold.

In accordance with the calculation results, heterostructures for leaking-mode diode lasers were made on *n*-GaAs substrates by the MOCVD method with lower pressure. Both $In_{0.20}Ga_{0.80}As$ stressed quantum-well active layers were grown 8 nm in thickness. The thickness of the barrier layer between them was 12 nm. The *p*-type cladding and *n*-type reflective layers of the identical $Al_{0.3}Ga_{0.7}As$ composition had the same thickness of 1 μm. The 5-μm-thick inflow *n*-type layer was grown from the undoped *n*-type $Al_{0.21}Ga_{0.79}As$. The thickness of the highly doped contact layer (made of p^+-type GaAs) was equal to 0.1 μm.

The ridge-type active element (chip) of a leaking-mode diode laser was prepared by ion etching followed by obliteration of the etched side regions with semi-insulating zinc selenide [9]. The widths of current-pumped strips were 6, 10, 15, 20, and 50 μm. The ohmic contacts to the *p*-type layer were obtained by the laser evaporation of thin layers of Zn-doped nickel and further of the barrier Mo–Ti–Ni layers, followed by thermal evaporation of Au. Ohmic contacts to the *n*-GaAs substrate were produced by the usual method of thermal evaporation of Ge–Au.

We prepared a number of novel wide-aperture high-efficiency high-power semiconductor lasers, where leaking radiation from the active region was involved in lasing. The test of the prepared samples provided the following results:

(i) single-mode (in the transverse index) semiconductor lasers, where the near-field zone had sizes from 5 to 10 μm and corresponding angle $\theta_\perp$ of mode divergence in the vertical plane was 11.1° to 6.9°, were realized;

(ii) semiconductor lasers with the output aperture with the dimensions 5×6, 7×7.5, and 10×10 μm on the optical facet, were produced;

(iii) at a wavelength of 980 nm for the strip width $w = 5$ μm with the divergence angles $\theta_\perp \times \theta_= = 12.3° \times 5.7°$ and low threshold current densities, a single-mode semiconductor laser with a radiation power of 0.5 W and a high-brightness semiconductor laser with a radiation power of 1.3 W were implemented;

(iv) in the continuous mode, a radiation power of 3.0 W was obtained from a wide-aperture laser diode with the strip width $w = 50$ μm at small divergence angles $\theta_\perp \times \theta_= = 11.5° \times 7.2°$;

(v) single-frequency 925-nm laser radiation with a power of 500 mW and divergence angles $\theta_\perp \times \theta_= = 12° \times 5.7°$ was generated.

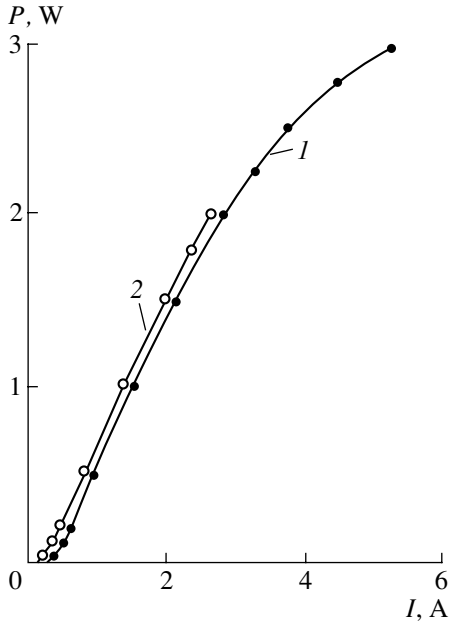

Fig. 2. Power–current characteristics of a leaking-mode diode laser with strip width w = 50 μm. A chip is soldered on a Cu plate so that its heterostructure is at the (*1*) bottom and (*2*) top.

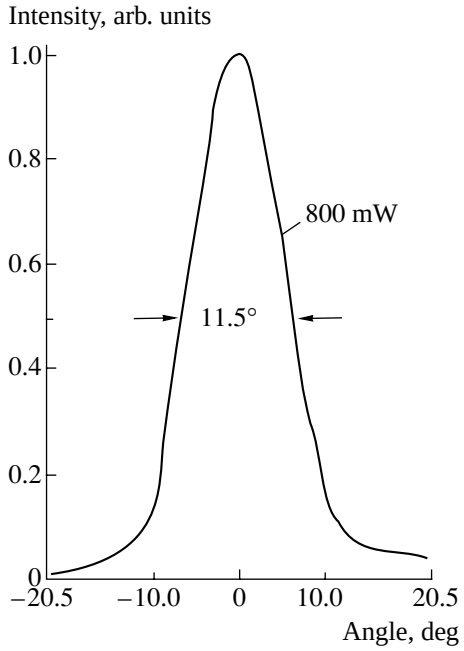

Fig. 3. Distribution of 0.8-W radiation in the far-field zone in the vertical plane for a leaking-mode diode laser with w = 50 μm, L = 1600 μm, R_1 = 95%, and R_2 = 10%.

Figure 2 shows the power–current characteristics for two samples of leaky-mode diode lasers (strip width w = 50 μm, length L_{res} = 1600 μm, R_1 = 95%, and R_2 = 10%). All the measurements were carried out in the continuous mode. The maximum radiation power obtained for a current of 3.0 A was 3.0 W (22 W in the pulsed mode). The decrease in power for currents exceeding 3.0 A is reversible and caused by overheating.

The far-zone field of radiation in the vertical plane for these samples is presented in Fig. 3. The divergence angle $\theta_\perp$ in the vertical plane is equal to 11.5° and depends slightly on the radiation power. In contrast, the divergence angle $\theta_=$ in the horizontal plane increases from 3.28° to 7.8° with increasing radiation power from 100 to 800 mW, respectively.

Figure 4 shows the power–current characteristics for two leaking-mode diode lasers with strip-region width w = 10 μm. Reflectivities R_1 and R_2 were equal to 95 and 7%, respectively, and L_{res} = 1600 μm. The output powers were measured up to P = 1.0 and 1.3 W. For the sample with P = 1.0 W, the threshold current is $j_{thre} \approx$ 70 mA and the maximum differential efficiency is η_d = 58%. With increasing radiation power from 100 to 1000 mW, the divergence angle $\theta_\perp$ increases from 11.5° to 12.3°. The lasers under consideration stably generate a single spatial mode up to a power of 0.5 W. With a further increase in power up to 1 W, the single mode in the transverse index in the vertical plane was retained when $\theta_\perp$ increased up to 12.3°. Weak mode interference arose in the horizontal plane, and the angle $\theta_=$ increased up to 7.0° (i.e., by ~13%).

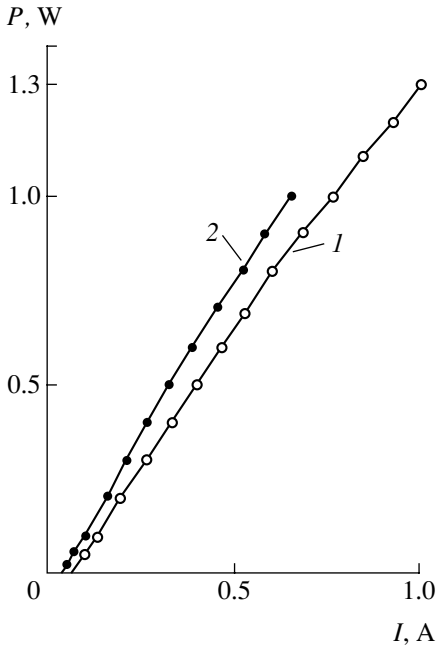

Fig. 4. Power–current characteristics for a leaking-mode diode laser with w = 10 μm, L = 1600 μm, R_1 = 95%, and R_2 = 7%.

ACKNOWLEDGMENTS

This study was supported by the D-LED corporation (2000–2001 research program).

REFERENCES

1. D. R. Scrifers, W. Streifer, and R. D. Burnham, Appl. Phys. Lett. **29** (1), 23 (1976).
2. V. I. Shveĭkin, A. P. Bogatov, A. E. Drakin, and Yu. V. Kurnyavko, RF Patent No. 2133534, Izobreteniya, No. 20 (1999).
3. N. B. Zvonkov, B. N. Zvonkov, and A. V. Ershov, Kvant. Élektron. (Moscow) **25** (7), 622 (1998).
4. V. I. Shveĭkin, A. P. Bogatov, A. E. Drakin, and Yu. V. Kurnyavko, Kvant. Élektron. (Moscow) **26** (1), 33 (1999).
5. A. P. Bogatov, A. E. Drakin, and V. I. Shveĭkin, Kvant. Élektron. (Moscow) **26** (1), 28 (1999).
6. V. I. Shveĭkin, RF Patent No. 2142665, Izobreteniya, No. 34 (1999).
7. V. I. Shveĭkin, *Injection Laser*, International Application RST/RU99/00275, Supplement, June 5, 2000, Publ. No. WO00/10235 (Feb. 24, 2000).
8. M. Gokhale, J. C. Dries, P. V. Studenkov, *et al.*, Quantum Electron. **33** (12), 2266 (1997).
9. E. I. Davydova, V. V. Popovichev, M. B. Uspenskiĭ, *et al.*, RF Patent No. 2035103, Izobreteniya, No. 13 (1995).

Translated by Yu. Vishnyakov